7-17-2023

Large Dry Metal Electrodes for Physiological Monitoring

Krittika Goyal
krgmet@rit.edu

Recommended Citation

Goyal, Krittika, "Large Dry Metal Electrodes for Physiological Monitoring" (2023). Thesis. Rochester Institute of Technology. Accessed from

RIT

Large Dry Metal Electrodes for Physiological Monitoring

by

Krittika Goyal

A dissertation submitted in partial fulfillment of the requirements
for the degree of Doctorate of Philosophy in Microsystems Engineering

Microsystems Engineering Program
Kate Gleason College of Engineering

Rochester Institute of Technology

Rochester, New York

July 17th, 2023

Large Dry Metal Electrodes for Physiological Monitoring

by

Krittika Goyal

Committee Approval:

We, the undersigned committee members, certify that we have advised and/or supervised the candidate on the work described in this dissertation. We further certify that we have reviewed the dissertation manuscript and approve it in partial fulfillment of the requirements of the degree of Doctor of Philosophy in Microsystems Engineering.

Steven W. Day, Ph.D. Professor and Department Head, Biomedical Engineering	Date
David A. Borkholder, Ph.D. Professor, Microsystems Engineering	Date
Dan Phillips, Ph.D. Associate Professor, Electrical and Microelectronic Engineering	Date
Michael Richards, Ph.D. Assistant Professor, Biomedical Engineering	Date
Jayanti Venkataraman, Ph.D. Professor, Electrical and Microelectronic Engineering	Date

Certified by:

Stefan F. Preble, Ph.D. Director, Microsystems Engineering Program	Date

ABSTRACT

Kate Gleason College of Engineering

Rochester Institute of Technology

Degree: Doctor of Philosophy **Program**: Microsystems Engineering

Authors Name: Krittika Goyal

Advisors Name: Steven W. Day

Dissertation Title: Large Dry Metal Electrodes for Physiological Monitoring

Cardiovascular disease is the leading cause of death in the United States. In-home physiological monitoring systems have a potential to track daily changes in cardiovascular health and to provide health care professionals data about the recovery or deterioration of their patient's cardiac health. Various in-home monitoring systems have been designed to capture physiological signals from both standard (chest, wrist) and non-standard (palms, buttocks) locations. Unfortunately, most in-home monitoring systems provide poor signal quality due to the use of dry electrodes. Dry electrodes have an unstable electrochemical interface that results in high and variable contact impedance and poor signal quality.

The present work focuses on investigating the dependence of the electrode-skin impedance, and resulting signal quality, on the electrode material, electrode area, and skin hydration. This overall goal is accomplished by three separate studies. First, a novel equivalent circuit model for the skin-electrode interface impedance model was developed, which was validated on human skin and with a first of its kind skin phantom. The results of the model suggest the relative permittivity of the native oxide for the electrode material can provide insight into the electrode performance for biopotential measurements.

Second, this work demonstrates an application of previous model to evaluate the feasibility of using the dry electrodes to capture clinically relevant Electrocardiogram (ECG) signals by using large dry titanium electrodes integrated into a toilet seat cardiovascular monitoring system. *In vivo* skin-electrode contact impedance and ECG measurements were conducted across ten healthy human subjects, and quantitative comparisons were performed to compare the ECG signal quality between different electrode configurations. It was found that large titanium electrodes resulted in better signal quality than large stainless steel electrodes.

Third, this work demonstrates the use of large dry titanium electrodes to monitor respiration by measuring changes in impedance from the back of the thigh, which may be useful for several conditions including COVID-19 recovery, and progression of edema during heart failure management. The feasibility of the thigh and the sensitivity of impedance to respiration were investigated empirically, by comparing thorax and thigh-thigh bioimpedance measurements to spirometer measurements, and computationally, using finite element modeling (FEM). Empirical thigh-thigh bioimpedance resulted in a high correlation (0.87) to the respiration rate and tidal volume. The FEM model predicts that thigh-thigh bioimpedance measurements might not be sensitive to pulmonary edema detection, however, the ability to effectively measure respiratory rate and tidal volume from the back of the thigh can be used for tracking COVID-19 recovery.

ACKNOWLEDGMENTS

To my dear husband Sarthak, thank you for always believing in me. This would not have been possible without your unconditional love and support. Thank you for pushing me to pursue doctoral studies, this is just as much your Ph.D., as it is mine. Thank you for always being there by my side, in all the ups and downs of my life. Thank you for staying up late at night so that I could meet deadlines. Thank you for motivating me and keeping me calm through this journey. You made sure, that I stay focused, took care of all the household chores, and also made scrumptious food for me. Words cannot express how grateful I am for your unconditional love, you are my biggest strength!

To my parents, thank you for having confidence in me and supporting me to break the social barriers. You taught me to be organized, respect everyone, and stay humble and grounded. Thank you for instilling in me these values. To my in-laws, thank you for loving me and always supporting me. Your encouragement enabled me to stay motivated, throughout the course of my Ph.D.

To Dr. Day, thank you for your guidance and support, and for trusting me. The experiences and insights you shared with me, especially in our 1-1 meetings, shaped my career and I will carry them with me throughout my life. Thank you for having my back, and supporting me in all of my decisions. Your words “go for it” boosted my confidence. I want to thank you for providing me the exposure to conferences, allowing me to work at MCC, and teaching me different aspects of journal, conference, and book writing. Thank you for traveling on my behalf to the Greece conference and for speaking highly of me. I would not be finishing this doctorate today without your support. I look forward to sharing my professional career and continued interactions with you.

To Dr. Borkholder, thank you for providing me with a strong foundation to build upon and ample resources. Thank you for developing in me the ability to think critically, working with collaborators, and teaching me how to run and write human subject studies. I am grateful to you, for understanding my strengths and weaknesses and guiding me in the right direction. Thank you for always getting back to me at short notice and providing constructive feedback. I look forward to future collaborations with you.

I would like to thank Dr. Phillips, for always encouraging me and appreciating my research. I have always looked up to you as a role model, especially as a teacher in the field of bioinstrumentation. I would like to thank Dr. Richards, for introducing me to the polyvinyl alcohol material and the cryogel phantoms. Your inputs during the milestone meetings have been really fruitful.

I had the privilege to work with Dr. Nicholas Conn during the initial years of my Ph.D and would like to thank him for his mentorship. I would like to also thank Dr. Linwie Wang for providing me with the NIH R01 grant funding which enabled me to present my work at the conferences. Additionally, I would to thank Lisa Zimmerman, James Stefano, and Renee Milliken, for always being there for me.

Finally, I would like to thank my entire committee and my department. It has been a pleasure to be a part of the Microsystems department. I could not be more grateful for all that I have experienced and learned.

Contents

List of Figures

List of Tables

Chapter 1: Introduction

1.1 Cardiovascular Disease: Heart Failure

Cardiovascular disease (CVD) is the leading cause of death globally. In the US alone, cardiovascular disease accounted for 695,000 deaths in 2021, approximately 1 of every 5 deaths [1], [2]. As per the American Heart Association (AHA) reports, there is a high prevalence of CVD in older adults; ~75% of individuals from 65–79 years are impacted by CVD [3]. Cardiovascular disease includes several heart and blood vessel diseases such as heart failure, stroke, atrial fibrillation, etc.

Heart failure is a condition when the heart is not able to pump enough blood to meet the body's needs. Heart failure is mostly a chronic condition. About 6.2 million Americans have heart failure as of 2016, and the numbers are expected to rise by 2030, resulting in more than 8 million people with heart failure [4]. Half of those diagnosed with heart failure will die within 5 years [4]. When the heart is not pumping sufficiently, fluid accumulates in the body and causes swelling, which is also known as edema. Fluid usually accumulates in the lower legs, ankles, and lungs. Accumulation of fluid in the lungs is known as pulmonary edema, which leads to shortness of breath. Approximately 1 in 9 deaths includes heart failure as the contributing cause [4].

1.1.1 Projected Costs and Hospital Readmissions

CVD is the most costly chronic disease. CVD total costs consist of direct medical and indirect costs including lost productivity at the workplace and home. As per the recent analysis by the AHA, the total direct and indirect costs of CVD are expected to grow from $555 billion in 2015 to $1.1 trillion in 2035, as detailed in Figure 1.1 [5]. Medical and indirect costs are expected to increase by 135% and 55% respectively. As of 2015, heart failure alone contributes to 18 billion dollars direct medical and 11 billion dollars indirect costs [5].

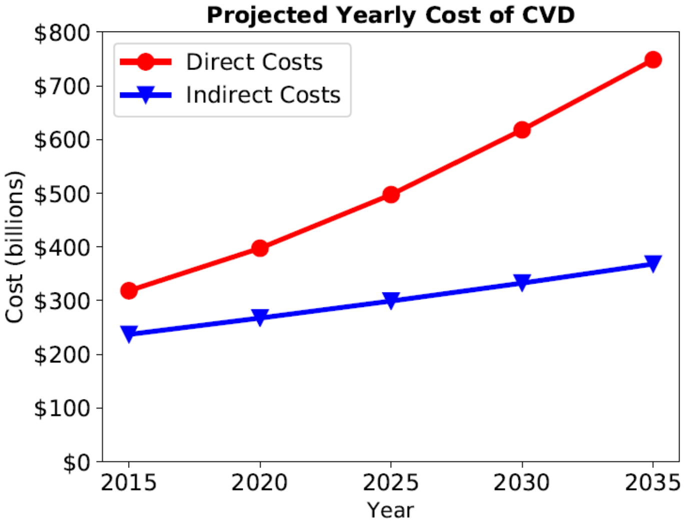

Figure 1.1. Projected yearly direct and indirect costs of cardiovascular disease (CVD). Data plotted using [5].

Further, the medical costs comprise all the charges related to medical services such as hospital, physician, prescription, home health, and nursing home as detailed in Figure 1.2. for the case of heart failure. It can be seen that hospitalization is a significant cost. One reason for the high cost of hospitalization is readmissions; approximately 25 percent of HF patients are readmitted within 30 days of discharge [6].

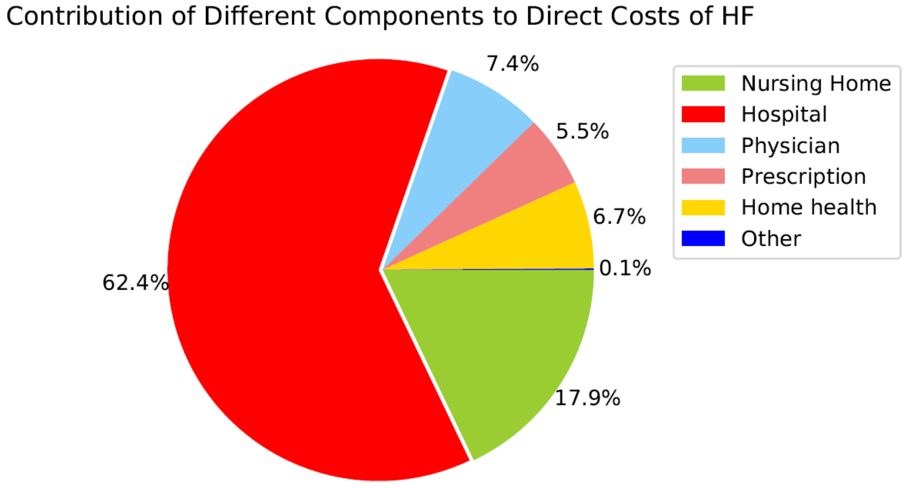

Figure 1.2. Percentage contribution of different components (by point of service) to direct cost of heart failure (HF). Data plotted using [5].

To reduce the readmission rates, follow-up appointments are scheduled within two weeks of patient discharge [7]. Hospital readmissions may also reduced using in-home physiological monitoring systems. In-home physiological monitoring systems have a potential to track the daily changes in one's cardiovascular health and give care providers advanced notice of the deterioration of their patient's cardiac health. As an example, daily tracking of weight can provide insight into the cardiac condition of the HF patient, as an increase in weight could be an indicator of water retention and deteriorating condition [18].

1.2 In-Home Physiological Monitoring: Benefits and Challenges

In-home physiological monitoring, also known as remote patient monitoring, enables monitoring patients from the comfort of their homes or remotely without the need to visit the clinical settings [8]. It has a potential to make a healthcare transformation from reactive to proactive and preventive care. It helps in improving health care and reducing healthcare costs. However, there are some challenges with remote patient monitoring. fFirst, physician may not trust the efficacy and accuracy of the remote monitoring device. Second, the devices should be easy to use and should not require a trained person. For example, a Holter monitor is a device that captures ECG using wet electrodes; the positioning of the electrodes should be consistent to accurately capture the physiological changes in one's cardiac condition [9]. The benefits and challenges of in-home physiological monitoring will be discussed in more detail in the subsequent sections.

1.2.1 Significance of In-Home Physiological Monitoring

In-home physiological monitoring has the potential to reduce hospitalization rates by tracking the daily changes in one's health and by enabling early detection of deterioration before the situation worsens. Remote patient monitoring has shown success in lowering hospitalization rate. As an example, a study was carried out by the University of Pennsylvania Health Care, and the effectiveness of a transitional care model (skilled home health) was evaluated among HF patients in reducing 30-day readmissions among HF patients [10]. The study was conducted on 818 HF patients, and the information about various health parameters such as blood pressure, weight, heart rate, and blood oxygenation was collected. There was a 73% relative reduction in the All-cause 30-day readmission rate in three years. Another study, named Heart Health Program, was conducted at Mount Sinai Health System, and the feasibility of digital health monitoring was examined on the 30-day readmission rate. A blood pressure cuff and a digital scale were connected through Bluetooth with an iHealth mobile app on the patient's smartphone, and the data was sent to provider care teams. In this study, 58 patients were recruited, and the 30-day hospital readmission rate dropped to 10% compared to the earlier rate of 23% [11]. Hence, remote monitoring can be critical in diagnosing and managing cardiovascular diseases such as heart failure [13] .

1.2.2 Current Remote Monitoring Technologies

The current state of the art is inclined towards non-invasive technologies using wearable mobile devices and patch-based sensors. Various devices starting from as simple as a bathroom scale to wearable devices can be used for in-home cardiac health monitoring. Current remote monitoring devices include devices such as watches and wearable vests. A few have been listed below to demonstrate the current state of the art, as shown in Figure 1.3. One such device is a Holter monitor that measures the heart's activity and provides an ambulatory electrocardiogram [9]. It is portable and worn for a short period (24-72 hours) to determine if the subject has any occasional cardiac arrhythmias. The ECG is captured using the wet electrode patches on the skin, which results in clinically relevant ECG signal quality. However, there are certain drawbacks of using the wet electrodes: the skin needs to be prepared by a skilled person; the gel dries over time, leading to signal degradation; and the removal of the gel electrodes is often painful or leads to skin irritation. To overcome challenges of wet electrodes , devices utilize dry electrode technology to measure ECG. One such device is KardiaMobile by AliveCor, a US-based company [14]. It is a hand-held device and can detect atrial fibrillation (an irregular and rapid heart rate). It uses two 3cm x 3cm stainless steel electrodes and provides single-lead ECG. To make the devices more user-friendly, dry electrodes are being integrated into wearable devices such as watches. One such device is an Apple watch series 4 [15]. It measures a single-lead ECG and consists of two electrodes, where the digital crown made up of titanium serves as one of the electrodes, and the sapphire crystal electrode on the back of the Apple watch serves as another electrode. For accurate measuring of ECG, the watch should neither be too tight nor too loose, as it can affect the ECG recording.

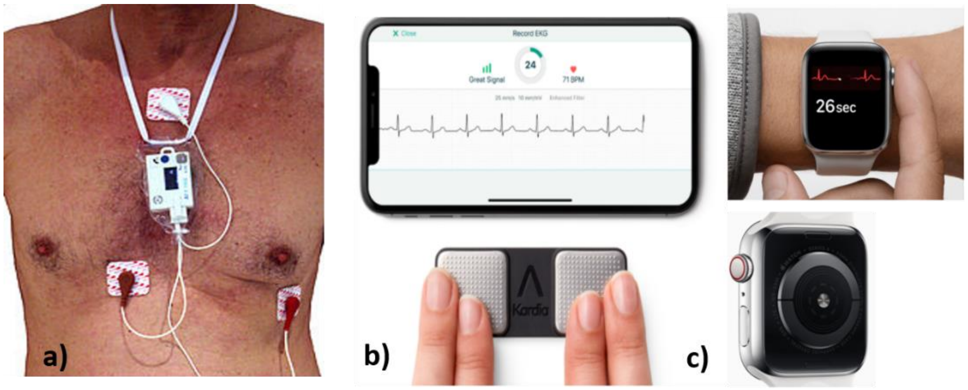

Figure 1.3. Examples of current in-home physiological monitoring devices for measuring single-lead ECG. a) Holter monitor using three wet electrodes [9]. b) KardiaMobile by Alivecor using dry stainless steel electrodes [14] c) Apple watch series 4 using crown (titanium) and backside (chromium silicon carbide nitride) as dry electrodes [15].

Apart from measuring heart activity, other devices are used to measure bioimpedance across the thorax, focusing on tracking the health condition of HF patients. One such device has been designed by Philips Technologies Gmbh, Aachen, Germany, which measures transthoracic impedance to monitor the fluid levels in the lungs (pulmonary edema) for HF patients [16]. It is a wearable device that consists of an adjustable vest, four electrodes, and a measurement device, as shown in Figure 1.4. The four electrodes are textile-based dry electrodes made from silver-coated polyurethane yarn. The measurement device injects current through two electrodes, and a corresponding voltage is measured through the other two electrodes. During a single acquisition, sixteen frequencies ranging from 10 kHz – 1 MHz are measured. Since this device is also based on dry electrodes, it also suffers from signal quality issues. Dovancescu et al. reported that electrodes had to be wetted to lower skin interface impedance to achieve good signal quality, which complicates the use of the device [17]. Another such device by an Israel-based company Cardioset uses stainless steel-based dry electrodes to detect fluid accumulation in the lungs [19].

Figure 1.4: Wearable vest for measuring transthoracic impedance with four embedded textile-based electrodes [16], [17].

1.2.3 Challenges of Dry Electrode Based Monitoring Technologies

The devices mentioned above are based on dry electrodes. Although dry electrodes are more user friendly and can overcome the challenges of wet electrodes, they generally lead to poorer quality signals. Dry electrodes have a poor electrochemical interface due to the absence of the gel, and thus high skin-electrode contact impedance, leading to poor signal quality. This high impedance is also variable, depending on location and pressure, which can cause drift and motion artifacts in the signal. In addition to the challenges of dry electrodes, measurements at a consistent physiological state are important for accurate trend analysis. Each of the devices, as mentioned earlier, has one thing in common, they require the subject to change their daily habits and perform the measurement at the correct time of day. Hence, patient compliance is often very low, and there is a need for a novel method that ensures patient compliance.

1.2.4 Toilet Seat Cardiovascular Monitoring System

There is an opportunity for daily in-home physiological monitoring from a non-standard location by integrating sensors into a toilet seat. The fully integrated toilet seat (FIT) contains multiple sensors and can capture single-lead electrocardiogram (ECG), photoplethysmogram, ballistocardiogram, and body weight [18]. All the sensors are self-contained, the whole device is battery-powered, wireless, and can be easily mounted on a standard toilet (Figure 1.5). The data gets captured when the user sits on the seat and is wirelessly transmitted to a base station and uploaded to the cloud. This novel bioinstrumentation system has a potential to resolve many challenges of the aforementioned devices. The novel method's major advantages include automatic skin contact and repeatable electrode placement. Additionally, sitting leads to consistent pressure and less electrode slippage on the skin. It further addresses the major challenge of patient compliance, as the system will enable us to make inconspicuous measurements without forcing the subject to have a significant change of habit. Lastly, the measurements may be captured at the same time every day which is helpful when looking for day-to-day trends. The physician can use the resulting data to track their patient's daily health condition and intervene as required.

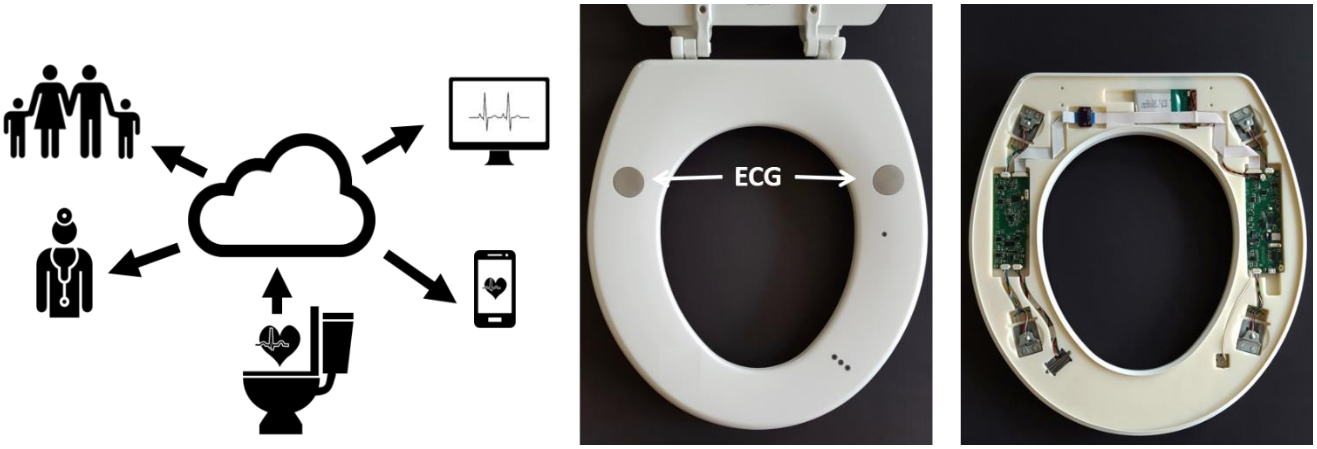

Figure 1.5. Fully integrated toilet seat with self-contained sensors and electronics inside the seat (Image modified from reference [18]).

1.2.5 ECG instrumentation in the FIT seat

Out of the FIT seat's multiple functionalities, of particular interest is the acquisition of ECG for this research work. The ECG signal's amplitude is <2 mV for conventional limb leads and <0.1 mV for buttocks ECG. The magnitude of electromagnetic noise present in the surroundings is significantly large compared to the ECG signal. The ECG signal is differentially measured with instrumentation amplifiers with a high common mode rejection ratio to reject the common noise across the body. Hence, ECG is measured as the difference between two electrodes. FIT measures a single-channel ECG with dry stainless steel (SS) electrodes (diameter = 28mm). Figure 1.6 shows that the signal is amplified by a differential amplifier (instrumentation amplifier) before further amplification and filtering.

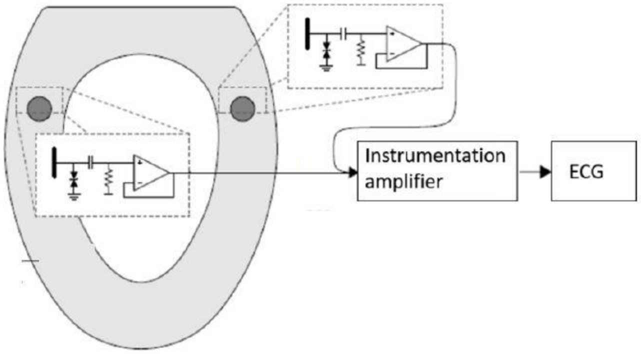

Figure 1.6: The differential pair of electrodes (SS) are connected to the two active electrode analog front-end (AFE) circuits. The right leg reference electrode is grounded. The output of each AFE is connected to an instrumentation amplifier, and the resulting ECG is captured (Image modified from reference [18]).

One of the large factors that impact ECG signal acquisition is the electrode interface and skin impedance. The combination of dry electrodes and fairly weak ECG signal in the buttocks make obtaining a significantly high quality ECG a challenge.

1.3 Aims

This research aims to improve the signal quality from dry electrodes to overcome the challenges of in-home physiological monitoring devices. The research work carried out here has been broadly divided into three aims.

1.3.1 Aim 1

a) To investigate the electrode-skin impedance dependence on the electrode material, the electrode area, and the skin hydration by developing an equivalent skin-electrode interface impedance model for dry electrodes.

b) To fabricate a 2-layered skin phantom to mimic skin's electrical properties in the low-frequency range (1 Hz-1000 Hz) along with controlled hydration status.

The first aim of this work is to investigate the dependence of the electrode-skin impedance, and resulting signal quality, on the electrode material, the electrode area, and the skin hydration. This overall goal is accomplished by three separate studies. First, a novel equivalent circuit model of the skin-electrode interface impedance, validated on human skin and with a first of its kind skin phantom. The properties of the human skin may change over time. Hence, the measured impedance also varies, making it difficult to perform reproducible measurements. Moreover**,** the properties of human skin differ for each person. This variability complicates the understanding of the role of hydrated, dry skin and electrode material in the acquisition of biopotential signals. Therefore, the second part of this aim is to fabricate a two-layered skin phantom to mimic the skin's electrical properties in the low-frequency range (1 Hz-1000 Hz) along with controlled hydration status, as there is no explicit control on human variables. Thereafter, the model is developed, and the mechanistic principle of the metal-based dry electrodes is investigated by carrying out benchtop experiments in a controlled manner using the phantom.

1.3.2 Aim 2

To demonstrate the ability to capture clinically relevant Electrocardiogram signals using large dry titanium electrodes from a non-standard location and explain the mechanism for working of large titanium electrodes.

Second, this work then employs this model to evaluate the feasibility of using dry electrodes to capture clinically relevant Electrocardiogram (ECG) signals by using large dry titanium electrodes integrated into a toilet seat cardiovascular monitoring system. Further, the model developed in Aim 1 is used to understand the dependence of skin-electrode contact impedance on material and skin hydration. *In vivo* skin-electrode contact impedance and ECG measurements were conducted across ten healthy human subjects, and quantitative comparisons were performed to compare the ECG signal quality between different electrode configurations. Large titanium electrodes resulted in better signal quality than large stainless steel electrodes.

The toilet seat cardiovascular monitoring system is a device that has been designed for revolutionizing in-home cardiovascular monitoring. Thus, this work demonstrates the use of large dry titanium electrodes to monitor respiration by measuring changes in impedance from the back of the thigh, which may be useful for several conditions including COVID-19 recovery, and progression of edema during heart failure management. Remote transthoracic impedance-based monitoring technique has been used to monitor respiration and the detection of pulmonary edema. In the current work, the measurements are not across the thorax but are across the thighs (a non-standard location); hence this leads to Aim 3.

1.3.3 Aim 3

To understand the sensitivity of respiration and edema detection from the back of the thigh location using finite element method modeling.

The third aim is to characterize the sensitivity of respiratory monitoring from the back of the thigh and to evaluate the feasibility of measuring respiration based on changes in impedance. The feasibility of this approach is investigated empirically, by comparing thorax and thigh-thigh bioimpedance measurements to spirometer measurements. Further, the relationship between thigh-thigh impedance and respiration is investigated computationally, using finite element modeling, by performing bioimpedance simulations on a realistic CAD human model (Visible Human Project-Female from the National Library of Medicine).

1.4 Outline

The work presented in this dissertation consists of four chapters that are based on four peer-reviewed publications, and a future work chapter. Chapter 2 provides an overview of progress made in the field of dry electrodes for biopotential acquisition, based on their mechanistic principles, materials, and testing methods. In Chapter 3 (which covers the second part of Aim 1), the fabrication of the phantom simulating electrical properties of the skin in the low-frequency regime along with controlled hydration status is discussed. It includes the material selection, detailed fabrication process, *in vitro* characterization, and *in vivo* validation of the fabricated phantom. Using the developed phantom simulating dry and hydrated skin, a circuit skin-electrode interface model for dry electrodes is presented in Chapter 4 (which covers the first part of Aim 1). Further, validation of the model is presented via *in vivo* skin-electrode contact impedance measurements, and an ability to capture clinically relevant ECG using dry large titanium electrodes integrated into a toilet seat cardiovascular monitoring system is demonstrated in Chapter 4 (covers Aim 2). In Chapter 5 (covers Aim 3), a novel method of respiration detection from the back of the thigh using the bioimpedance technique is presented and the sensitivity of respiratory monitoring from the back of the thigh and edema detection is discussed. Future work and final remarks are presented in Chapter 6.

References

[1] CDC, “Heart Disease Facts | cdc.gov,” 2022. https://www.cdc.gov/heartdisease/facts.htm (accessed Jun. 05, 2023).

[2] C. W. Tsao *et al.*, *Heart Disease and Stroke Statistics - 2023 Update: A Report from the American Heart Association*, vol. 147, no. 8. 2023. doi: 10.1161/CIR.0000000000001123.

[3] S. S. Virani *et al.*, “Heart disease and stroke statistics—2020 update: A report from the American Heart Association,” *Circulation*. pp. E139–E596, 2020. doi: 10.1161/CIR.0000000000000757.

[4] S. S. Virani *et al.*, *Heart Disease and Stroke Statistics - 2021 Update: A Report From the American Heart Association*, vol. 143, no. 8. 2021. doi: 10.1161/CIR.0000000000000950.

[5] O. Khavjou, D. Phelps, and A. Leib, “Projections of Cardiovascular Disease Prevalence and Costs: 2015-2035,” *RTI Int.*, no. 0214680, pp. 1–54, 2016.

[6] K. Merkley, “Leveraging Healthcare Analytics to Reduce Heart Failure Readmission Rates,” *Health Catalyst*, 2016. https://www.healthcatalyst.com/reduce-heart-failure-readmissions-with-healthcare-analytics/ (accessed Feb. 08, 2021).

[7] R. Nair, H. Lak, S. Hasan, D. Gunasekaran, A. Babar, and K. V Gopalakrishna, “Reducing All-cause 30-day Hospital Readmissions for Patients Presenting with Acute Heart Failure Exacerbations: A Quality Improvement Initiative,” *Cureus*, vol. 12, no. 3, 2020, doi: 10.7759/cureus.7420.

[8] J. Morrissey, “Remote patient monitoring.,” *Medical economics*, vol. 91, no. 13. 2014. doi: 10.1145/2534088.2534108.

[9] “Holter Monitor.” https://en.wikipedia.org/wiki/Holter_monitor (accessed Feb. 08, 2021).

[10] M. O’Connor *et al.*, “Using telehealth to reduce all-cause 30-day hospital readmissions among heart failure patients receiving skilled home health services,” *Appl. Clin. Inform.*, vol. 7, no. 2, pp. 238–247, 2016, doi: 10.4338/ACI-2015-11-SOA-0157.

[11] C. Park *et al.*, “Impact on Readmission Reduction Among Heart Failure Patients Using Digital Health Monitoring: Feasibility and Adoptability Study,” *JMIR Med. Informatics*, vol. 7, no. 4, p. e13353, 2019, doi: 10.2196/13353.

[12] W. T. Abraham *et al.*, “Wireless pulmonary artery haemodynamic monitoring in

chronic heart failure: A randomised controlled trial," *Lancet*, vol. 377, no. 9766, pp. 658–666, 2011, doi: 10.1016/S0140-6736(11)60101-3.

[13] S. Emani, "Remote Monitoring to Reduce Heart Failure Readmissions," *Curr. Heart Fail. Rep.*, vol. 14, no. 1, pp. 40–47, 2017, doi: 10.1007/s11897-017-0315-2.

[14] Alive Technologies, "AliveCor | FDA-cleared EKG at your fingertips. – AliveCor, Inc." https://store.alivecor.com/ (accessed Feb. 08, 2021).

[15] Apple Inc, "Taking an ECG with the ECG app on Apple Watch Series 4 or later," *Support.Apple.Com*, 2019. https://support.apple.com/en-us/HT208955 (accessed Feb. 08, 2021).

[16] C. Gyllensten, "Monitoring heart failure using noninvasive measurements of thoracic impedance," 2018. [Online]. Available: https://pure.tue.nl/ws/files/97474897/20180627_Cuba_Gyllensten.pdf

[17] S. Dovancescu *et al.*, "Detecting Heart Failure Decompensation by Measuring Transthoracic Bioimpedance in the Outpatient Setting: Rationale and Design of the SENTINEL-HF Study," *JMIR Res. Protoc.*, vol. 4, no. 4, pp. e121, 1–13, 2015, doi: 10.2196/resprot.4899.

[18] N. J. Conn, "Robust Algorithms for Unattended Monitoring of Cardiovascular Health," 2016. [Online]. Available: https://scholarworks.rit.edu/theses/9277/

[19] M. Shochat *et al.*, "Prediction of cardiogenic pulmonary edema onset by monitoring right lung impedance," *Intensive Care Med.*, vol. 32, no. 8, pp. 1214–1221, 2006, doi: 10.1007/s00134-006-0237-z.

Chapter 2: A Review on Dry Electrode Performance

Published as **K. Goyal** and S.W. Day, "Factors affecting Wearable Electrode Performance and Development of Biomimetic Skin Phantom" In New Advances in Biosensing. 2023. DOI: 10.5772/intechopen.111429

2.1 Abstract

In-home physiological monitoring devices enable the monitoring of vital health parameters and can facilitate health recovery. The current state of the art is inclined towards non-invasive technologies such as wearable mobile devices and patch-based sensors. In this chapter, we provide an overview of progress made in the field of dry electrodes for biopotential acquisition, based on their mechanistic principles, materials, testing methods, and effectiveness in a real-world setting. Important parameters affecting the dry electrode performance such as the area, material, applied pressure and skin hydration are discussed. Traditionally, the development and testing of these wearable electrodes are conducted empirically, *in vivo* on human skin. However, due to the inter- and intra-subject variability in human skin properties, reliability, repeatability, and the efficacy of the device under investigation cannot be evaluated. Thus a review is presented about the skin phantoms used to simulate the electrical properties of the skin, which has the potential to serve as a robust method to test the functionality of current and future electrodes. This retrospective overview provides researchers with an understanding of the mechanistic principle of biopotential

electrodes and the crucial factors that affect electrode performance, thus facilitating wearable electrode development.

Keywords: Dry electrodes, Skin phantoms, Biopotential signals, Wearable devices, Non-invasive, Skin-electrode impedance.

2.2 Introduction

In-home physiological monitoring, also known as remote patient monitoring, enables long-term tracking of patients' health from the comfort of their homes without the need to visit a clinic. It has the potential to facilitate a healthcare transformation from reactive to proactive preventive care. In-home physiological monitoring of biopotential (voltage) signals such as an Electroencephalogram (EEG), Electrocardiogram (ECG), and Electromyogram (EMG) enables tracking daily changes in a patient's health [1]. The current state of the art for in-home monitoring is inclined towards non-invasive technologies such as wearable mobile devices and patch-based sensors (Figure 2.1). In both technologies a biopotential electrode picks up voltage signals from the surface of the body and acts as an interface between the tissue and the electronics.

This chapter is focused on the mechanism of *dry electrodes*, but we include here a brief description of the most common type of biopotential electrode, the *wet electrode*. A wet electrode is an electrochemical electrode and consists of two major parts: the metal plate and the electrolyte. An example of a wet electrode is an ECG disposable electrode commonly used in clinical settings. It consists of an electrochemically active gel (this acts as an electrolyte and contains conductive ions), which is in direct contact with both the skin and the metallic part of the electrode, the inside of which is coated with Ag/AgCl and the outside is connected to a metal snap. The whole assembly is mounted on a flexible foam pad and contains adhesive for ease of attachment to the body. Due to the adhesive, wet electrodes stay in contact with the skin while the person is moving and can compensate for the motion artifacts. However, there are certain drawbacks of using the wet electrodes: the skin needs to be prepared by a skilled person; the gel dries over time, leading to signal degradation; and the removal of the gel electrodes is often painful or leads to skin irritation.

To overcome the limitations of wet electrodes, dry electrodes are being integrated into wearable devices such as watches and hand-held monitoring devices thus making them user-friendly. The mechanistic principle involved in the functioning of dry electrodes is important to understand and is different from that of wet electrodes, and is discussed in section 2.3. Based upon this mechanistic principle, this chapter provides a brief overview of different types of dry electrodes that exist in the literature. Factors such as the electrode area, material, applied pressure, and skin hydration that affect the electrode performance are presented in section 2.4. This is followed by a discussion of the existing methods for testing the performance of these electrodes in section 2.5. Finally, the chapter summarizes the key findings about the factors that affect electrode performance along with suggestions for future directions to aid wearable electrode development.

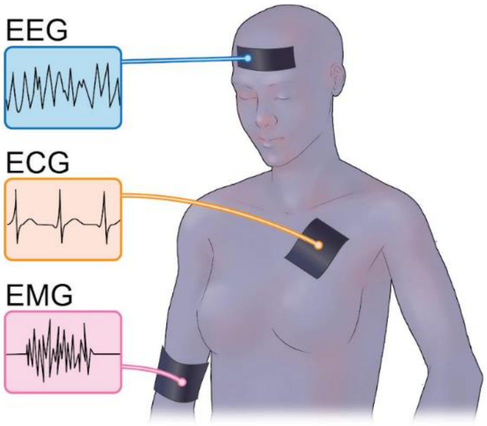

Figure 2.1. Biopotential signals acquisition such as Electroencephalogram (EEG), Electrocardiogram (ECG), and Electromyogram (EMG) using wearable electrodes on the skin.

2.3 Electrodes for Biopotential Acquisition

A lot of attention has been paid to ECG because of the clinical significance of heart disease, the ability to diagnose arrhythmias from biopotential, and the utility of long-term monitoring of ECG for some conditions that only occur intermittently and may therefore be missed in the clinic. Clinically, ECG is captured using wet electrodes. Some wearable devices, such as the Holter Monitor, capture ECG using wet electrodes on the skin and provides an ambulatory electrocardiogram [2]. Such a wearable device's benefits include a portable device that is worn for a short time (24–72 hours) to determine if the subject has any occasional cardiac arrhythmias, but they do face the challenges associated with wet electrodes mentioned earlier, such as being uncomfortable and leading to skin irritation. Because of this, there is a lot of research and development activity to implement an ECG system using dry electrodes. Although not an exhaustive list, two of these are described here. One such device is KardiaMobile by AliveCor, a US-based company [3]. It is a hand-held device and can detect atrial fibrillation (an irregular and rapid heart rate). It uses two 3cm x 3cm stainless steel electrodes and provides single-lead ECG. Dry electrodes are also being integrated into wearable devices such as watches. One such device is an Apple watch series 4. It also measures a single-lead ECG and consists of two electrodes. The button on the side of the watch (digital crown) made up of titanium serves as one of the electrodes, and the back crystal electrode on the back of the apple watch serves as another electrode. It consists of an ultrathin chromium silicon carbide nitride layer that is applied to the sapphire crystal. The wrist of the user is always in contact with the watch and the user needs to apply his fingertip across the crown, which creates a closed circuit, and this ECG can be recorded using the ECG app. Although dry electrodes are more user-friendly, they generally lead to poorer quality signals, due to the different mechanistic principles of the wet and dry electrodes, which are discussed in the following section.

2.3.1 Mechanistic Principle of Wet Electrodes

2.3.1.1 Electrochemical reactions of electrode/electrolyte interface

The mechanistic principle of a wet electrode is based on an electrode-electrolyte interface's electrochemical reactions. When a metal electrode comes in contact with an electrolyte solution, redox reactions may occur at the interface. The redox reactions occurring at the electrode/electrolyte interface are complex, but mechanistic models have been proposed that describe this interface as the *double layer* structure. The very first model was proposed by Helmholtz [4] and then modified by Gouy [5], Chapman [6], Stern [7], and Grahame [8], and followed by Bockris, Devanathan, and Muller with what is known as the BDM model [9]. Details for the double layer structure can be found elsewhere [10], [11] but are described here in brief in the context of the workings of a wet electrode by means of the double-layer structure at the interface of an Ag/AgCl electrode immersed in an electrolyte containing NaCl (Figure 2.2) [12].

The electrochemical reactions occur at the liquid electrode interface when the Ag/AgCl electrode is immersed in an electrolyte containing Na+ and Cl- ions. First, the oxidation reaction occurs at the Ag electrode interface with the AgCl coating, which results in an excess of Ag+ ions. The Ag+ ions move into the AgCl and fill up the vacancies or move the adjacent Ag+ ions to an interstitial site. Further, the Ag+ ion interacts with the Cl- ions in the electrolyte. Hence it leads to the precipitation of AgCl at the interface of AgCl and the electrolyte. Also, there is a dissolution of AgCl, as the Ag+ ions in AgCl prefer to be reduced. The Cl- ions get dissolved in the electrolyte, which leads to a higher concentration of Cl- ions at the interface than at the bulk of the electrolyte. Thus, to neutralize the negatively charged plane, the Ag electrode becomes positively charged, and these two planes form a double layer structure, and there appears a potential difference across the electrode/electrolyte interface. The electrochemical reactions can be described by the following equations [12] :

$$\mathrm{Ag} \rightarrow \mathrm{Ag}^{+} + \mathrm{e}^{-} \text{ (Oxidation)}$$

$$\mathrm{Ag}^{+} + \mathrm{Cl}^{-} \longrightarrow \mathrm{AgCl} \text{ (Precipitation)}$$

$$\mathrm{AgCl} \rightarrow \mathrm{Ag}^{+} + \mathrm{Cl}^{-} \text{ (Dissolution)}$$

$$\mathrm{Ag}^{+} + \mathrm{e}^{-} \longrightarrow \mathrm{Ag} \text{ (Reduction)}$$

The potential difference across the electrode/electrolyte interface causes the rearrangement of Cl- ions and leads to the orientation of water molecules. The water molecules align due to their dipole nature. Some Cl- ions are specifically adsorbed on the AgCl surface. There also happens to be the electrostatic attraction of Cl- ions by the positive charges of the Ag/AgCl electrode. This process can be described as the formation of planes, the inner Helmholtz plane IHP and the outer Helmholtz plane (OHP). The plane crossing the center of the water molecules is called IHP, and the plane crossing through the center of the aligned Cl- ions is known as OHP. The two positively (Ag/AgCl) and negatively charged planes (OHP) act as two plates of a parallel plate capacitor, and thus can be described as a capacitor. It is also known as the Stern layer. Due to the thermal driving forces and electrostatic attraction, there is a diffusion of the other Cl- ions in the electrolyte. The concentration of Cl- ions decreases exponentially; it is known as the diffusion layer. The diffusion layer ends when there is no potential gradient, which is represented by the bulk electrolyte. The double-layer structure is formed by the combination of the stern layer and diffusion layer. It can be considered the two layers connected in the series and can be described by the following expression, where C_{dl} is the double layer capacitdance, C_H is the Helmholtz layer capacitance, and C_{GC} is diffusion layer capacitance (Gouy- Chapman) :

$$\frac{1}{C_{dl}} = \frac{1}{C_H} + \frac{1}{C_{GC}} \qquad (1)$$

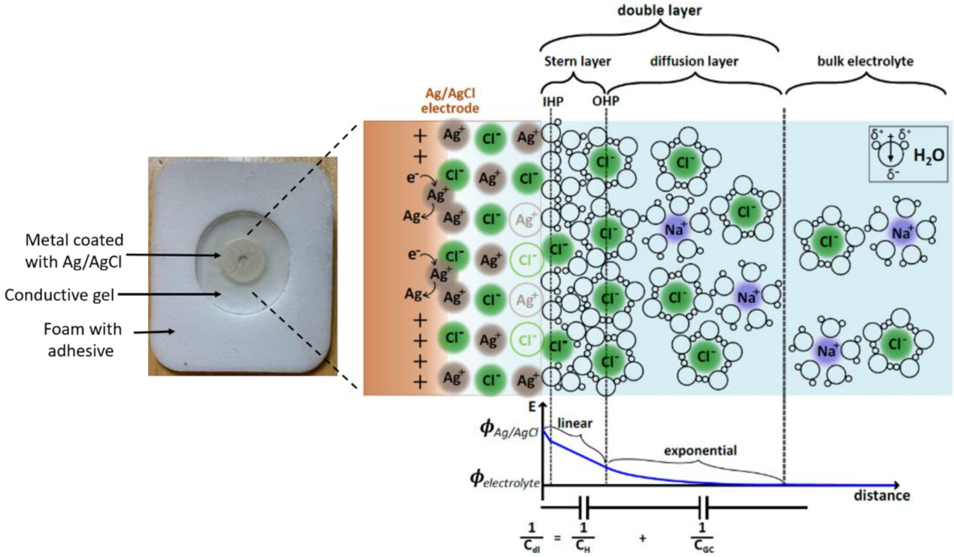

Figure 2.2. An example image of a typical wet electrode is shown. The zoomed-in view represents the electrode-electrolyte interface for a wet electrode depicting the double layer structure and an electric field of the interface, where IHP is the inner Helmholtz plane and OHP is the outer Helmholtz plane (Image modified from reference [12]).

2.3.1.2 Equivalent electrical circuit for electrode/electrolyte interface

Electrically, the electrode/electrolyte interface and the skin can be represented by a combination of resistor and capacitor networks. The double layer is formed at the interface of two different phases. If there are any electrochemical reactions at the interface, they take place in the double-layer structure, leading to the faradaic current. Faradaic current is the current generated by the redox reactions at the electrode. The double-layer structure is represented by a capacitor (C_{dc}), while the faradaic current flowing through it due to electrochemical reactions can be expressed as leakage current of the capacitor and is represented by a resistor in parallel (R_d) [13]. It is also known as charge transfer resistance and can be represented as R_{ct}. Thus, in wet electrodes, due to this charge transfer phenomenon, resistive coupling is dominant. In this work, as shown in Figure 2.3, R_{ct} is used to represent the charge transfer resistance, C_{dc} as the double-layer capacitance, and the resistance offered by the electrolyte is represented by R_g.

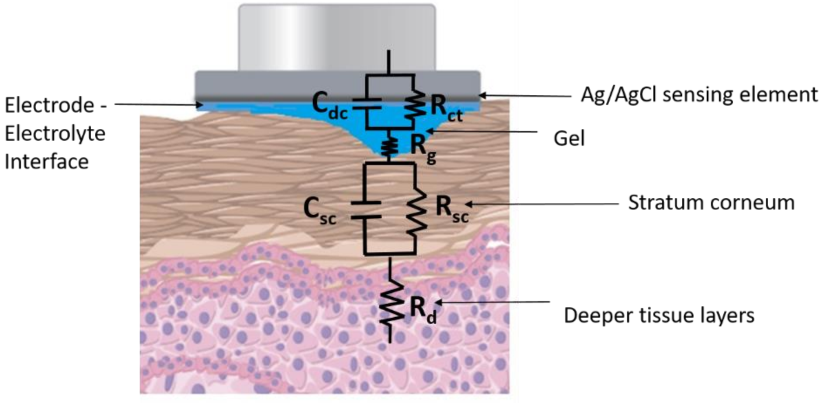

Figure 2.3. An analogous electrical equivalent circuit of the wet electrode. Electrode-electrolyte interface is shown, where R_{ct} and C_{dc} represent the charge transfer resistance and double-layer capacitance respectively. R_g represents the resistance in the gel/electrolyte. The stratum corneum is shown as a parallel combination of resistor (R_{sc}) and capacitor (C_{sc}), and deeper tissue layers as a resistor (R_d).

2.3.1.3 Equivalent electrical circuit for skin

The electrode-skin interface plays an important role in measuring biopotential signals. The anatomical structure of skin comprises different layers. It can be broadly divided into the epidermis, dermis, and subcutaneous tissues. The topmost layer of the epidermis is the stratum corneum (SC), which consists of dead cells and is also referred to as the horny layer [14]. The outermost layer has the highest electrical resistance as it consists of dead cells. The layer beneath the epidermis is known as the dermis and mainly consists of blood vessels and sweat glands. Sweat ducts penetrate the stratum corneum, and as the sweat emerges, it results in a low-resistance parallel pathway. Sweat is considered a weak electrolyte and thus the flow of sweat across the duct walls leads to an increase in the stratum corneum's hydration. Hence, this causes variation in the conductance of the skin. The skin can be represented electrically by equivalent capacitor and resistor configurations.

Electrical conduction inside the body is ionic. The stratum corneum contains sweat ducts and hair follicles that contain an ionic liquid and traverse the SC, therefore allowing electrical conduction across the SC. Hence it can be represented as a resistor. Stratum corneum consists of dead cells, and from an electric standpoint, it can be considered an insulator between the electrode (one plate of the capacitor) and the other living conductive tissues underneath it (another plate of the capacitor). Hence, it can be represented by a capacitor. The skin can be modeled as a capacitor and resistor in parallel. Several investigators have studied human skin's electrical properties in response to AC signals and found skin impedance is of the order of 100Ω at high frequencies and 10 kΩ-1MΩ at low frequencies (below 1 kHz) [15]. Figure 2.3 shows an equivalent circuit model where R_{sc} and C_{sc} represent the resistance of the stratum corneum, and R_d represents the resistance of the deeper tissue layers.

In wet electrodes, the electrolyte/gel helps in facilitating the electrochemical reactions and hydrates the stratum corneum, thus providing conductive ions that create an easier ionic path between the electrode and the skin below the stratum corneum [16]. The gel further helps in lowering the skin-electrode impedance by reducing R_{sc} and increasing C_{sc}. However, the gel dries over time, which leads to an increase in R_g, $R_{sc,}$ and a decrease in C_d, and C_{sc}. In addition to this, Huigen et al. revealed that the main origin of the noise in the surface electrodes is due to the electrolyte-skin interface and is highly dependent on the electrode gel [17]. Thus, to overcome the limitations and challenges of wet electrodes, efforts have been made in the field of dry electrodes.

2.3.2 Mechanistic Principle of Dry Electrodes

In contrast to *resistive coupling* in wet electrodes, dry electrodes are free of gel, and thus in the absence of any sweat has no ionic fluid coupling from the skin to the electrode, and the mechanistic principle is fundamentally different [18] and referred to as *capacitive coupling*.

In the capacitive coupling associated with dry electrodes no actual charge crosses the skin/electrode interface, as the metal electrode being an inert metal is difficult to oxidize or dissolve [14]. A displacement current exists as a result of capacitance at the interface and the signal gets capacitively coupled from the body to the sensing electrodes [19]. The heart causes immediate changes in the electric potential within the tissue, which is sensed by the metal electrodes. The metal electrode acts as one plate of a capacitor, with the deeper tissue layers as the other plate of the capacitor. The thin metal native oxide, air gaps, and the dry outer layer of the skin (stratum corneum) together act as a *dielectric* (the space between plates of a capacitor) [18]. Thus C_c varies as per equation (2), where the capacitance is directly proportional to the relative permittivity and area, and inversely proportional to the distance between two plates. Further, the capacitive impedance holds an inverse relation to the capacitance given by equation (3). Based upon this mechanistic principle of dry electrodes, different types of electrodes are reviewed in section 2.3.3.

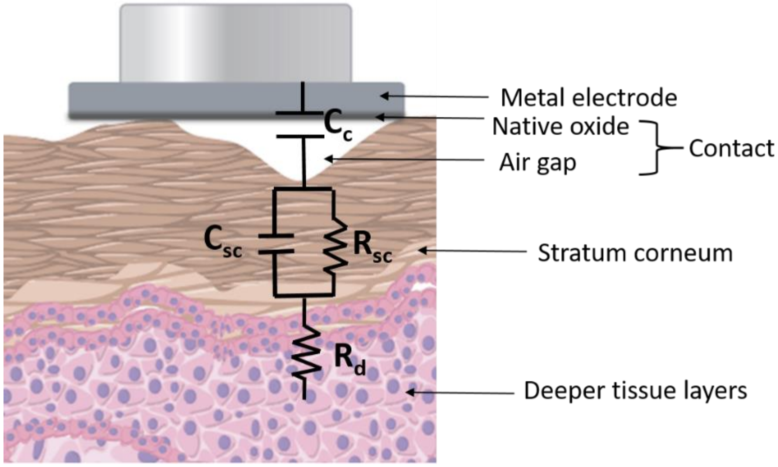

Figure 2.4. An analogous electrical equivalent circuit for the metal-based dry electrode. Contact is represented by a capacitor (Cc), along with the stratum corneum as a parallel combination of resistor (Rsc) and capacitor (Csc), and deeper tissue layers as a resistor (Rd). The air gaps are due to the surface roughness of the stratum corneum and stiff metal-based dry electrodes. Cc comprises both the air gaps and the thin native oxide that comes in direct contact with the skin.

$$C = \frac{\varepsilon_0 \varepsilon_r A}{d} \qquad (2)$$

$$Z_c = \frac{1}{\omega C} \qquad (3)$$

Where ε_0 is the relative permittivity of free space, ε_r is the relative permittivity of a material, A is the area of the plate, and d is the distance between the two plates, $\omega = 2\pi f$, ω is in rad/s, and f is the frequency (Hz).

2.3.3 Types of Dry Electrodes

Dry electrodes can be broadly classified into two major categories: contact and non-contact electrodes. As the name suggests, contact electrodes are in direct contact with the skin and can be made from a range of materials, including metal, textile, and polymer electrodes. Metal-based electrodes use metal plates such as stainless steel, silver, titanium, and gold [16], [20]–[22]. These provide ease of manufacturing, integration, and use, but due to the lack of an electrolyte and flat hard surfaces, it is difficult to achieve good contact with dry and hairy skin. This results in an increase in resistance of the stratum corneum (R_{sc}) and a decrease in stratum corneum capacitance (C_{sc}) and contact capacitance (C_c). It leads to high skin-electrode contact impedance, which leads to poor signal quality. Efforts have been made to embed the metal-based electrodes on a foam structure for ease of wearing [20], [23].

Several investigators have worked on fabricating dry electrodes based on the use of textiles in place of stiff metals [24], [25]. Textiles-based electrodes are made using conductive thread, steel, yarn, or silver coated on nylon fabric. These electrodes can be embedded within clothing and used as smart garments to sense biopotential signals [26], [27]. Due to flexibility, there is an increase in the effective skin contact area compared to the metal-based electrode, which decreases the R_{sc} and increases the C_{sc} and C_c, thus lowering the overall impedance. But still, the challenges of high skin-electrode contact impedance remain the same due to the absence of an electrolyte.

To enhance elasticity, electrodes have been fabricated on polymeric substrates like polyethylene terephthalate (PET) and coated with conductive polymers such as MWCNT/PDMS [28]. Another polymer material, such as PEDOT, poly (3,4-ethylenedioxythiophene), is coated on metal electrodes to enhance the electrochemical performance, as it would lead to an increase in C_c [29]. But often, fabrication is complex, and in the long run, polymers usually flake off. Another type of dry contact electrodes includes microtips/pin based. The surface of the electrodes coming into contact with the skin consists of pins/spikes. The pin’s height is of the order of 150 μm, which is sufficient to penetrate the 20 μm thick stratum corneum. Thus this leads to a lower value of R_{sc} and a higher value of C_{sc}. Hence, the pins directly come into contact with the fluids underneath the stratum corneum, which acts as an electrolyte, and eventually, the spike electrodes behave like wet electrodes. Though the application of pin electrodes can overcome the high impedance of the stratum corneum [30], their use can lead to skin irritation and infections as they come into contact with fluids underneath the skin. There are other types of electrodes, which do not make direct contact with the body, which thus can be categorized as non-contact electrodes [31]. These electrodes are worn on top of clothing, and can acquire biopotential signals through clothing [32]–[35]. The addition of clothing further increases the contact impedance, thus increasing the R_{sc} and decreasing the C_c and C_{sc}.

2.4 Significant parameters for dry electrodes

In this section, several factors affecting dry electrode performance such as the electrode area, electrode material, skin hydration, and pressure are discussed. In addition to the high skin-electrode impedance of the dry electrodes, the skin-electrode impedance is variable with the applied pressure. Major factors that should be considered in the development of new electrode designs and their contribution to the skin-electrode interface have been summarized in Table 2.1.

2.4.1 Electrode Area

Researchers have tried to overcome the challenges of dry electrodes by increasing the area of the electrode [28], [36]. Electrode-skin impedance plays a major role in the biopotential signal quality. With an increase in the electrode area, the R_{sc} decreases (Resistance is inversely proportional to the area), and both C_c and C_{sc} increase, which leads to a decrease in Z_c. Thus, it leads to an overall decrease in skin-electrode impedance with an increase in the area of the electrode. This approach of increasing the area to achieve lower skin-electrode contact impedance is useful and effective, however, it has a limited application in devices such as wearables where small electrode size is necessary for devices to be practical as wearables. This is particularly true for watch type devices, which require very small ($<1cm^2$) electrodes.

2.4.2 Electrode Material

Another aspect to improve the quality of biopotential signal acquisition is using different electrode materials [20], [37], [38]. The classical approach followed by researchers for characterizing different electrode materials is entirely empirical, and consists of carrying out experiments with different chosen materials followed by qualitative or quantitative comparison with wet electrodes (gold standard) [20], [37]–[39]. After that, the most satisfactory material based on the performance is selected. Some researchers have used the equivalent circuit electrode-skin interface impedance models and fitted them in the electrochemical impedance spectroscopy experimental data to characterize the wet and dry electrodes [40]. Typically, equivalent-skin interface models have been used to demonstrate the role of the size of electrodes on skin-electrode contact impedance, which clearly depicts the decrease in skin-electrode impedance with an increase in the electrode area. However, the role of electrode material (typically metal-based) in the skin-electrode interface is not reported. In one of the recent studies [18], efforts were made to understand the rationale behind a “metal-based electrodes’” material performance. The electrode-skin impedance dependence on the electrode material was investigated by developing a skin-electrode interface model that includes aspects of prior models and incorporates a model of the electrode material. The findings of this work suggested that the relative permittivity of the electrode material native oxide plays a significant role and a higher value leads to an enhanced capacitive coupling and thus a lower skin-electrode impedance. As per equation (2), a higher relative permittivity ε_r leads to increase in C_c which further leads to lower Z_c, thus lower skin-electrode impedance. However, the skin properties R_{sc} ad C_{sc} are not affected by the change in the electrode material, but C_c can be improved significantly. Thus, investigating dielectric properties, such as thickness, and relative permittivity of the native oxide, can be one of the approaches when selecting material for biopotential electrodes.

2.4.3 Skin Hydration

The impedance of the stratum corneum is greatly affected by changes in skin hydration. According to one study, the stratum corneum resistance (R_{sc}) decreases by 14 times, and capacitance (C_{sc}) increases by 1.5 times under hydrated conditions as compared to dry skin [41]. The increased capacitance (C_{sc}) is attributed to the fact that hydration significantly affects the dielectric properties of the stratum corneum. As per previously reported findings, the relative permittivity of dry stratum corneum is 10 [41] and that of hydrated SC is 49 [42], which suggests an increase in the C_{sc}. Moreover, hydrated skin leads to higher C_c, thus enabling enhanced capacitive coupling. The increased contact capacitance can be attributed to the improved contact between the electrode and stratum corneum [18].

Thus hydration plays an important role in lowering the stratum corneum impedance and is the most significant factor in achieving a low skin-electrode impedance.

2.4.4 Pressure

For dry electrodes, researchers have made efforts to understand the role of applied pressure on electrode performance [43], [25], [36]. An increase in applied pressure results in a lower skin-electrode impedance and this can be attributed to the increase in the effective contact area due to applied pressure. As per equation 2, the increase in the effective electrode contact area leads to an increase in both C_c and $C_{sc.}$ In addition to this, there is a decrease in R_{sc} as resistance is inversely proportional to the area. Changes in the applied pressure affect the skin-electrode impedance significantly, which further impacts the signal quality. Therefore, applied pressure should be accounted for during the testing of wearable devices.

2.4.5 Summary of Effects

The factors discussed in the above section and the impact on each parameter of the circuit model, along with the net effect on skin-electrode impedance are summarized in the Table below.

Table 2.1. Different factors that affect the electrode performance and the equivalent impedance fitting parameters that will be affected corresponding to these factors are shown. R_{sc} represents the resistance of the stratum corneum, respectively; C_{sc} and C_c represent the capacitances of the stratum corneum and contact.

Factors affecting Electrode Performance	**R_{sc}**	**C_{sc}**	**C_c**	**Net effect on Impedance**
Electrode Material	No change	No change	Changes	Changes
Increase in Electrode Area	Decreases	Increases	Increases	Decreases
Increase in Pressure	Decreases	Increases	Increases	Decreases
Increase in Skin Hydration	Decreases	Increases	Increases	Decreases

2.5 Testing method of Dry Electrodes

This section reviews the existing methods used for developing and testing the newly designed dry electrodes. The existing methods has been broadly classified into *in vivo* and *in vitro* type of testing. *In vitro* testing of dry electrodes refers to the evaluation of the performance of wearable electrodes across the human subjects, and *in vitro* testing refers to evaluating the electrode performance on a platform (aritifical skin) that has similar properties to that of human skin.

2.5.1 *In Vivo* Testing

Historically, the development and testing of electrodes are empirically performed by conducting experiments *in vivo* on human volunteers. This method of testing has two limitations: First, the properties of the human skin change over time, which leads to changes in the skin impedance, thus making it challenging to perform reproducible measurements [24]. Secondly, the properties of human skin differ for each person. Hence, the intra and inter-subject variability complicate the understanding of the performance of the dry electrodes in the acquisition of biopotential signals. Therefore, the performance of electrodes cannot be investigated and the role of various electrode parameters including electrode material, and applicability of the electrode design to a wider range of populations, cannot be clearly understood.

2.5.2 *In Vitro* Testing

To overcome the limitations of *in vivo* testing, some efforts have been made to fabricate a synthetic model of skin and tissue. These so-called *phantoms* simulate the electrical properties of tissues. The phantoms can be used as controlled benchtop testing platforms and can be used to facilitate the development of the electrode designs as there is no explicit control on human variables.

Figure 2.5 shows the electrical properties of two layers of the skin, which comprise the topmost layer known as the stratum corneum, and all the inner layers of the skin other than the stratum corneum, which are considered dermis/deeper tissue layers. The electrical properties of the stratum corneum represented in Figure 2.5 were investigated in one of the initial research works by Yamamoto et al. [44], where the stratum corneum was removed from a forearm of a human subject with a cellulose adhesive tape. The keratin layers of the stratum corneum were removed stepwise by stripping the skin with the cellulose tape and the electrical properties of the dermis and stratum corneum were studied. The impedance of the stratum corneum accounts for a major portion of the whole impedance measured at the skin, and it dominates in the low-frequency range between 1 Hz to 10 kHz. The region of interest in electrophysiological signals is low-frequency regions, and the stratum corneum impedance plays the dominant role in the low-frequency region. In this section, the existing phantoms have been broadly classified into single-layered and two-layered phantoms.

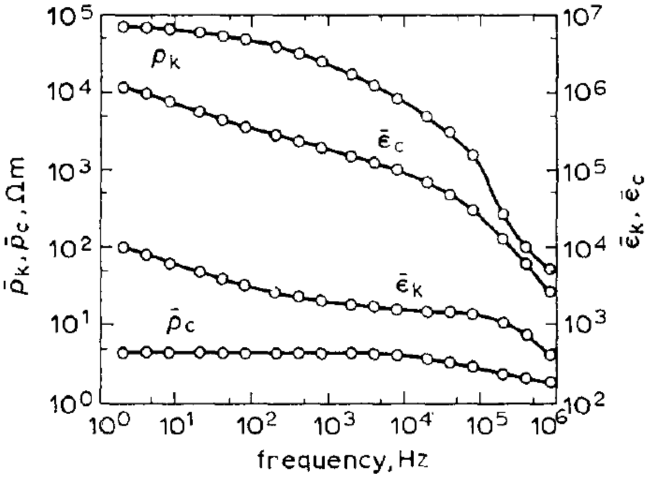

Figure 2.5. Electrical properties of two layers of skin, where ρ_k and ε_k are average resistivity and dielectric constants of stratum corneum; ρ_c and ε_c are average resistivity and dielectric constants of inner layers (dermis) (Image reproduced from reference [44])

2.5.2.1 Single-layered phantom

Skin phantoms, also known as artificial/synthetic skin, are made using different materials to mimic various kinds of skin properties. Skin properties can be broadly categorized into surface, mechanical, acoustic, optical, electrical, and thermal properties. For mimicking electrical properties, gelatinous substances and elastomers are mostly used [45]. Several researchers have fabricated skin phantoms using gelatinous substances such as gelatin [24] and agar [15], [46]. The agar-based phantom’s electric and dielectric properties can be adjusted by adding NaCl and polyethylene powder, respectively. Using this approach, Ito et al. fabricated the conventional electromagnetic phantom as a whole layer and used it to mimic electrical properties for higher frequency ranges (300 MHz - 2.5 GHz) [47]. Later on, Yamamoto et al. used the above approach and further tuned electrical properties by adding the carbon microcoil to increase the relative permittivity of the phantom and thus fabricated a phantom that simulated electrical properties ranging between 1 MHz up to 2.5 GHz. However, the hydrous phantoms couldn't be further tuned to mimic the electrical properties for frequencies below 1 MHz [48]. Thus, the conventional approach using agar, DI water, NaCl, and polyethylene simulate the electrical characteristics of a high-content water tissue such as muscle and brain, and is incapable of simulating the electrical properties of the skin

In another such work, Kalra et al. fabricated a single-layer phantom using oil in gelatin for simulating dielectric properties in a low-frequency range (20 Hz-300 kHz). However, the results are four orders of magnitude away from the desired skin dielectric properties in the low-frequency range [49]. A similar approach using gelatin was followed for fabricating a phantom for electrophysiology in the recent work of Owda et al. A single-layer phantom was made, and efforts were made to tune the electrical properties with different gelatin and NaCl concentrations [50]. The contact impedance profile was compared for the developed gelatin-based phantom and ex vivo porcine skin over 20-1000 Hz [50]. However, the impedance of human skin is much higher than that of porcine skin. For biopotential signals, the stratum corneum impedance is of interest as it dominates the skin impedance in the low-frequency range (1 Hz to 10 kHz) [51]. Therefore, a single-layer phantom approach does not include the effect of the outer layer of skin. Hence, there is a need for a two-layered skin phantom.

2.5.2.2 Two-Layered phantom

One of the two-layered artificial skin phantoms using elastomers was developed by Nachman et al. [52] to study the mechanical properties such as friction of dry and moist skin. The model consisted of two different layers, a hydrophilic silicone-based top layer, and a polyurethane-based dermis. But, the materials were selected to mimic the elastic modulus properties [52]. Another two-layered artificial skin phantom demonstrating both electrical and mechanical properties was demonstrated by Liu et al. [53]. The skin phantom consisted of a gelatin membrane mimicking the epidermis, SU-8 photoresist mimicking stratum corneum, and microholes mimicking sweat pores and simulating the electrical properties of skin in the frequency range of (20 Hz – 1MHz). However, this frequency range is still too high of a frequency range for characterizing the biopotential electrodes.

Since biopotential signals lie in the range of 1 Hz - 1000 Hz, and hydration plays a significant role in the skin-electrode impedance, none of the phantoms described above are capable of simulating the range crucial for modeling the hydration state. To fill this gap, in one of our previous works [54], a two-layered phantom was simulated, where the two layers represent the deeper tissues and stratum corneum. The lower layer of the phantom mimicking deeper tissues was fabricated using a mixture of polyvinyl alcohol cryogel (PVA-c) prepared with 0.9% W/W saline solution. The upper layer representing the stratum corneum was simulated using a 100 µm-thick layer fabricated by spin-coating a mixture of polydimethylsiloxane (PDMS), 2.5% W/W carbon black (CB) for conductance, and 40% W/W barium titanate ($BaTiO_3$) as a dielectric. The hydration of the stratum corneum was modeled in a controlled way by varying the porosity of the phantom's upper layer. Steps for fabricating the two-layered phantom are shown in Figure 2.6 [54]. The fabricated phantom was found to simulate electrical properties in the range of 1 Hz – 1000 Hz, and matched well with the physiological skin impedance of human subjects. Moreover, with the novel approach of change of porosity, it provides a capability to simulate the hydration in a controlled manner and the phantom can be tuned as per skin ranges among different individuals.

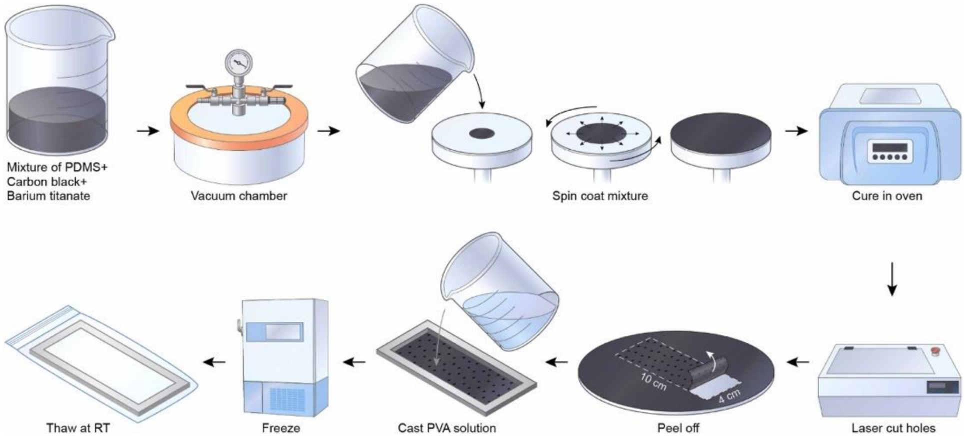

Figure 2.6. Fabrication steps of a two-layered phantom. Clockwise from top-left: a mixture of PDMS, Carbon black, barium titanate; followed by removal of air bubbles in the vacuum chamber; Spin coat mixture at 1000 rpm and 30 s; Cure in an oven at 80 °C for two hours; Laser-cut holes; Peel off the layer; Cast PVA solution; Freeze (12 h at −20 °C); Thaw (24 h at RT). (Reproduced from reference [54])

2.6 Conclusion and Future Outlook

This chapter reviews the factors that affect wearable electrode performance, which are important to understand for the development of these electrodes. The mechanistic principle along with an electrical equivalent circuit for both wet and dry electrodes is discussed that explains the differences in the transduction mechanism of wet and dry electrodes. Various types of dry electrodes have been briefly covered to highlight the current state of art. Efforts made by researchers in developing different types of dry electrodes in a detailed manner can be found in the literature in recent review papers [55]–[58]. Several factors such as the electrode area, skin hydration, electrode material, and pressure that substantially impact the performance of the dry electrodes and their contribution to the individual parameters of the electrical model are discussed. This review suggests that higher relative permittivity of the electrode material's native electrode, an increase in electrode area, the application of pressure, and hydrated skin can help in achieving lower skin-electrode impedance. Thus, these factors can be used for the development of wearable biopotential electrodes, to improve high-quality biopotential signals. In addition to the consideration of the factors for the development of the electrodes, testing the wearable electrodes in a controlled way is crucial for evaluating their performance. Thus several research efforts to fabricate the skin phantoms simulating the electrical properties of the skin across a broad frequency range of 1 Hz – 300 GHz are reviewed. Based on this review, phantoms simulating the electrical properties of the skin across their corresponding frequency range are shown in Figure 2.7. In addition to this, the skin phantom that is capable of simulating the electrical properties of stratum corneum in the frequency range crucial for biopotential signals (1 Hz – 1000 Hz) along with the controlled hydration status is discussed, which can be used to model the interaction of dry electrodes.

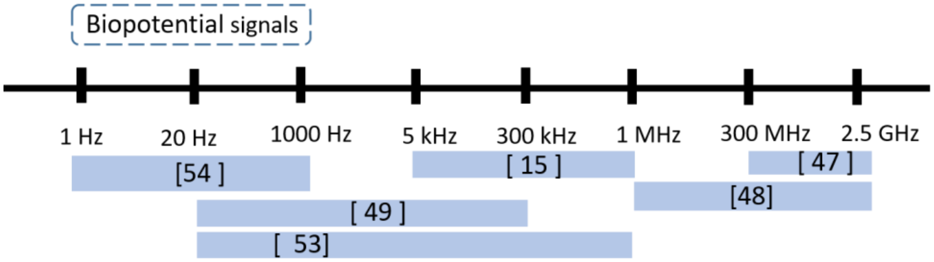

Figure 2.7. Summary of the fabricated skin phantoms across the different frequency ranges. Numbers in square brackets show the reference numbers.

References

[1] S. R. Steinhubl *et al.*, "Effect of a home-based wearable continuous ECG monitoring patch on detection of undiagnosed atrial fibrillation the mSToPS randomized clinical trial," *JAMA - J. Am. Med. Assoc.*, vol. 320, no. 2, pp. 146–155, 2018, doi: 10.1001/jama.2018.8102.

[2] "Holter Monitor." https://en.wikipedia.org/wiki/Holter_monitor (accessed Feb. 08, 2021).

[3] Alive Technologies, "AliveCor | FDA-cleared EKG at your fingertips. – AliveCor, Inc." https://store.alivecor.com/ (accessed Feb. 08, 2021).

[4] H. Von Helmholtz, "Studies of electric boundary layers," *Wied. Ann*, vol. 7, pp. 337–382, 1879, doi: https://doi.org/10.1002/andp.18792430702.

[5] M. Gouy, "Sur la constitution de la charge électrique à la surface d'un électrolyte," *J. Phys. Theor. Appl*, vol. 9, no. 1, pp. 457–468, 1910, doi: 10.1051/jphystap:019100090045700.

[6] D. L. Chapman, "A Contribution to the Theory of Electrocapillarity," *London, Edinburgh, Dublin Philos. Mag. J. Sci.*, vol. 25, no. 148, pp. 475–481, 1913, doi: https://doi.org/10.1080/14786440408634187.

[7] "Stern bilayer - Wikipedia." https://de.wikipedia.org/wiki/Stern-Doppelschicht (accessed Dec. 12, 2022).

[8] D. C. Grahame, "The Electrical Double Layer and the Theory of Electrocapillarity," *Chem. Rev.*, vol. 41, no. 3, pp. 441–501, 1947, doi: 10.1021/cr60130a002.

[9] J. O. M. Bockris, M. A. V Devanathan, and K. Muller, "On the structure of charged interfaces," *Proc. R. Soc. London. Ser. A. Math. Phys. Sci.*, vol. 274, no. 1356, pp. 55–79, 1963, doi: 10.1098/rspa.1963.0114.

[10] Wikipedia, "Double layer (surface science) - Wikipedia," *Wikipedia*, 2019. https://en.wikipedia.org/wiki/Double_layer_(surface_science) (accessed Mar. 12, 2021).

[11] D. Henderson, "Recent progress in the theory of the electric double layer," *Prog. Surf. Sci.*, vol. 13, no. 3, pp. 197–224, 1983, doi: 10.1016/0079-6816(83)90004-7.

[12] Y. Chen, “Polymer-based Dry Electrodes for Biopotential Measurements,” 2016. [Online]. Available: https://lirias.kuleuven.be/1733146?limo=0

[13] M. R. Neuman, “The Biomedical Engineering Handbook: Second Edition.,” 1999. doi: 10.1201/9781420049510.sec5.

[14] S. M. Lobodzinski, “ECG Instrumentation: Application and Design,” in *Macfarlane, P.W., van Oosterom, A., Pahlm, O., Kligfield, P., Janse, M., Camm, J. (eds) Comprehensive Electrocardiology*, Springer, London, 2010, pp. 427–480. doi: 10.1007/978-1-84882-046-3_12.

[15] S. I. Bîrlea, P. P. Breen, G. J. Corley, N. M. Bîrlea, F. Quondamatteo, and G. Ólaighin, “Changes in the electrical properties of the electrode-skin-underlying tissue composite during a week-long programme of neuromuscular electrical stimulation,” *Physiol. Meas.*, vol. 35, no. 2, pp. 231–252, 2014, doi: 10.1088/0967-3334/35/2/231.

[16] F. Lu *et al.*, “Review of stratum corneum impedance measurement in non-invasive penetration application,” *Biosensors*, vol. 8, no. 2, 2018, doi: 10.3390/bios8020031.

[17] E. Huigen, A. Peper, and C. A. Grimbergen, “Investigation into the origin of the noise of surface electrodes,” *Med. Biol. Eng. Comput.*, vol. 40, no. 3, pp. 332–338, 2002, doi: 10.1007/BF02344216.

[18] K. Goyal, D. A. Borkholder, and S. W. Day, “Dependence of Skin-Electrode Contact Impedance on Material and Skin Hydration,” *Sensors*, vol. 22, no. 8510, 2022, doi: 10.3390/s22218510.

[19] L. A. G. and L. E. Baker, *Principles of applied biomedical instrumentation*. New York: Wiley, 1975. doi: 10.1213/00000539-199005000-00027.

[20] N. Meziane, S. Yang, M. Shokoueinejad, J. G. Webster, M. Attari, and H. Eren, “Simultaneous comparison of 1 gel with 4 dry electrode types for electrocardiography,” *Physiol. Meas.*, vol. 36, no. 3, pp. 513–529, 2015, doi: 10.1088/0967-3334/36/3/513.

[21] G. E. Bergey, R. D. Squires, and W. C. Sipple, “Electrocardiogram Recording with Pasteless Electrodes,” *IEEE Trans. Biomed. Eng.*, vol. BME-18, no. 3, pp. 206–211, 1971, doi: 10.1109/TBME.1971.4502833.

[22] K. Goyal, D. A. Borkholder, and S. W. Day, “Unobtrusive In-Home Respiration Monitoring Using a Toilet Seat,” pp. 01–05, 2022, doi: 10.1109/bhi56158.2022.9926931.

[23] A. Gruetzmann, S. Hansen, and J. Müller, “Novel dry electrodes for ECG monitoring,” *Physiol. Meas.*, vol. 28, no. 11, pp. 1375–1390, 2007, doi: 10.1088/0967-3334/28/11/005.

[24] L. Beckmann *et al.*, “Characterization of textile electrodes and conductors using standardized measurement setups,” *Physiol. Meas.*, vol. 31, no. 2, pp. 233–247, 2010, doi: 10.1088/0967-3334/31/2/009.

[25] A. Cömert, M. Honkala, and J. Hyttinen, “Effect of pressure and padding on motion artifact of textile electrodes,” *Biomed. Eng. Online*, vol. 12, no. 1, pp. 1–18, 2013, doi: 10.1186/1475-925X-12-26.

[26] G. Acar, O. Ozturk, A. J. Golparvar, T. A. Elboshra, K. Böhringer, and M. Kaya Yapici, “Wearable and flexible textile electrodes for biopotential signal monitoring: A review,” *Electron.*, vol. 8, no. 5, pp. 1–25, 2019, doi: 10.3390/electronics8050479.

[27] M. K. Yapici and T. E. Alkhidir, “Intelligent medical garments with graphene-functionalized smart-cloth ECG sensors,” *Sensors*, vol. 17, no. 4, pp. 1–12, 2017, doi: 10.3390/s17040875.

[28] A. A. Chlaihawi, B. B. Narakathu, S. Emamian, B. J. Bazuin, and M. Z. Atashbar, “Development of printed and flexible dry ECG electrodes,” *Sens. Bio-Sensing Res.*, vol. 20, pp. 9–15, 2018, doi: 10.1016/j.sbsr.2018.05.001.

[29] P. Leleux *et al.*, “Conducting Polymer Electrodes for Electroencephalography,” *Adv. Healthc. Mater.*, vol. 3, no. 4, pp. 490–493, 2014, doi: 10.1002/adhm.201300311.

[30] A. Albulbul, “Evaluating major electrode types for idle biological signal measurements for modern medical technology,” *Bioengineering*, vol. 3, no. 3, 2016, doi: 10.3390/bioengineering3030020.

[31] J. S. Lee, J. Heo, W. K. Lee, Y. G. Lim, Y. H. Kim, and K. S. Park, “Flexible capacitive electrodes for minimizing motion artifacts in ambulatory electrocardiograms,” *Sensors*, vol. 14, no. 8, pp. 14732–14743, 2014, doi: 10.3390/s140814732.

[32] T. W. Wang, H. Zhang, and S. F. Lin, “Influence of Capacitive Coupling on High-Fidelity Non-Contact ECG Measurement,” *IEEE Sens. J.*, vol. 20, no. 16, pp. 9265–9273, 2020, doi: 10.1109/JSEN.2020.2986723.

[33] T. Terada, M. Toyoura, T. Sato, and X. Mao, “Noise-reducing fabric electrode for ecg measurement,” *Sensors*, vol. 21, no. 13, pp. 1–17, 2021, doi: 10.3390/s21134305.

[34] C. C. Chen, S. Y. Lin, and W. Y. Chang, “Novel stable capacitive electrocardiogram measurement system,” *Sensors*, vol. 21, no. 11, 2021, doi: 10.3390/s21113668.

[35] Y. G. Lim, K. K. Kim, and K. S. Park, “ECG measurement on a chair without conductive contact,” *IEEE Trans. Biomed. Eng.*, vol. 53, no. 5, pp. 956–959, 2006, doi: 10.1109/TBME.2006.872823.

[36] G. Li, S. Wang, and Y. Y. Duan, “Towards gel-free electrodes: A systematic study of electrode-skin impedance,” *Sensors Actuators B Chem.*, vol. 241, pp. 1244–1255, 2017, doi: 10.1016/j.snb.2016.10.005.

[37] A. S. Anusha, S. P. Preejith, T. J. Akl, J. Joseph, and M. Sivaprakasam, “Dry Electrode Optimization for Wrist-based Electrodermal Activity Monitoring,” *MeMeA 2018 - 2018 IEEE Int. Symp. Med. Meas. Appl. Proc.*, pp. 1–6, 2018, doi: 10.1109/MeMeA.2018.8438595.

[38] R. Kusche, S. Kaufmann, and M. Ryschka, “Dry electrodes for bioimpedance measurements - Design, characterization and comparison,” *Biomed. Phys. Eng. Express*, vol. 5, no. 1, 2019, doi: 10.1088/2057-1976/aaea59.

[39] S. Peng, K. Xu, and W. Chen, “Comparison of active electrode materials for non-contact ECG measurement,” *Sensors*, vol. 19, no. 16, pp. 1–18, 2019, doi: 10.3390/s19163585.

[40] G. Li, S. Wang, and Y. Y. Duan, “Towards conductive-gel-free electrodes: Understanding the wet electrode, semi-dry electrode and dry electrode-skin interface impedance using electrochemical impedance spectroscopy fitting,” *Sensors Actuators B Chem.*, vol. 277, pp. 250–260, 2018, doi: 10.1016/j.snb.2018.08.155.

[41] S. Björklund *et al.*, “Skin membrane electrical impedance properties under the influence of a varying water gradient,” *Biophys. J.*, vol. 104, no. 12, pp. 2639–2650, 2013, doi: 10.1016/j.bpj.2013.05.008.

[42] B. Hirschorn, M. E. Orazem, B. Tribollet, V. Vivier, I. Frateur, and M. Musiani, “Determination of effective capacitance and film thickness from constant-phase-element parameters,” *Electrochim. Acta*, vol. 55, no. 21, pp. 6218–6227, 2010, doi: 10.1016/j.electacta.2009.10.065.

[43] B. Taji, A. D. C. Chan, and S. Shirmohammadi, “Effect of Pressure on Skin-Electrode Impedance in Wearable Biomedical Measurement Devices,” *IEEE Trans. Instrum. Meas.*, vol. 67, no. 8, pp. 1900–1912, 2018, doi: 10.1109/TIM.2018.2806950.

[44] T. Yamamoto and Y. Yamamoto, “Electrical properties of the epidermal stratum corneum,” *Med. Biol. Eng.*, vol. 14, no. 2, pp. 151–158, 1976, doi: 10.1007/BF02478741.

[45] A. K. Dabrowska *et al.*, “Materials used to simulate physical properties of human skin,” *Ski. Res. Technol.*, vol. 22, no. 1, pp. 3–14, 2016, doi: 10.1111/srt.12235.

[46] S. Yao *et al.*, “A Wearable Hydration Sensor with Conformal Nanowire Electrodes,” *Adv. Healthc. Mater.*, vol. 6, no. 6, pp. 1–8, 2017, doi: 10.1002/adhm.201601159.

[47] K. Ito, K. Furuya, Y. Okano, and L. Hamada, “Development and characteristics of a biological tissue-equivalent phantom for microwaves,” *Electron. Commun. Japan, Part I Commun.*, vol. 84, no. 4, pp. 67–77, 2001, doi: 10.1002/1520-6424(200104)84:4<67::AID-ECJA8>3.0.CO;2-D.

[48] T. Yamamoto *et al.*, “Development of electromagnetic phantom at low-frequency band,” *Proc. Annu. Int. Conf. IEEE Eng. Med. Biol. Soc. EMBS*, pp. 1887–1890, 2013, doi: 10.1109/EMBC.2013.6609893.

[49] A. Kalra, A. Lowe, and G. Anand, “Bio Phantoms Mimicking the Dielectric and Mechanical Properties of Human Skin Tissue at Low-Frequency Ranges,” *Mod. Appl. Sci.*, vol. 14, no. 7, p. 1, 2020, doi: 10.5539/mas.v14n7p1.

[50] A. Y. Owda and A. J. Casson, “Investigating Gelatine Based Head Phantoms for Electroencephalography Compared to Electrical and Ex Vivo Porcine Skin Models,” *IEEE Access*, vol. 9, pp. 96722–96738, 2021, doi: 10.1109/ACCESS.2021.3095220.

[51] U. Birgersson, E. Birgersson, P. Åberg, I. Nicander, and S. Ollmar, “Non-invasive bioimpedance of intact skin: Mathematical modeling and experiments,” *Physiol. Meas.*, vol. 32, no. 1, pp. 1–18, 2011, doi: 10.1088/0967-3334/32/1/001.

[52] M. Nachman and S. E. Franklin, “Artificial Skin Model simulating dry and moist in vivo human skin friction and deformation behaviour,” *Tribol. Int.*, vol. 97, pp. 431–439, 2016, doi: 10.1016/j.triboint.2016.01.043.

[53] C. H. Liu *et al.*, “Microelectromechanical system-based biocompatible artificial skin phantoms,” *Micro Nano Lett.*, vol. 14, no. 3, pp. 333–338, 2019, doi: 10.1049/mnl.2018.5112.

[54] K. Goyal, D. A. Borkholder, and S. W. Day, “A biomimetic skin phantom for characterizing wearable electrodes in the low-frequency regime,” *Sensors Actuators A Phys.*, vol. 340, no. 113513, 2022, doi: 10.1016/j.sna.2022.113513.

[55] M. A. Serhani, H. T. El Kassabi, H. Ismail, and A. N. Navaz, “ECG monitoring systems: Review, architecture, processes, and key challenges,” *Sensors*, vol. 20, no. 6, 2020, doi: 10.3390/s20061796.

[56] Y. Fu, J. Zhao, Y. Dong, and X. Wang, “Dry electrodes for human bioelectrical signal monitoring,” *Sensors*, vol. 20, no. 13, pp. 1–30, 2020, doi: 10.3390/s20133651.

[57] X. Niu, X. Gao, Y. Liu, and H. Liu, “Surface bioelectric dry Electrodes: A review,” *Measurement*, vol. 183, no. March, p. 109774, 2021, doi: 10.1016/j.measurement.2021.109774.

[58] H. Kim, E. Kim, C. Choi, and W. H. Yeo, “Advances in Soft and Dry Electrodes for Wearable Health Monitoring Devices,” *Micromachines*, vol. 13, no. 4, 2022, doi: 10.3390/mi13040629.

Chapter 3: A biomimetic skin phantom for characterizing wearable electrodes

Published as **K. Goyal**, D. A. Borkholder, and S. W. Day, “A biomimetic skin phantom for characterizing wearable electrodes in the low-frequency regime,” *Sensors Actuators A Phys.*, vol. 340, no. 113513, 2022, doi: 10.1016/j.sna.2022.113513.

3.1 Abstract

Advances in the integration of wearable devices in our daily life have led to the development of new electrode designs for biopotential monitoring. Historically, the development and testing of wearable electrodes for the acquisition of biopotential signals has been empirical, relying on experiments on human volunteers. However, the lack of explicit control on human variables, the intra-, and inter-subject variability complicates the understanding of the performance of these wearable electrodes. Herein, phantom mimicking the electrical properties of the skin in the low-frequency range (1 Hz-1000 Hz), which has the potential to be used as a platform for controlled benchtop experiments for testing electrode functionality, is demonstrated. The fabricated phantom comprises two layers representing the deeper tissues and stratum corneum. The lower layer of the phantom mimicking deeper tissues was realized using polyvinyl alcohol cryogel (PVA-c) prepared with 0.9% W/W saline solution by a freeze-thaw technique. The properties of the upper layer representing the stratum corneum were simulated using a 100 µm thick layer fabricated by spin-coating a mixture of polydimethylsiloxane (PDMS), 2.5% W/W carbon black (CB) for conductance, and 40% W/W barium titanate ($BaTiO_3$) as a dielectric. The hydration of the stratum corneum was modeled in a controlled way by varying porosity of the phantom's upper layer. Impedance spectroscopy measurements were carried out to investigate the electrical performance of the fabricated phantom and validated against the impedance response obtained across a physiological skin impedance range of five human subjects. The results indicated that the Bode plot depicting the impedance response obtained on the phantom was found to lie in the human skin range. Moreover, it was observed that the change of porosity provides control over the hydration and the phantom can be tuned as per the skin ranges among different individuals. Also, the phantom was able to mimic the impact of dry and hydrated skin on a simulated ECG signal in the time domain. The developed skin phantom is affordable, fairly easy to manufacture, stable over time, and can be used as a platform for benchtop testing of new electrode designs.

Keywords: Biopotential signal; Skin phantom; Impedance spectroscopy; Skin hydration; Wearable electrodes

3.2 Introduction

Biopotential signals such as Electrocardiogram (ECG), Electromyogram (EMG), and Electroencephalogram (EEG) provide vital information about health [1]. The use of health-monitoring systems incorporating wearable electrodes has led to the development of new electrode designs, including materials [2], geometry [3],[4] and surface coatings [5], for biopotential monitoring from the skin surface [6], [7]. However, there is no robust platform to test the performance and functionality of these new electrode designs. Development and testing is typically performed empirically with experiments on human volunteers [8], [9], [10]. The properties of the human skin are variable [11]. First, properties and impedance change over time, making it challenging to perform reproducible measurements. Secondly, the properties of human skin differ for each person. A readily manufacturable skin phantom with explicit controlled properties that is stable in time will provide a benchtop platform to aid research and development of skin contact electrodes designed for acquiring biopotential signals.

The tissue anatomy is considered as a stack of layers (muscle, fat, skin) and these layers have different electrical properties that affect the propagation of potential [12]. Skin is further comprised of different layers, broadly divided into the epidermis, dermis, and subcutaneous layers. The epidermis further consists of four or five layers; the topmost layer being the stratum corneum [13]. Each tissue layer has distinct electrical properties, including electrical impedance [14], which is frequency dependent [15]. The combined skin impedance is of the order of 100Ω at high frequencies and is 10 kΩ-1MΩ at low (<1 kHz) frequencies [16]. The increased impedance at lower frequency is thought to be dominated by the stratum corneum [16], which has high electrical resistance as it consists of dead cells [17]–[19]. The electrical properties of stratum corneum, and subsequently human skin, strongly depend on hydration. Hydration plays an important role in lowering the stratum corneum impedance [20], with hydrated skin, the resistance becomes 14 times lower and capacitance is 1.5 times higher than dry skin conditions [21].

One widely used approach for fabricating phantom uses agar, polyethylene powder, sodium chloride, and TX-151 to simulate electrical characteristics of a highly hydrous biological tissue such as muscle in the high-frequency range of 300 MHz-2.5 GHz [22]. Yamamoto et al. extended this agar approach to mimic the electrical properties (conductivity and relative permittivity) of muscle at 1 MHz [23]. Beckmann et al. made a skin dummy using agar and saline water for testing biopotential electrodes and simulated the conductance of wet skin tissue in the frequency range of 5 kHz-1 MHz [11]. However, this agar approach is limited to simulating high water content tissues and is unable to mimic skin. Existing phantoms are not able to simulate the impedance of dry and hydrated skin conditions necessary for testing dry wearable electrodes for two reasons. First, biopotentials signals (ECG, EEG, EMG) lie in the low-frequency range (0.1 Hz-1000 Hz). Agar-based methods have only been shown effective at modeling impedance in a much higher frequency range, primarily because they do not include a model of the stratum corneum. There is limited work on the phantoms mimicking electrical properties of the skin in the low-frequency range and has significant gaps. Recently, Kalra et al. developed a skin phantom using oil in gelatin to mimic conductivity and permittivity of the skin in the range of 20 Hz-300 kHz, but the results indicated that the permittivity is off by four orders of magnitude with respect to the reference skin data [24]. Owda and Casson improved this by using different gelatin and NaCl concentrations and the contact impedance profile for the phantom was compared with the impedance profile obtained on ex vivo porcine skin over 20 Hz-1000 Hz [25]. However, the impedance of porcine skin is very low in comparison to human skin [26]. Most recently, a two-layered phantom was developed incorporating the effect of the skin layer and was shown to mimic electrical properties in the range 20 Hz-1 MHz [27], which is still too high a frequency range to characterize wearable electrodes. Additionally, this recent phantom is complex to fabricate and the skin hydration state cannot be modeled.

Prior efforts to change hydration of artificial skin phantoms include placing the phantom in a humidity chamber [28] or leaving it out for drying [29], immersing it in water [30], and covering the phantom with a wet cloth soaked in saline solution to mimic hydrated skin [31]. All the aforementioned methods lack explicit control and none have demonstrated the ability to mimic the effect of skin hydration on overall tissue impedance. The goal of this work is to develop the phantom that is substantially similar in impedance to the skin across 1 Hz-1000 Hz, crucial for capturing biopotential signals and mimics the effect of skin hydration in a controlled predictive manner. Here we present a two-layered phantom mimicking electrical properties of deeper tissues and stratum corneum in the frequency range of 1 Hz-1000 Hz. The electrical properties of the deeper tissues have been simulated with polyvinyl alcohol cryogel (15% W/W) prepared with 0.9% W/W saline solution and that of the stratum corneum with a 100µm layer of a PDMS/CB/$BaTiO_3$ mixture. Stratum corneum can be modeled electrically by a parallel combination of equivalent capacitor and resistor configuration, here the hydration of the stratum corneum is modeled using a novel approach that integrates fabricated holes on the stratum corneum layer. These holes become filled with saline from the PVA layers, thus affecting resistance. A phantom that can model the hydration in a controlled and consistent way will facilitate in understanding of the role of skin conditions on the electrode performance and benefit electrode testing and development. Further, we demonstrate that known electrophysiological signals can be provided as an input to the phantom, which is not possible for *in vivo* human skin.

We present here methods for fabrication of the two-layered phantom, followed by experimental techniques used to characterize and evaluate the electrical performance of the phantom with dry electrodes. Conventionally, wet electrodes are the gold standard as they consistently provide clinically acceptable signal quality. However, they are uncomfortable, single use, require skin preparation, and cause skin irritation. Moreover, with recent advancements in remote monitoring technology, wet electrodes are not promising for long-term monitoring due to the gel drying out over time. To overcome the challenges of the wet electrodes, a lot of progress is being made in the field of dry electrodes (contact/non-contact electrodes), as they are comfortable, reusable, require no skin preparation, and generally do not cause skin irritation, albeit with compromised signal quality as compared to wet electrodes. Our phantom is designed to mimic the impedance of the stratum corneum as well as the skin-electrode interface impedance for any dry electrode, and we chose to use stainless steel dry electrodes for evaluating the electrical performance of the fabricated phantom. Currently, dry metal-based stainless steel electrodes are integrated into various in-home monitoring devices such as Kardia Mobile (Alivecor Inc., San Francisco, CA, USA), which is a handheld monitor to capture ECG, and a toilet seat to capture buttocks ECG (bECG) (Conn et al., 2018). As validation, the impedance results obtained from the interaction of the phantom with dry electrodes are compared to that of human skin. Further, we evaluate the time stability and reproducibility of the phantom. Lastly, we demonstrate an active phantom in the time domain using a 0.12 mV (typical bECG amplitude) signal, which is an order of magnitude lower than typical ECG amplitude (1.6 mV). The choice of bECG was made because the combination of dry electrodes and fairly weak ECG signal in the buttocks make the sensing of a high-quality ECG a challenging application representative of applications where a phantom may facilitate electrode design.

3.3 Materials and Methods

3.3.1 Phantom Fabrication

3.3.1.1 Materials:

PDMS (Sylgard 184 silicone elastomer; Electron Microscopy Sciences, Hatfield, PA, USA) was used as bulk materials, but has a high volume resistivity of the order 2.9×10^{14} ohm·cm, a dielectric constant of 2.72 @100 Hz and 2.68 @100 kHz [32], which makes it non-conductive. Conductance was increased by adding carbon black powder (CB; Vulcan XC-72R, Fuel Cell Store, College Station, TX, USA) and dielectric properties were increased by adding barium titanate powder ($BaTiO_3$; Sigma Aldrich, St. Louis, MO, US, product number 208108, mean particle diameter <3µm) [33]. Preliminary analysis and experiments showed that a composite of PDMS doped with 2.5% W/W carbon black and 40% W/W barium titanate resulted in the desired resistance and capacitance of 1MΩ and 10 nF [34] for the stratum corneum. PVA (Elvanol 71-30, Chemical Store Inc, Clifton, NJ, USA), a synthetic polymer and soluble in hot water was used to develop the lower layer of the phantom representing deeper tissues, which are hydrous and conductive [16]. Moreover, the dielectric properties of PVA cryogels can be tuned by freeze-thaw cycling [35].

3.3.1.2 Fabrication process:

The fabrication process of a two-layered phantom is schematically illustrated in Figure 3.1. To fabricate the upper layer of the phantom, 6g of sylgard 184 silicone elastomer was mixed in the ratio of 10:1.5 to obtain PDMS with increased crosslinking, to facilitate mechanical strength and easy handling of the 100 µm stratum corneum layer [36]. We then added 40% W/W $BaTiO_3$ and mixed using a stirrer for 10 minutes, followed by 2.5% W/W carbon black powder and 20 minutes mixing. The container was placed in a vacuum chamber for 30 minutes to remove air bubbles. The mixture was spin-coated using a spin coater (Model WS-400-6NPP-LITE, Laurel Technologies Corp., North Wales, PA, USA) onto an acrylic wafer (14 cm diameter, 3/32” thick), at a speed of 1000 rpm for 30 seconds to obtain a thickness of 100µm [37]. The spin-coated wafer was placed in an oven (Heratherm OGS 100 Thermo Electron LED, GmbH, Thermo Scientific, Waltham, MA, USA) for curing at 80°C for two hours. After curing, a laser cutter (H-Series, 20" x 12" Desktop CO2 laser, Full Spectrum Laser, Las Vegas, NV, USA) was used at a speed of 100, a power of 1, and with 1 pass to cut 0.1 mm-diameter holes and a 10 x 4 cm rectangular piece from the wafer's center. A mold (of dimension L x W x H = 10 cm x 4 cm x 0.5 cm) was 3D printed using SLA 3D-printing (Form 2, Formlabs Inc., Somerville, MA, USA). The layer representing the stratum corneum was peeled from the acrylic wafer and placed on the bottom of the mold.

For fabricating the deep tissue layers of the phantom, PVA cryogel was developed using a 0.9% W/W saline solution and polymerized by a freeze-thaw technique without any chemical crosslinkers [38]. To prepare the PVA-c solution, 8.8 g of PVA powder was mixed slowly with continuous stirring in 50 ml of 0.9% W/W saline solution (0.9 g of NaCl in 99.1 g of DI water). The solution was microwaved to a boil and stirred. The process of heating was repeated until translucent. The beaker was covered with a parafilm and left to cool to room temperature (RT). Air bubbles at the top of the solution were scraped and discarded. The PVA-c solution was poured on top of the stratum corneum layer in the mold. The mold was subjected to a single freeze (12 hours at -20°C) /thaw (24 hours at room temperature) cycle to cross-link the PVA-c polymer and polymerize the gel [39]. For thawing, the entire assembly along with mold was stored in a ziplock bag within an environmental chamber (Model 5503, Temperature and Humidity Chamber, Microcontroller 5200, Electro-Tech Systems, Perkasie, PA, USA) at RH of 90% and RT of 22 °C. The ziplock bag was used to prevent the PVA cryogel from drying and losing water. Further, the longer thawing cycle and storage in the humidity chamber facilitated the phantom reach an equilibrium stage.

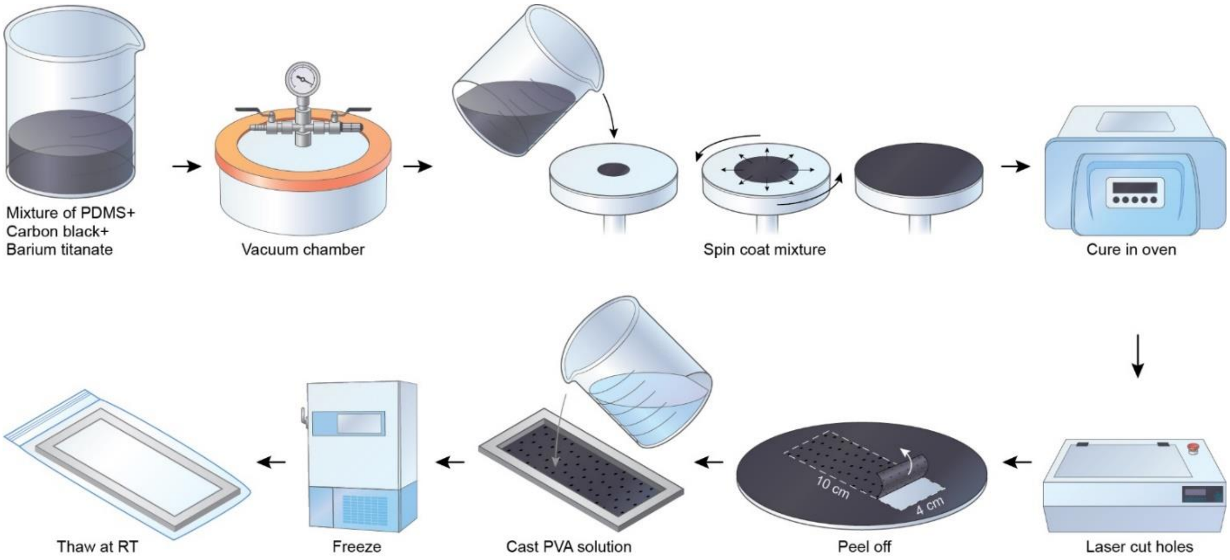

Figure 3.1. Steps for the fabrication process of a two-layered phantom. Clockwise from top-left: a mixture of PDMS, Carbon black, barium titanate; followed by removal of air bubbles in the vacuum chamber; Spin coat mixture at 1000 rpm and 30 seconds; Cure in an oven at 80°C for two hours; Laser-cut holes; Peel off the layer; Cast PVA solution; Freeze (12 hours at -20°C); Thaw (24 hours at RT).

3.3.1.3 Hydration control via porosity:

Different hydration states of the stratum corneum were modeled in a controlled way on the surface of the phantom by varying porosity. Porosity is defined as a measure of empty spaces in a material. Mathematically, it can be described as the fraction of void space in material over the total volume. Here, the porosity represents the percentage of open area and was calculated by the area fraction as both void and bulk material have the same thickness (eq. 1).

$$\emptyset = \frac{\text{no.of pores}^{*}\, A_{\text{pore}}}{A_{\text{bulk material}}} \qquad \text{(eq. 1)}$$

Where, A_pore is the area of the pore, A_(bulk material) is the area of bulk material (SC layer) and $\emptyset$ represents porosity. It was achieved by cutting out holes from the fabricated upper layer representing stratum corneum with the laser cutter. Different sets of phantom were made and different hydration states were modeled with varying porosity of 0%, 0.16%, 0.28%, and 1.4%. The impedance response across different sets of phantoms was obtained to understand the effect of porosity.

The thickness and uniformity of the fabricated layer were measured using an optical non-contact profilometer (ST400, Nanovea Inc, Irvine, CA, USA). Further, the hole size characterization was performed and the microscopic images were captured using a digital microscope (KH-7700, Hirox-USA, Inc., NJ, USA). The dimensions of the hole were measured along the x-axis and y-axis, and the mean was computed. 10 random holes were selected across the entire phantom and the mean and standard deviation (SD) were obtained. The obtained value of mean was used as the radius of the fabricated hole and A_pore was computed, and was also plugged into equation 1 to calculate the porosity.

3.3.2 Impedance Spectroscopy Measurements

Impedance spectroscopy measurements were performed with a potentiostat (Reference 600, Gamry Instruments Inc., Warminster, PA, USA) in a two-electrode configuration using two stainless steel dry electrodes, each of area 9 cm^2 (Figure 3.2). The potentiostat consists of four probes, namely working (W), counter (C), working sense (WS), and reference (R). The working and counter probe carries the current and the working sense and reference measures the voltage. W and WS were connected to one electrode and C and

R were connected to the second electrode. A 25 mV RMS AC voltage signal was generated using a potentiostat over a frequency sweep from 1 Hz-1000 Hz. Bode plot analysis was performed to characterize impedance with respect to frequency.

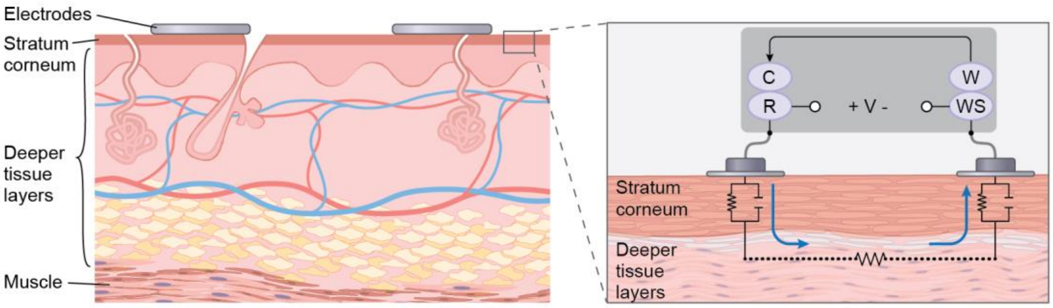

Figure 3.2. Skin cross-section where stratum corneum represents the outermost layer of the skin and the deeper tissue layers together represent the other layers of the epidermis, dermis, and hypodermis. The zoomed-in view of the skin cross-section showing an electrical equivalent model of the electrode-skin interface and the two-electrode configuration set up where C, R, W, and WS represent counter, reference, working, and working sense electrodes, respectively.

To validate the performance of the developed phantom with the impedance response of human skin, impedance spectroscopy experiments were carried out on the human volar arm for five adult volunteers (four male and one female) belonging to different ethnic groups. Two stainless steel dry electrodes were placed 4 inches apart on the subject’s left volar forearm. Metal snap connectors had previously been integrated into the electrodes and were used to connect the probes of the potentiostat. Medical tape (3M Kind Removal Silicone Tape) was used to attach the electrodes to the arm. A 25 mV RMS AC voltage signal within the current range of 600 nA-600 µA was generated using a potentiostat (Reference 600, Gamry Instruments Inc., Warminster, PA, USA) over a frequency sweep from 1 Hz-1000 Hz, and the data was recorded. The potentiostat was plugged into a medical-grade isolation transformer (ILC-1400MED4, TSI Power Corp., Antigo, WI, USA) to ensure electrical safety.

Experiments were conducted under an informed consent, in a protocol approved by the Rochester Institute of Technology Institutional Review Board for Protection of Human Subjects. The first experiment ("Dry") was performed with dry electrodes on the untreated skin. Prior to the second (Hydrated) experiment, the subject was asked to soak their volar forearm in a tray partially filled with lukewarm (40°C) water for 30 minutes [40], [41]. The arm of the subject was wiped with the paper towel to remove the excess water from the surface of the skin, and the electrodes were applied and impedance measurements made. The physiological range of skin impedance for untreated and hydrated skin obtained across five subjects was compared to the impedance response on the phantom. To study how accurately the signals are being transmitted through the phantom, group delay values were calculated using the method as in [25] and compared to the group delay values obtained corresponding to the human skin data.

3.3.3 Stability and Reproducibility of phantom

To investigate the stability of the phantom over time, and the use of the phantom for multiple days, impedance measurements were carried out several times of the day over consecutive days. The phantom was stored in the environmental chamber between experiments. The weight was measured prior to the impedance measurements. After the impedance measurements, the phantom was returned to the ziplock bag in humidity chamber at RH 90% and RT 22 ºC to reduce drying. This experiment was repeated for four days. To evaluate the reproducibility of the fabricated phantom, four different batches of phantom were made. The impedance measurements were performed across 1 Hz-1000 Hz and at each frequency, mean and SD were calculated across four replicates.

3.3.4 Active phantom

To demonstrate the behavior of the phantom in the time domain, a simulated ECG signal was injected into the bottom of the phantom and the output signal was recorded from the top surface of the phantom. An ECG signal of 0.12 mV (typical bECG amplitude) with a sampling frequency of 1000 Hz was simulated using LabVIEW Biomedical Toolkit (Simulate ECG express VI), with analog outputs of a DAQ (USB-6215, National Instruments Corp., Austin, TX, USA) connected to wet electrodes (3M Red Dot 2560, 3M, Maplewood, MN, USA) attached to the bottom of the phantom. Stainless steel dry electrodes of area 1 cm^2 were held in contact with the phantom's surface with the micromanipulator (M325, World Precision Instruments, Sarasota, FL, USA). This ensured good contact and consistent pressure between the electrode and the phantom. The acquired ECG signal from a set of phantoms with porosity of 0%, 0.16%, 0.28%, and 1.4% was recorded. The raw signal was processed using a third-order Butterworth bandpass filter with a bandwidth of 0.5 Hz-150 Hz, along with a notch filter at 60 Hz to obtain a denoised ECG signal. The noise component was calculated by subtracting the denoised ECG signal from the raw ECG signal. Power spectral densities of denoised signal and noise component were calculated by Welch's method [42]. The power was computed by approximating the area under the power spectral density curves [43]. Signal to noise ratio (SNR) was calculated as the ratio of the power of denoised ECG signal to the power of noise component and represented in decibels.

3.4 Results and Discussion

3.4.1 Fabricated phantom

The completed integrated phantom with a porosity of 1.4% is shown in Figure 3.3. The phantom is 0.5 cm thick and 10 cm × 4 cm. The average thickness of the fabricated stratum corneum measured using an optical profilometer was 99 µm, SD 3 µm, across the surface. All measurements fell within a range of 91 to 104 µm. We do not believe that the PVA-c solution filled these pores, due to the small hole diameter and high viscosity of the PVA-c solution. The hole size was examined to understand the kerf of the laser cutter (Figure A1 of Appendix A) and holes drawn with a nominal diameter of 0.1 mm and 0.2 mm resulted in actual hole diameters of 0.31 ± 0.020 (mean ± SD) and 0.40 ± 0.021 (mean ± SD) respectively. Moreover, the examination reveals that we have a small variation in the diameters of the actual holes. Unlike previously reported skin phantom [27], our developed phantom model and holes are not analogous to the physical skin and the sweat pores, but by using the concept of porosity, the phantom has been modeled to simulate the impedance behavior similar to dry and hydrated human skin. The fabrication process is comprised of standard techniques, such as spin coating and laser cutting, that can be found at most universities and are easily learned. The cost of consumables is a few dollars (< $3) for each fabricated phantom. Thus, our developed phantom is easy to manufacture, affordable and incorporates a simple strategy for modeling the skin hydration state.

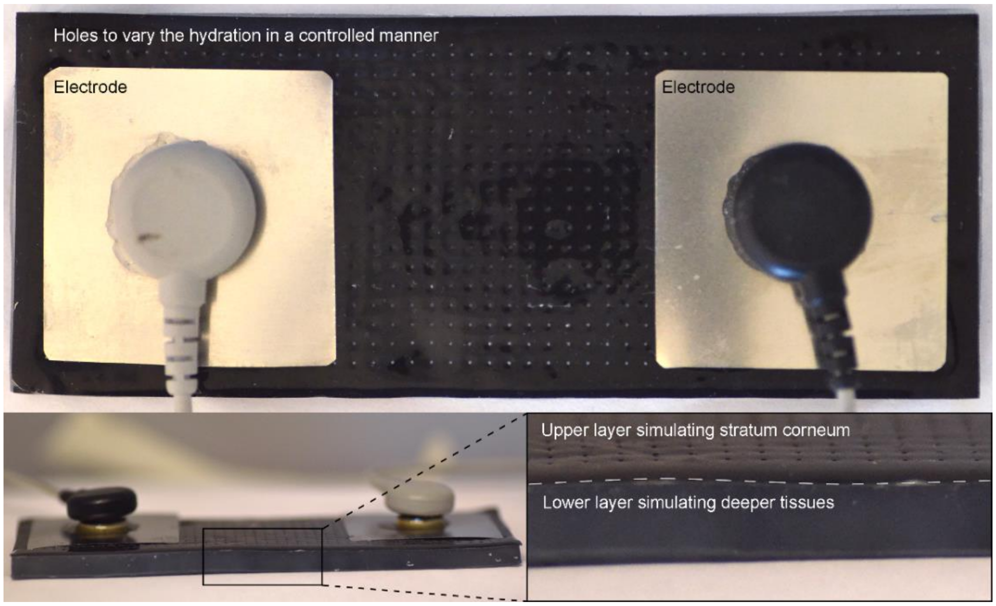

Figure 3.3. Photograph of the fabricated two-layered phantom with 1.4% porosity and 2-electrode configuration. The upper layer of the phantom simulates the stratum corneum and the lower layer simulates deeper tissues.

3.4.2 Electrical performance of the fabricated phantom

The Bode plots depicting the impedance of phantoms shows that the higher porosity phantoms have a lower impedance (Figure 3.4). This is likely because the holes in the stratum corneum layer fill with saline, which is more conductive than the polymer. In comparison to the impedance response of human skin, it was found that the phantoms with porosity of 0.16% and 0.28% lie in the physiological range of untreated skin and hydrated skin respectively, and have a similar slope. The similar slope to that of human skin impedance indicated that the upper layer of the phantom was able to simulate the combination of resistive and capacitive nature, analogous to that of stratum corneum in the actual human skin (Figure 3.4a). Moreover, the phase response for 0.16% and 0.28%

porosity phantoms was within 15 degrees of one another and within 13 degrees for dry and hydrated skin across the range of frequencies tested (Figure 3.4b). The group delay values for 0.16% and 0.28% porosity phantoms are generally <1msec in 10 Hz-1000 Hz (Figure 3.4c), which is small as compared to the duration of the electrophysiological signals and comparable to previously reported group delays for wet electrodes (Owda and Casson, 2021). At lower frequencies (1Hz-10Hz), our group delay values are larger, but are the first reported at low frequency and are lower than our measurements on actual human skin. The effect of this mismatch in phase and group delay is investigated in section 3.4.4, which indicates that there was no signal distortion in the ECG.

In comparison to existing phantoms [11], [24], where the phantoms were fabricated as a single homogeneous layer and did not include the stratum corneum impedance, the skin phantom developed in this work incorporates a model to simulate stratum corneum. The impedance of the phantom with 0.28% porosity was found to be lower by half an order of magnitude compared to the 0.16% porosity phantom. This is similar to the hydrated and dry human skin impedance. This indicated that the developed phantom can mimic the effect of skin hydration on the overall impedance. Several factors in the recipe can be varied for decreasing the impedance of the developed phantom to simulate the impedance of hydrated skin. These factors include thickness of the upper layer, concentration of carbon black powder, barium titanate, saline water, and PVA, as well as the freeze-thaw cycles. Preliminary exploration towards deciding onto porosity as the variable to vary the impedance of the phantom is discussed in Appendix A (Figure A2, Figure A3, Figure A4).In addition, porosity can be tuned to mimic different hydration levels and as per different individual skin impedances. Thus, unlike previously reported phantoms [31], [25]our phantom includes a mechanism for modeling various skin hydration, which is important for developing and characterizing biopotential electrodes for wearable technologies.

Lastly, the phantom effectively mimics impedance across the entire frequency range (1 Hz-1000 Hz) crucial for capturing various biopotential signals such as ECG, and EMG. Previous research indicated that the frequency content of the ECG waves varies. P wave is characterized by 5-30 Hz, T wave content lies below 10 Hz, and the main power lies in QRS complex, reflected by 5-15 Hz [44], [45]. The bandwidth of the EMG signal lies between 20 Hz-1000 Hz [46]. Prior phantoms [24], [25], [27] do not characterize their phantoms in the 1 Hz-20 Hz frequency range. This work is the first comparison of the phantom to *in vivo* human skin impedance across the frequency range (1 Hz-1000 Hz). A previously reported research study [24], compares the performance of the phantom with respect to relative permittivity and conductivity value of dry and wet skin based upon experiments [47], however, the database does not provide the dielectric properties below 10 Hz. In this work, we present a comparison of the phantom to *in vivo* data obtained for dry and hydrated skin across the entire frequency range (1 Hz-1000 Hz).

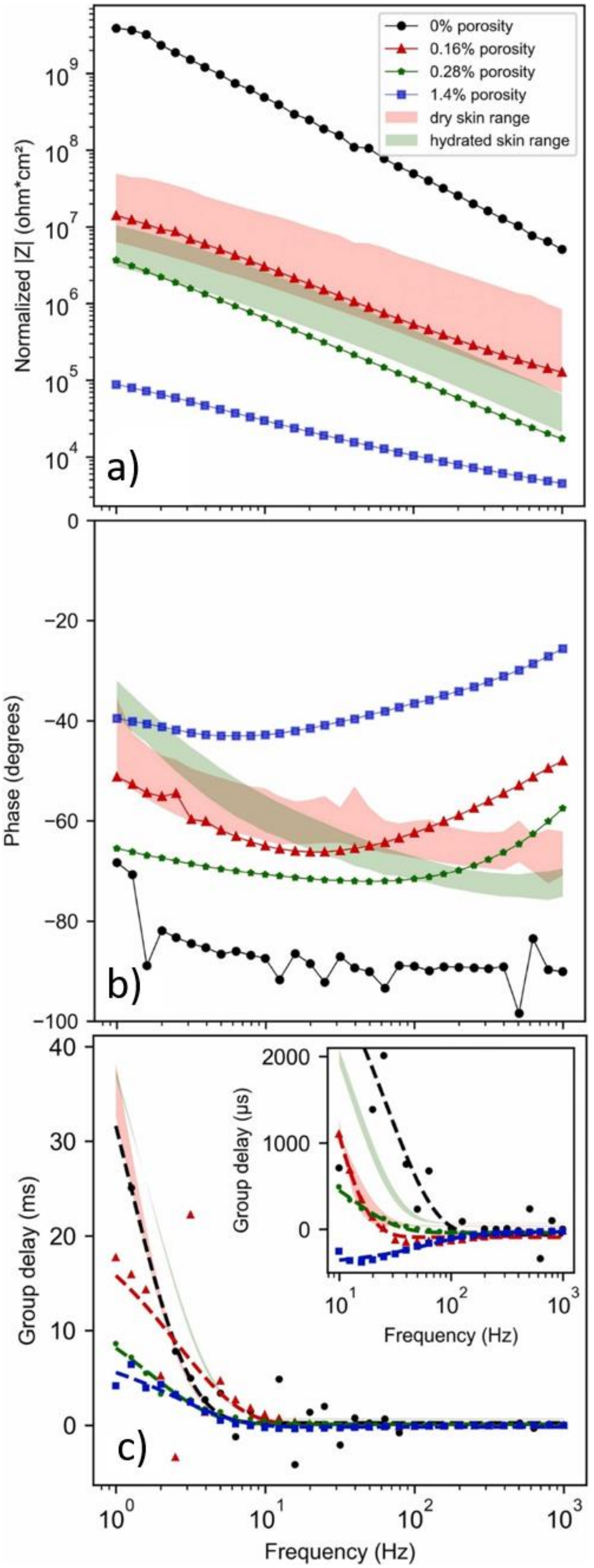
0% porosity
0.16% porosity
0.28% porosity
1.4% porosity
dry skin range
hydrated skin range
Normalized |Z| (ohm*cm²)
10^9
10^8
10^7
10^6
10^5
10^4
a)
Phase (degrees)
0
−20
−40
−60
−80
−100
b)
Group delay (ms)
40
30
20
10
0
c)
Group delay (µs)
2000
1000
0
10^1
10^2
10^3
Frequency (Hz)
10^0
10^1
10^2
10^3
Frequency (Hz)

Figure 3.4. a) Impedance magnitude and b) phase response c) group delay for the phantoms with porosity of 0% (black circle), 0.16 % (red triangle), 0.28% (green star), and 1.4% (blue square). The physiological range of impedance magnitude and phase response obtained on the human arm (five subjects) for untreated and hydrated skin is shown with the red and green background color respectively. Dashed lines in panel c) indicate the curve fit to aid for data visualization. The inset graph shows a zoomed-in view for the group delay corresponding to the frequency range of 10 Hz-1000 Hz.

3.4.3 Stability and Reproducibility of the fabricated phantom

The results of the 4-day experiment to test the stability of the phantom indicated an upward shift in the impedance response over time (Figure 3.5). The weight of the phantom was found to be 24.17 g, 22.50 g, and 22.28 g on Day 1, Day 3, and Day 4 respectively. There was a decline in the weight over time, which indicated that the water loss could be the reason for the observed upward shift in the impedance response of the phantom. This is in complete agreement with the previously reported findings [25] where the impedance response was studied for seven days and found to increase over time. In our work, we not only investigated the stability of the phantom over time for consecutive days but also the impedance measurements were performed several times each day, and it was found that there was no significant shift in the impedance response on the same day of the experiment. This result indicates that the same phantom can be used to perform experiments multiple times on the same day of the experiment. The results of the impedance measurements obtained for four replicates show that across the range of frequency, the SD was about 25% of the mean, shown in the Appendix A (Figure A5). The phantom developed in this work, uses a quick method for the electrical measurements with the impedance measurement technique. This enables the phantom to be used to evaluate the performance of different electrode configurations fairly quickly.

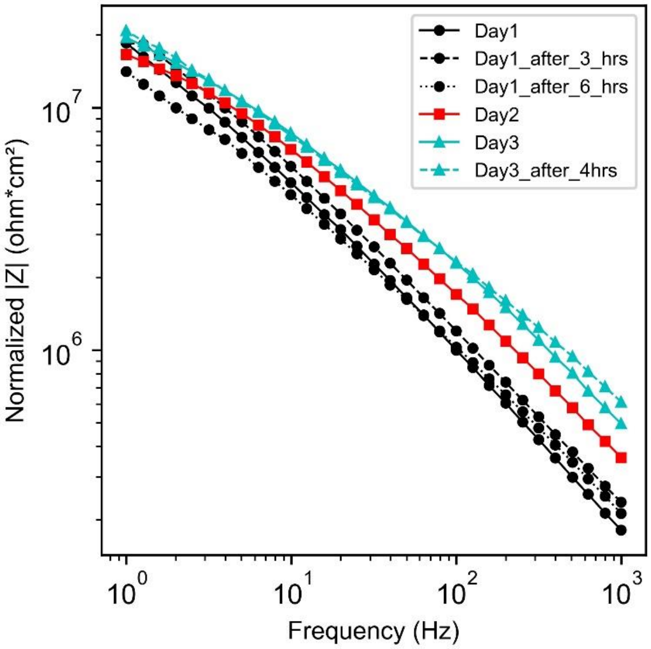

Figure 3.5. Impedance response for phantom with porosity 0.16% obtained on Day 1 (black circle solid line), Day 1 after three hours (black circle dashed line), Day 1 after six hours (black circle dotted line), Day 2 (red square solid line), Day 3 (cyan triangle solid line), and Day 3 after four hours (cyan triangle dashed line).

3.4.4 Active phantom

ECG signal recorded on phantoms with different porosities (0%, 0.16%, 0.28%, and 1.4%) was found to be significantly different both qualitatively and quantitatively (Figure 3.6). For a 0.12 mV ECG, typical for buttocks [48], we saw a low SNR (2.04 dB) for the phantom with porosity 0.16% which simulates the dry skin impedance. Hydrated skin, modeled with the 0.28% porosity, corresponds to lower skin-electrode impedance, thus higher SNR (9.08 dB), which is consistent with prior reported work [49], [50]. This is primarily because more noise gets integrated with higher impedance. The difference between the simulated dry and hydrated skin was only evident with the 0.12 mV amplitude ECG signal. Although not shown here, it was observed that the different phantom configurations all had a much higher SNR with either a bigger area electrode (9 cm^2) or a higher amplitude ECG signal (1.6 mV), typically obtained from standard locations. This is exactly what would be expected as the increase in the electrode area decreases the skin-electrode contact impedance [5]. Hence, the phantom developed in this work can mimic dry and hydrated skin impedance and clearly simulate the impact of dry and hydrated skin conditions on the ECG signal. Therefore, the phantom provides a platform for controlled testing where a known signal can be given and recorded on the surface, which is challenging in the case of human subjects due to the unknown signal and variable skin impedance.

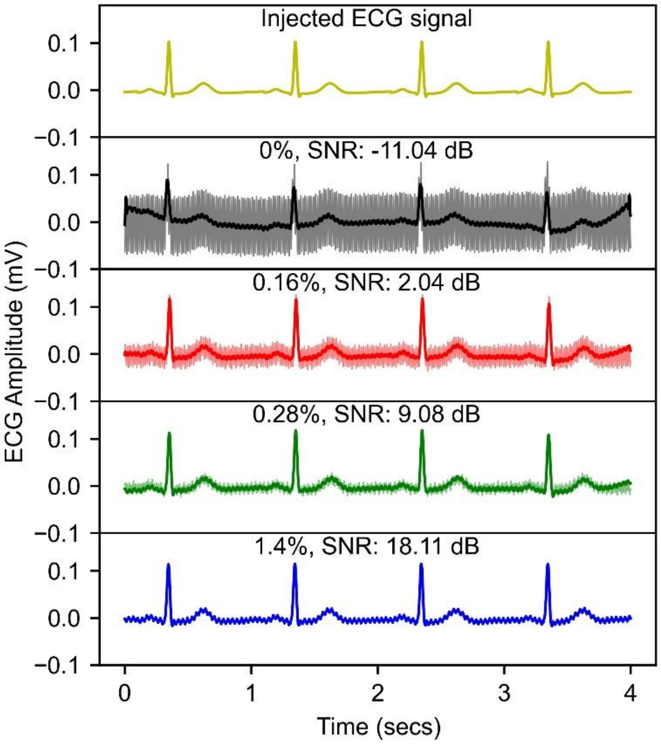

Figure 3.6. ECG recorded from phantoms with different porosities of 0%, 0.16%, 0.28%, and 1.4%. Top to bottom represent injected ECG signal, raw measured ECG superimposed with the denoised signal (bold line) for each phantom respectively. Calculated SNR is shown in text.

3.5 Conclusion

We developed a first of its kind skin phantom to model the interaction with dry electrodes across the range of frequency necessary for biopotential signals such as ECG, EEG, and EMG. Simple techniques were used for fabrication and properties of the phantom are stable for several days. The phantom mimics the effect of skin hydration in a controlled predictive manner based on the novel approach of varying porosity of a layer simulating the stratum corneum, the uppermost layer of skin. The porosity-based approach provides a method that can be leveraged to tune the phantom to simulate different individual skin impedances and study the impact of different skin types on the wearable electrodes. Spectroscopy measurements performed on the fabricated phantom showed that the impedance response for the phantom is similar to that of the human skin range. We additionally showed that the phantom simulated the impact of actual dry and hydrated skin conditions on the ECG signal quality in the time domain. The phantom could be used to facilitate electrode development, greatly reducing cost and complexity and increasing reproducibility by working with phantoms instead of a human subject.

References

[1] Y. Fu, J. Zhao, Y. Dong, and X. Wang, "Dry electrodes for human bioelectrical signal monitoring," Sensors, vol. 20, no. 13, pp. 1–30, 2020, doi: 10.3390/s20133651.

[2] S. Peng, K. Xu, and W. Chen, "Comparison of active electrode materials for non-contact ECG measurement," Sensors, vol. 19, no. 16, pp. 1–18, 2019, doi: 10.3390/s19163585.

[3] S. Kaitainen, A. Kutvonen, M. Suvanto, T. T. Pakkanen, R. Lappalainen, and S. Myllymaa, "Liquid silicone rubber (LSR)-based dry bioelectrodes: The effect of surface micropillar structuring and silver coating on contact impedance," Sensors

Actuators, A Phys., vol. 206, pp. 22–29, 2014, doi: 10.1016/j.sna.2013.11.020.

[4] Y. Maithani, B. Choudhuri, B. R. Mehta, and J. P. Singh, “Self-adhesive, stretchable, and dry silver nanorods embedded polydimethylsiloxane biopotential electrodes for electrocardiography,” Sensors Actuators A Phys., vol. 332, p. 113068, 2021, doi: 10.1016/j.sna.2021.113068.

[5] A. A. Chlaihawi, B. B. Narakathu, S. Emamian, B. J. Bazuin, and M. Z. Atashbar, “Development of printed and flexible dry ECG electrodes,” Sens. Bio-Sensing Res., vol. 20, pp. 9–15, 2018, doi: 10.1016/j.sbsr.2018.05.001.

[6] F. Khoshmanesh, P. Thurgood, E. Pirogova, S. Nahavandi, and S. Baratchi, “Wearable sensors: At the frontier of personalised health monitoring, smart prosthetics and assistive technologies,” Biosens. Bioelectron., vol. 176, no. October 2020, p. 112946, 2021, doi: 10.1016/j.bios.2020.112946.

[7] G. Acar, O. Ozturk, A. J. Golparvar, T. A. Elboshra, K. Böhringer, and M. Kaya Yapici, “Wearable and flexible textile electrodes for biopotential signal monitoring: A review,” Electron., vol. 8, no. 5, pp. 1–25, 2019, doi: 10.3390/electronics8050479.

[8] A. S. Anusha, S. P. Preejith, T. J. Akl, J. Joseph, and M. Sivaprakasam, “Dry Electrode Optimization for Wrist-based Electrodermal Activity Monitoring,” MeMeA 2018 - 2018 IEEE Int. Symp. Med. Meas. Appl. Proc., pp. 1–6, 2018, doi: 10.1109/MeMeA.2018.8438595.

[9] G. E. Bergey, R. D. Squires, and W. C. Sipple, “Electrocardiogram Recording with Pasteless Electrodes,” IEEE Trans. Biomed. Eng., vol. BME-18, no. 3, pp. 206–211, 1971, doi: 10.1109/TBME.1971.4502833.

[10] P. L. Fink, A. S. Muhammad Sayem, S. H. Teay, F. Ahmad, H. Shahariar, and A. Albarbar, “Development and wearer trial of ECG-garment with textile-based dry electrodes,” Sensors Actuators, A Phys., vol. 328, p. 112784, 2021, doi: 10.1016/j.sna.2021.112784.

[11] L. Beckmann et al., “Characterization of textile electrodes and conductors using standardized measurement setups,” Physiol. Meas., vol. 31, no. 2, pp. 233–247, 2010, doi: 10.1088/0967-3334/31/2/009.

[12] S. Gabriel, R. W. Lau, and C. Gabriel, “The dielectric properties of biological tissues: II. Measurements in the frequency range 10 Hz to 20 GHz,” Phys. Med. Biol., vol. 41, no. 11, pp. 2251–2269, 1996, doi: 10.1088/0031-9155/41/11/002.

[13] J. M. Reicherter, “Anatomy and physiology for polygraph examiners,” in Fundamentals of Polygraph Practice, D. J. Krapohl and P. K. Shaw, Eds. Elsevier Inc., 2015, pp. 29–60. doi: 10.1016/b978-0-12-802924-4.00002-5.

[14] H. Kalvøy, L. Frich, S. Grimnes, Ø. G. Martinsen, P. K. Hol, and A. Stubhaug, “Impedance-based tissue discrimination for needle guidance,” Physiol. Meas., vol. 30, no. 2, pp. 129–140, 2009, doi: 10.1088/0967-3334/30/2/002.

[15] T. K. Bera, “Bioelectrical Impedance and the Frequency Dependent Current Conduction Through Biological Tissues: A Short Review,” IOP Conf. Ser. Mater. Sci. Eng., vol. 331, no. 1, 2018, doi: 10.1088/1757-899X/331/1/012005.

[16] S. I. Bîrlea, P. P. Breen, G. J. Corley, N. M. Bîrlea, F. Quondamatteo, and G. Ólaighin, “Changes in the electrical properties of the electrode-skin-underlying tissue composite during a week-long programme of neuromuscular electrical stimulation,” Physiol. Meas., vol. 35, no. 2, pp. 231–252, 2014, doi: 10.1088/0967-3334/35/2/231.

[17] S. M. Lobodzinski, “ECG Instrumentation: Application and Design,” in Macfarlane, P.W., van Oosterom, A., Pahlm, O., Kligfield, P., Janse, M., Camm, J. (eds) Comprehensive Electrocardiology, Springer, London, 2010, pp. 427–480. doi: 10.1007/978-1-84882-046-3_12.

[18] S. Ha, C. Kim, Y. M. Chi, and G. Cauwenberghs, “Low-Power Integrated Circuit Design for Wearable Biopotential Sensing,” in Wearable Sensors: Fundamentals, Implementation and Applications, E. Sazonov and M. R. Neuman, Eds. Oxford, U.K.:Academic, 2014, pp. 323–352. doi: 10.1016/B978-0-12-418662-0.00018-0.

[19] J. Heikenfeld et al., “Wearable sensors: Modalities, challenges, and prospects,” Lab Chip, vol. 18, no. 2, pp. 217–248, 2018, doi: 10.1039/c7lc00914c.

[20] E. J. Clar, C. P. Her, and C. G. Sturelle, “Skin impedance and moisturization,” J. Soc. Cosmet. Chem. Japan, vol. 26, no. 7, pp. 337–353, 1975.

[21] S. Björklund et al., “Skin membrane electrical impedance properties under the influence of a varying water gradient,” Biophys. J., vol. 104, no. 12, pp. 2639–2650, 2013, doi: 10.1016/j.bpj.2013.05.008.

[22] K. Ito, K. Furuya, Y. Okano, and L. Hamada, “Development and characteristics of a biological tissue-equivalent phantom for microwaves,” Electron. Commun. Japan, Part I Commun., vol. 84, no. 4, pp. 67–77, 2001, doi: 10.1002/1520-6424(200104)84:4<67::AID-ECJA8>3.0.CO;2-D.

[23] T. Yamamoto et al., “Development of electromagnetic phantom at low-frequency band,” Proc. Annu. Int. Conf. IEEE Eng. Med. Biol. Soc. EMBS, pp. 1887–1890, 2013, doi: 10.1109/EMBC.2013.6609893.

[24] A. Kalra, A. Lowe, and G. Anand, “Bio Phantoms Mimicking the Dielectric and Mechanical Properties of Human Skin Tissue at Low-Frequency Ranges,” Mod. Appl. Sci., vol. 14, no. 7, p. 1, 2020, doi: 10.5539/mas.v14n7p1.

[25] A. Y. Owda and A. J. Casson, “Investigating Gelatine Based Head Phantoms for Electroencephalography Compared to Electrical and Ex Vivo Porcine Skin Models,” IEEE Access, vol. 9, pp. 96722–96738, 2021, doi: 10.1109/ACCESS.2021.3095220.

[26] R. Tregear, “Interpretation of Skin Impedance Measurements,” Nature, vol. 205, no. 5007, pp. 600–601, 1965, doi: https://doi.org/10.1038/205600a0.

[27] C. H. Liu et al., “Microelectromechanical system-based biocompatible artificial skin

phantoms," Micro Nano Lett., vol. 14, no. 3, pp. 333–338, 2019, doi: 10.1049/mnl.2018.5112.

[28] S. Yao et al., "A Wearable Hydration Sensor with Conformal Nanowire Electrodes," Adv. Healthc. Mater., vol. 6, no. 6, pp. 1–8, 2017, doi: 10.1002/adhm.201601159.

[29] M. Nachman and S. E. Franklin, "Artificial Skin Model simulating dry and moist in vivo human skin friction and deformation behaviour," Tribol. Int., vol. 97, pp. 431–439, 2016, doi: 10.1016/j.triboint.2016.01.043.

[30] A. Dąbrowska et al., "A water-responsive, gelatine-based human skin model," Tribol. Int., vol. 113, no. January, pp. 316–322, 2017, doi: 10.1016/j.triboint.2017.01.027.

[31] Y. H. Chen et al., "Soft, comfortable polymer dry electrodes for high quality ECG and EEG recording," Sensors (Switzerland), vol. 14, no. 12, pp. 23758–23780, 2014, doi: 10.3390/s141223758.

[32] The Dow Chemical Company, "SYLGARD TM 184 Silicone Elastomer Technical Datasheet," 2017. https://www.dow.com/content/dam/dcc/documents/en-us/productdatasheet/11/11-31/11-3184-sylgard-184-elastomer.pdf?iframe=true-us/productdatasheet/11https://consumer.dow.com/content/dam/dcc/documents/en-us/productdatasheet/11/11-31/11-3184-sylgard-184-elasto (accessed Sep. 07, 2021).

[33] C. Nawanil et al., "Electrical and dielectric properties of barium titanate–polydimethylsiloxane nanocomposite with 0-3 connectivity modified with carbon nanotube (CNT)," Integr. Ferroelectr., vol. 195, no. 1, pp. 46–57, 2019, doi: 10.1080/10584587.2019.1570043.

[34] Y. M. Chi, T. P. Jung, and G. Cauwenberghs, "Dry-contact and noncontact biopotential electrodes: Methodological review," IEEE Rev. Biomed. Eng., vol. 3, pp. 106–119, 2010, doi: 10.1109/RBME.2010.2084078.

[35] N. N. Getangama, J. R. De Bruyn, and J. L. Hutter, "Dielectric properties of PVA cryogels prepared by freeze-thaw cycling," J. Chem. Phys., vol. 153, no. 4, 2020, doi: 10.1063/5.0007251.

[36] C. Jin, C. Ma, Z. Yang, and H. Lin, "A force measurement method based on flexible PDMS grating," Appl. Sci., vol. 10, no. 7, 2020, doi: 10.3390/app10072296.

[37] H. K. Lee, S. Il Chang, and E. Yoon, "A flexible polymer tactile sensor: Fabrication and modular expandability for large area deployment," J. Microelectromechanical Syst., vol. 15, no. 6, pp. 1681–1686, 2006, doi: 10.1109/JMEMS.2006.886021.

[38] S. R. Stauffer and N. A. Peppast, "Poly(vinyl alcohol) hydrogels prepared by freezing-thawing cyclic processing," Polymer (Guildf)., vol. 33, no. 18, pp. 3932–3936, 1992, doi: 10.1016/0032-3861(92)90385-A.

[39] D. S. Mix, M. C. Stoner, S. W. Day, and M. S. Richards, "Manufacturing abdominal aorta hydrogel tissue-mimicking phantoms for ultrasound elastography validation," J. Vis. Exp., vol. 2018, no. 139, pp. 1–9, 2018, doi: 10.3791/57984.

[40] H. Baker and A. M. Kligman, “Measurement of Transepidermal Water Loss by Electrical Hygrometry,” Arch. Dermatol., vol. 96, no. 4, pp. 441–452, 1967, doi: 10.1001/archderm.1967.01610040091018.

[41] H. Tagami, M. Ohi, K. Iwatsuki, Y. Kanamaru, M. Yamada, and B. Ichijo, “Evaluation of the skin surface hydration in vivo by electrical measurement,” J. Invest. Dermatol., vol. 75, no. 6, pp. 500–507, 1980, doi: 10.1111/1523-1747.ep12524316.

[42] P. D. Welch, “The Use of Fast Fourier Transform for the Estimation of Power Spectra: A Method Based on Time Averaging Over Short, Modified Periodograms,” IEEE Trans. Audio Electroacoust., vol. 15, no. 2, pp. 70–73, 1967, doi: 10.1109/TAU.1967.1161901.

[43] M. A. Yokus and J. S. Jur, “Fabric-based wearable dry electrodes for body surface biopotential recording,” IEEE Trans. Biomed. Eng., vol. 63, no. 2, pp. 423–430, 2016, doi: 10.1109/TBME.2015.2462312.

[44] L. G. Tereshchenko and M. E. Josephson, “Frequency content and characteristics of ventricular conduction,” J. Electrocardiol., vol. 48, no. 6, pp. 933–937, 2015, doi: 10.1016/j.jelectrocard.2015.08.034.

[45] N. V. Thakor, J. G. Webster, and W. J. Tompkins, “Optimal QRS detector,” Med. Biol. Eng. Comput., vol. 21, no. 3, pp. 343–350, 1983, doi: 10.1007/BF02478504.

[46] S. A. Go, K. Coleman-Wood, and K. R. Kaufman, “Frequency analysis of lower extremity electromyography signals for the quantitative diagnosis of dystonia,” J. Electromyogr. Kinesiol., vol. 24, no. 1, pp. 31–36, 2014, doi: 10.1016/j.jelekin.2013.11.002.

[47] S. Gabriel, R. W. Lau, and C. Gabriel, “The dielectric properties of biological tissues: III. Parametric models for the dielectric spectrum of tissues,” Phys. Med. Biol. Phys. Med. Biol, vol. 41, no. 41, pp. 2271–2293, 1996, doi: 10.1088/0031-9155/41/11/003.

[48] N. J. Conn, K. Q. Schwarz, and D. A. Borkholder, “Nontraditional electrocardiogram and algorithms for inconspicuous in-home monitoring: Comparative study,” JMIR mHealth uHealth, vol. 6, no. 5, 2018, doi: 10.2196/mhealth.9604.

[49] A. Albulbul, “Evaluating major electrode types for idle biological signal measurements for modern medical technology,” Bioengineering, vol. 3, no. 3, 2016, doi: 10.3390/bioengineering3030020.

[50] E. S. Kappenman and S. J. Luck, “The effects of electrode impedance on data quality and statistical significance in ERP recordings,” Psychophysiology, vol. 47, no. 5, pp. 888–904, 2010, doi: 10.1111/j.1469-8986.2010.01009.x.

Appendix A

A.1 Pore size characterization

Label	Result
YY1	0.281 mm
XX1	0.297 mm
YY2	0.234 mm
YY3	0.344 mm
XX2	0.339 mm

Figure A1. Holes of nominal diameter 0.2 mm, were observed under the microscope to understand the kerf of the laser cutter.

A.2 Factors affecting the impedance change of phantom

The properties of the upper layer representing the stratum corneum for the phantom were simulated using a 100 µm thick layer fabricated by spin-coating a mixture of polydimethylsiloxane (PDMS), 2.5% W/W carbon black (CB) for conductance, and 40% W/W barium titanate ($BaTiO_3$) as a dielectric. The lower layer of the phantom mimicking deeper tissues was realized using polyvinyl alcohol cryogel (PVA-c) prepared with 0.9% W/W saline solution by a freeze-thaw technique. Impedance of the phantom can be decreased to simulate the impedance of the hydrated skin by varying the following factors:

A.2.1 Thickness of the upper layer

Impedance of hydrated skin is lower than dry skin, which could be simulated theoretically by reducing the thickness of the phantom's upper layer. The thickness of the upper layer was reduced to 50 microns, however, the material was difficult to handle while fabricating phantoms, and hence 100 microns was used.

A.2.2 Concentration of Carbon Black powder

Theoretically, increasing the concentration of carbon black powder would lower the impedance, however, the viscosity of the PDMS mixture increased, and the homogeneous mixing of carbon black powder became difficult.

A.2.3 Concentration of Barium Titanate

To investigate the effect of dielectric powder on the overall impedance of phantom, preliminary experiments were conducted, where different concentrations of barium titanate (0%, W/W 20% W/W, 40% W/W, 100% W/W) was tested on a 0% porosity phantom. 0% porosity phantom was chosen to independently study the effect of dielectric concentration. Preliminary results depicted no significant change in the impedance response (Figure A2). Therefore, the concentration of barium titanate was not varied in the recipe.

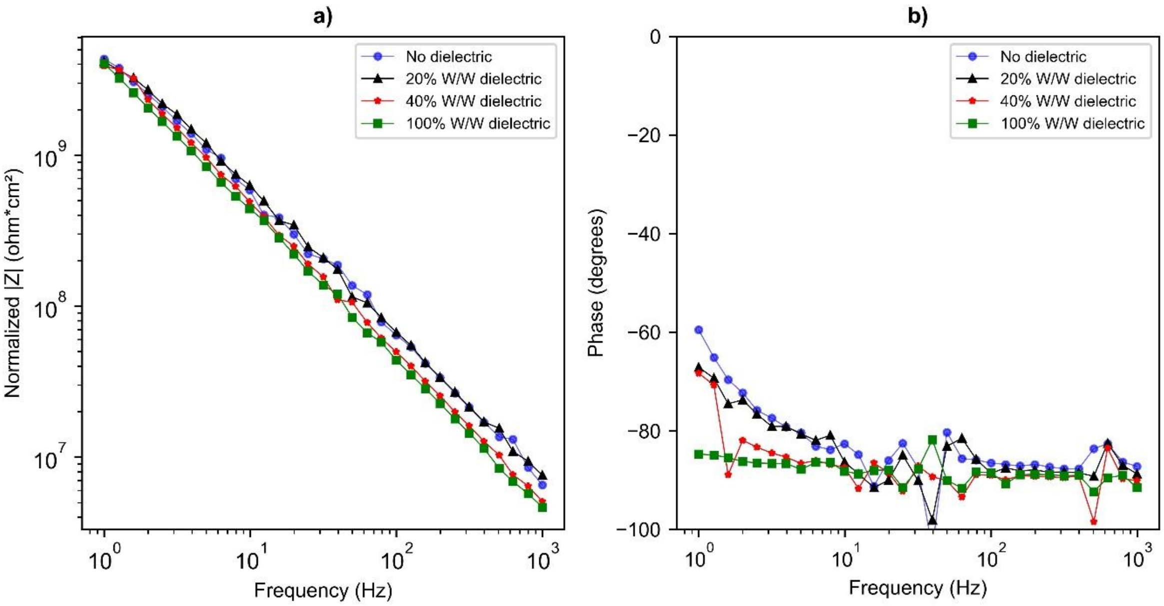

Figure A2. a) Impedance magnitude and b) phase response obtained on a 0% porosity phantom with no dielectric (blue circle), 20% W/W dielectric (black triangle), 40% W/W dielectric (red star), and 100% W/W dielectric (green square).

A.2.4 Concentration of saline water

Polyvinyl alcohol cryogel (PVA-c) simulating the deeper tissues was realized using 0.9 W/W% saline water and we believe this saline water is filling the pores of the phantom's upper layer. In theory, increasing the concentration of saline water would lead to lower impedance, however, this will vary both the properties of the lower and upper layers.

A.2.5 Porosity

A porosity-based approach allows to independently control the properties of the phantom's upper layer, by varying the amount of water within the upper layer, without varying the properties of the lower layer. Hence, porosity was the only variable used to lower the impedance. In addition, preliminary experiments were conducted to investigate if the difference in pore sizes would affect the dehydration speed of the phantom. Two consecutive measurements were performed on both 0.16% and 0.28% porosity phantoms. It was observed that the shift in magnitude impedance responses for first (n=1) and consecutive measurement (n=2) for both porosity phantoms were similar and the percentage change in phase response was less than 5%. (Figure A3). Hence, it was found that there were insignificant changes in the dehydration speed of the phantoms within the time frame of impedance measurement.

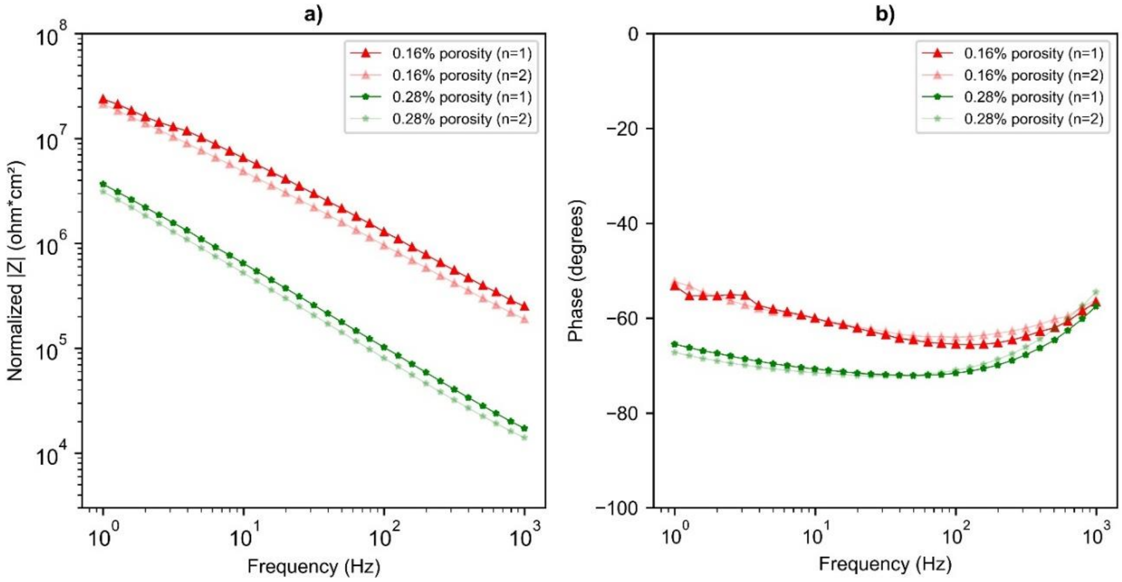

Figure A3. a) Impedance magnitude and b) phase response for the phantoms with porosity 0.16% (red triangle), and 0.28% (green star) respectively for first measurement (n=1). Translucent color denotes the consecutive measurement (n=2) for both porosity phantoms.

A.2.6 Concentration of PVA

PVA is simulating the deeper tissues which are typically resistive. As per literature, the combined skin impedance is of the order of 100Ω at high frequencies and is 10 kΩ-1MΩ at low (<1 kHz) frequencies. The concentration of PVA solution may affect the impedance of deeper tissues, however, it will not affect the overall impedance of the phantom at low frequencies significantly. The phantom developed in this work simulates the electrical properties in the low-frequency range, where we believe the upper layer and the saline water filling the holes play a significant role.

A.2.7 Freeze-Thaw Cycles

Preliminary experiments were conducted to investigate the effect of freeze-thaw cycles on phantom impedance. One phantom was fabricated using a single freeze-thaw cycle and another with three freeze-thaw cycles. Each freeze-thaw cycle comprised of 12 hours at -20°C and thaw for 12 hours at room temperature. It was found that the slope of the phantom fabricated with the single freeze-thaw cycle had a similar slope to that of human skin (Figure A4). Increasing the freeze-thaw cycles, not only varied the impedance but also varied the slope, hence, a single freeze-thaw cycle was used for fabricating the phantom.

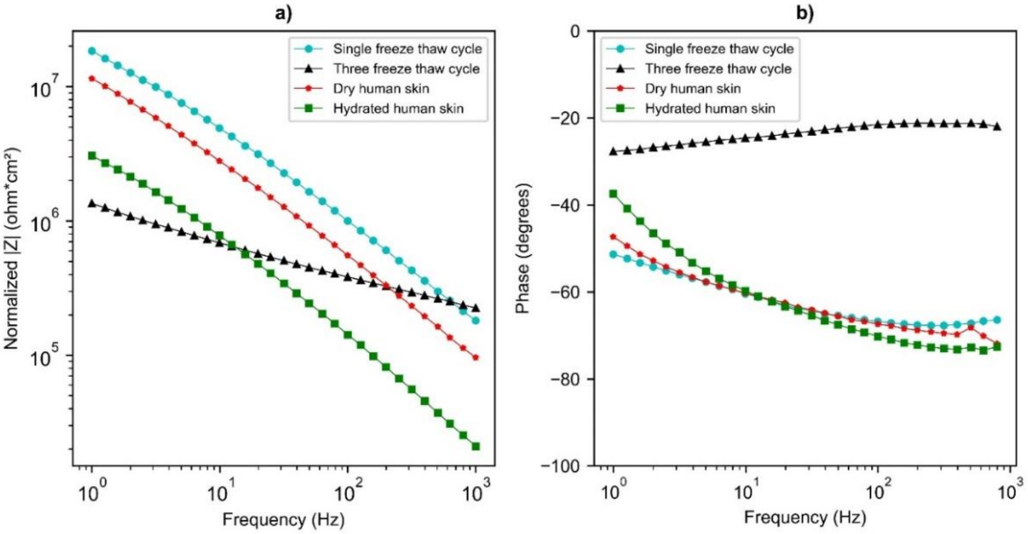

Figure A4. a) Impedance magnitude and b) phase response on a 0.16% porosity phantom for single freeze-thaw cycle (cyan circle), three freeze-thaw cycles (black triangle), untreated skin (red star), and hydrated skin (green square) obtained on human arm (across one subject). Each freeze-thaw cycle includes 12 hours at-20°C and thaw for 12 hours at room temperature.

A.3 Reproducibility of phantom

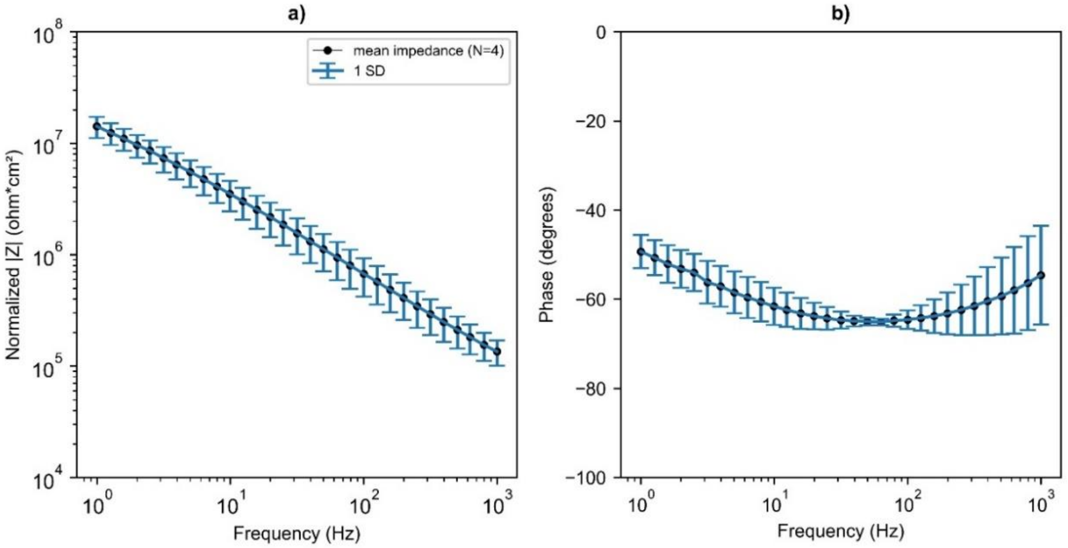

Figure A5. a) Impedance and b) phase response for phantom with porosity 0.16% obtained across four phantoms. Each point is the mean across four replicates; error bars represent one standard deviation.

Chapter 4: Dependence of Skin-Electrode Contact Impedance on Material and Skin Hydration

Published as **K. Goyal**, D. A. Borkholder, and S. W. Day, “Dependence of Skin-Electrode Contact Impedance on Material and Skin Hydration,” *Sensors*, vol. 22, no. 8510, 2022, doi: 10.3390/s22218510.

4.1 Abstract

Dry electrodes offer an accessible continuous acquisition of biopotential signals as part of current in-home monitoring systems but often face challenges of high-contact impedance that results in poor signal quality. The performance of dry electrodes could be affected by electrode material and skin hydration. Herein, we investigate these dependencies using a circuit skin-electrode interface model, varying material and hydration in controlled benchtop experiments on a biomimetic skin phantom simulating dry and hydrated skin. Results of the model demonstrate the contribution of the individual components in the circuit to total impedance and assist in understanding the role of electrode material in the mechanistic principle of dry electrodes. Validation was performed by conducting *in vivo* skin-electrode contact impedance measurements across ten healthy human subjects. Further, the impact of the electrode on biopotential signal quality was evaluated by demonstrating an ability to capture clinically relevant electrocardiogram signals by using dry electrodes integrated into a toilet seat cardiovascular monitoring system. Titanium electrodes resulted in better signal quality than stainless steel electrodes. Results suggest that relative permittivity of native oxide of electrode material come into contact with the skin contributes to the interface impedance, and can lead to enhancement in the capacitive coupling of biopotential signals, especially in dry skin individuals.

Keywords: Dry electrodes; In-home monitoring; Biopotential signals; Electrode material; Skin-electrode contact impedance

4.2 Introduction

Accurate and reliable in-home monitoring of biopotential signals such as electrocardiogram (ECG) can provide early diagnosis of cardiac health conditions [1], [2]. Clinically, ECG is performed using wet electrodes, which contain a conductive gel between the skin and the Ag/AgCl metal contact. The mechanistic principle is based on an electrode-electrolyte interface's electrochemical reactions, which shows that resistive coupling is dominant due to the charge transfer phenomenon [3]. The presence of gel also moistens the skin, which helps in lowering the skin-electrode impedance [4]. Wet electrodes provide high signal quality, however are single-time use, need skin preparation, and can cause skin irritation. In addition, Huigen et al. [5] demonstrated that the main origin of noise in surface electrodes originates in the electrolyte-skin interface and highly depends on the electrode gel. Though wet electrodes exhibit excellent signal quality for short duration recordings, they are not suitable for long-term monitoring as the gel dries over time, which leads to signal degradation.

Dry electrodes have the potential to overcome all the challenges associated with wet electrodes; they are easy to use, reusable, and do not lead to discomfort. However, dry electrodes have an unstable electrochemical interface due to the absence of gel, which results in high and variable contact impedance, drift, and therefore low repeatability. Skin-electrode contact impedance plays a significant role in the performance of dry electrodes and a low skin-electrode contact impedance is desirable for the acquisition of a high-quality signal [6]. To achieve a lower skin-electrode contact impedance, it is important to understand the signal transfer mechanism occurring at the interface and the factors contributing to the skin-electrode contact impedance. In dry electrodes such as made from stainless steel, no actual charge crosses the electrode/electrolyte interface, as it is an inert metal and difficult to oxidize or dissolve [7]. Instead, a displacement current is present as a result of capacitance at the interface. Moreover, in the absence of any gel or sweat on the skin, the behavior of metal electrodes made from inert materials can be considered capacitive transducers [8]. However, it is necessary to understand how the signal is capacitively coupled from the body to the sensing electrodes. In this work, the dry electrode model is considered to act like a capacitive transducer. The heart causes immediate changes in the electric potential within the tissue, which is sensed by the metal electrodes. The metal electrode is thought to act as one plate of a capacitor, with the deeper tissue layers as the other plate of the capacitor. Thus, in our hypothesis, we considered the thin metal native oxide, air gaps, and the dry outer layer of the skin (stratum corneum) together to act as a dielectric.

For skin-based biopotential signals, the topmost layer of the skin, the stratum corneum, is important as the impedance of this layer is a major portion of the total skin impedance, and it dominates the skin impedance in the low-frequency range (1 Hz to 10 kHz) [9]. In the absence of electrolyte/sweat, the higher stratum corneum impedance makes the acquisition of high-quality signals with dry electrodes very challenging, especially in people with dry skin. Researchers have tried to overcome the high stratum corneum impedance by developing micro tips/pin-based contact electrodes [10], where the surface of the electrodes coming in contact with the skin consists of pins/spikes, with a height of the order of 150 μm [11], which is sufficient to penetrate the 20 μm-thick stratum corneum. Such an approach overcomes the high impedance offered by the stratum corneum and the charge transfer mechanism is similar to that of wet electrodes [10]. One of the major drawbacks of such an approach is it can lead to skin irritation and infection, as the pins pierce the skin and come into contact with the fluids underneath the stratum corneum [11]. Some other types of dry electrodes have been developed with polymer coatings to enhance the electrochemical performance [4], [12]. When left for a certain amount of time on the skin, they are likely to perform similarly to wet electrodes for two reasons. First, the impedance of the stratum corneum is greatly affected by changes in hydration. Due to the accumulation of perspiration under the electrodes, it hydrates the skin and the capacitance of the interface improves. Second, the sweat acts as the electrolyte and facilitates the transfer mechanism similar to that of wet electrodes. One major drawback of such types of electrodes is that fabrication is complex and polymers may flake off [4].

To overcome the challenges of higher skin-contact impedance, researchers have also tried increasing the area of the electrode [12], [13]. However, increasing the area alone to achieve lower skin-electrode contact impedance has a limited application, and is not applicable for miniature devices such as watches. Other efforts include using different electrode materials to improve the performance of dry electrodes [14], [15]. The classical approach followed by researchers for characterizing different electrode materials is entirely empirical and consists of carrying out experiments on human skin with different chosen materials followed by qualitative or quantitative comparison with the wet electrodes (gold standard) [14]–[16]. Subsequently, the most satisfactory material based upon the performance is chosen. One of the major limitations of this empirical approach is the inter- and intra-subject variability in the skin properties. Also, some researchers have used the equivalent electrode-skin impedance modeling and compared the wet and dry electrode performance [17], and demonstrated the decrease in impedance corresponding to the increase in the electrode area [12]. However, the role of electrode material (typically metal-based) in the skin-electrode interface has not been studied and the rationale behind metal-based electrode material performance in the dry case scenario is not yet understood [14], [15]. Thus, there is a need to understand the optimal set of solutions that can help in designing in-home monitoring devices effectively. This understanding will help to optimally design the electrodes for applications such as a watch with a miniature area, people with dry skin, and measurement locations where the signal amplitude is weak (<0.1 mV for buttocks ECG) such as measurement from the back of the thigh using a toilet seat [18].

The present work focuses on investigating the electrode-skin impedance dependence on the electrode material, area, and skin hydration by developing a skin-electrode interface circuit model. The circuit model includes aspects of prior models using a network of passive electrical circuit elements and incorporates a rationale for the electrode material. Parameter values of components within the model were determined by fitting empirical data from controlled benchtop experiments on a skin phantom designed in our previous work [19]. The phantom simulates the effect of skin hydration in a controlled predictive manner and mimics the electrical properties of the skin in the low-frequency range. The circuit parameters were fitted and computed to understand the effect of variables such as material, area, and hydration status in the skin-electrode contact impedance. Validation was performed using *in vivo* human subject impedance data captured across ten healthy subjects using impedance spectroscopy. Lastly, ECG was acquired using different dry electrode configurations, integrated into a toilet seat cardiovascular monitoring system, and the ability to capture high-ECG signal quality is demonstrated.

4.3 Materials and Methods

4.3.1 Electrode Material

Several metal-based candidate materials comprising stainless steel, titanium, copper, silver, nickel, gold, and brass were explored for consideration as electrode materials. The selection criteria included: high electrical conductivity, high corrosion resistance, hypoallergenic, robust to abrasion, and chemical resistant. Of the materials evaluated, stainless steel 304 (SS) and titanium grade 2 (Ti) were selected as the most readily available materials.

The electrical conductivity of the selected materials was investigated using a four-point probe setup (Model RM 3000, Jandel Engineering Ltd., UK). The surface roughness of the materials was measured using a non-contact optical profilometer (ST400, Nanovea Inc, Irvine, CA, USA) to investigate the effective contact area coming in contact with the skin and quantitative measures of surface roughness such as the arithmetic average of the roughness profile (Ra) were obtained. SS is an alloy that contains iron, chromium, and nickel [20], thus the composition of native oxides was performed using auger electron spectroscopy (AES) to examine the composition of the oxides present on the stainless surface that directly contacts the skin. In addition, ion sputter etching was performed to evaluate the composition as a function of depth. AES was also performed across the titanium sample to investigate the composition of the native titanium oxide [21].

4.3.2 Skin-Electrode Impedance Equivalent Model for Dry Electrodes

4.3.2.1 Impedance Measurements on Phantom

Skin-electrode contact impedance was investigated by carrying out impedance measurements on the phantom developed in previous work [19]. To summarize, the fabricated phantom comprises two layers representing the deeper tissues and stratum corneum. The lower layer simulated deeper tissues and the hydration of the stratum corneum was modeled in a controlled way by varying porosity of the phantom's upper layer. Impedance spectroscopy measurements were performed with a potentiostat (Reference 600, Gamry Instruments Inc., Warminster, PA, USA) in a two-electrode configuration, where the working (W) and counter (C) probe carried the current, and working sense (WS) and reference (R) measured voltage. Electrodes were fabricated from a 0.3 mm-thick sheet, as this was easy to cut. Different electrode configurations consisted of electrode material: stainless steel and titanium with electrode area: 4 cm^2 and 9 cm^2, each arrangement tested in a controlled manner on a set of phantoms simulating dry and hydrated skin. The hydration state modeled with 0.16% porosity simulated dry skin and that with 0.28% mimicked hydrated skin impedance. Using the potentiostat, a frequency sweep of 0.1 Hz - 100 kHz was performed and an impedance response was obtained.

4.3.2.2 Development of Model

A simplistic model for metal-based dry electrodes consisting of a circuit model of the electrode and the skin (Figure 4.1) was developed using Gamry Echem Analyst software. Deeper tissues were represented by a resistor (R_d), and the stratum corneum by a capacitor (C_{sc}) and resistor (R_{sc}) in parallel. The contact interface between the skin and electrode, including the thin native oxide, air gaps due to the skin roughness, stiff metal, and the stratum corneum interface was considered to act as a dielectric in the transduction mechanism and modeled by a contact capacitor (C_c). Thus, the electrode was thought to act as one of the capacitor plates, and the interface located at the stratum corneum was considered as the other capacitor plate. Both the relative permittivity (also known as dielectric constant) and the thickness of the native oxide layer are material-dependent. The air gap depends on the pressure and effective contact between the electrode and the skin. The dielectric properties of the stratum corneum depend on skin type, part of the body, hydration level, and are highly subject-dependent. Thus C_c was considered to vary as per equation (1), where the capacitance is directly proportional to the relative permittivity and area, inversely proportional to the distance between two plates:

$$C = \frac{\varepsilon_0 \varepsilon_r A}{d} \qquad (1)$$

Where ε_0 is the relative permittivity of free space, ε_r is the relative permittivity of a material, A is the area of the plate, and d is the distance between the two plates.

The parameters representing the stratum corneum, C_{sc} and R_{sc} were modeled for dry and hydrated phantom similar to that of dry and hydrated skin. To obtain good contact between the electrode and the phantom's surface, a micromanipulator (M325, World Precision Instruments, Sarasota, FL, USA) was used to hold the electrode against the phantom's surface, as the effective contact between the electrode and the skin affects the interface impedance significantly [22]. The micrometer head was adjusted until it just touched the snap-on connector in order to hold the electrode against the phantom's surface. Thus, this ensured a consistent and very low pressure between the electrode and phantom's surface. The capacitive impedance holds an inverse relation to capacitance given by equation (2) and substituting the value of C, using equation (1), results in equation (3):

$$Z_c = \frac{1}{\omega C} \qquad (2)$$

$$Z_c = \frac{d}{\omega \varepsilon_0 \varepsilon_r A} \qquad (3)$$

Where $\omega = 2\pi f$, ω is in rad/sec, and f is the frequency (Hz).

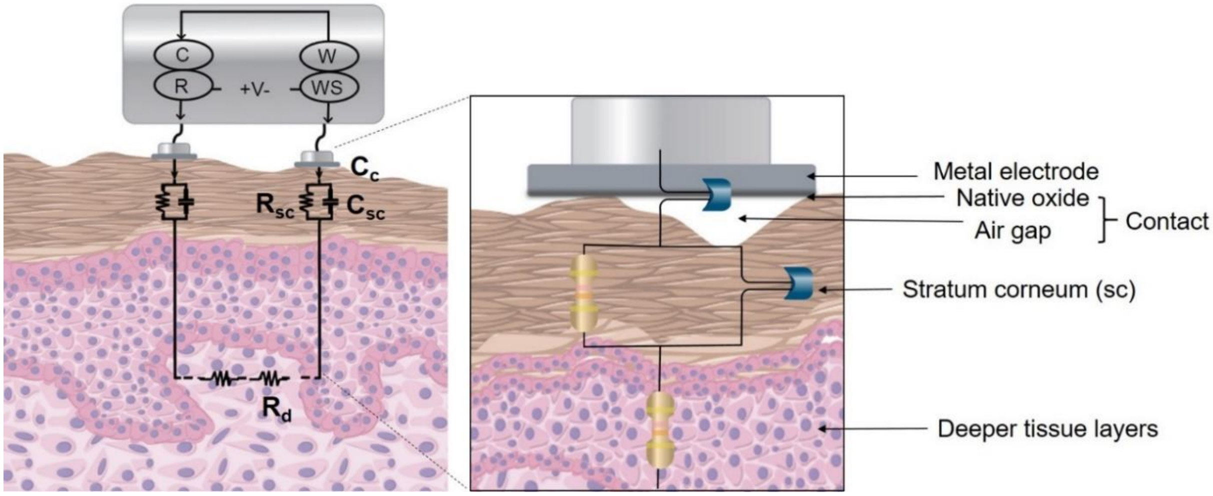

Figure 4.1. Two-electrode setup and an equivalent skin-electrode model for metal-based dry electrodes. Two- electrode configuration setup is shown where C, R, W, and WS represent counter, reference, working, and working sense leads of the potentiostat respectively. An analogous electrical equivalent circuit is shown where contact is represented by a capacitor (C_c), along with the stratum corneum as a parallel combination of resistor (R_{sc}) and capacitor (C_{sc}), and deeper tissue layers as a resistor (R_d). The zoomed-in view represents the air gaps due to the surface roughness of the stratum corneum, the thin native oxide that comes in direct contact with the skin.

The model (Figure 4.1) was used to fit the impedance response obtained across various electrode configurations comprising different electrode materials and sizes, tested on a dry and hydrated phantom. For understanding the physics and the mechanism, the stratum corneum and the contact interface components were thought to be capacitors, as they have a physical meaning in the real world. However, a constant phase element was used for the fitting, as it accounts for factors such as non-uniform current distribution and surface roughness [17], [20]. The constant phase element is represented by equation (4), where *CPE* represents the capacitance, $\omega = 2\pi f$, ω is in rad/sec, f is in Hz, α is the exponent, and lies between ($0 < \alpha \leq 1$). From equations (2) and (4), When $\alpha = 1$, the constant phase element becomes equivalent to a capacitor. The modeling parameters representing deeper tissue layers (R_d), stratum corneum (R_{sc}, CPE_{sc}) and contact interface (CPE_c) were computed by fitting the obtained impedance response. The fitting of the circuit parameters was restricted to lower and upper bounds, to avoid physically unreasonable values [6]. As per values found in the literature, R_d was assigned 100 Ω – 10 kΩ, R_{sc} varied in the range of 10 kΩ - 10 MΩ, and CPE_{sc} ranged from 1-500 nSs^{α} (S and s represent Siemen and secs respectively) with $0 < \alpha \leq 1$ [6], [17]. CPE_c was assigned a wide range of 1 – 20000 nSs^{β} with $0.5 < \beta \leq 1$. The C_{sc} was calculated by substituting the obtained values for R_{sc}, CPE_{sc}, and α in equation (5). C_c was calculated by using equation (6), where CPE_c along with exponent β represents the constant phase element of the interface and ω_{max} is the frequency at which the imaginary part of impedance reaches maximum [23]. The error associated with calculated fitted parameters was investigated. The goodness of fit (chi-squared) computed after fitting the parameters provided the fitting accuracy, which can be defined as the square of the percentage error between the experimental and fit values [24]. For this work, a value of an order of (10^{-2}) was considered a sufficiently good fit, which indicates a 10% difference between the experimental and fitted data [25] and a model was considered valid if the error associated with every calculated fitted parameter was smaller than its respective components.

$$Z_{CPE} = \frac{1}{(j\omega)^{\alpha}\mathrm{CPE}} \tag{4}$$

$$C_{sc} = \frac{(\mathrm{CPE_{sc}R_{sc}})^{1/\alpha}}{\mathrm{R_{sc}}} \tag{5}$$

$$C_c = \mathrm{CPE_c}(\omega)_{\mathrm{max}}{}^{\beta\text{-}1} \tag{6}$$

4.3.3 Healthy Subject Testing

4.3.3.1 *In Vivo* Skin-Impedance Measurements

To evaluate the effect of SS and Ti *in vivo* on the skin-electrode interface, measurements were conducted across the thigh, using a toilet seat platform. It consists of a pair of SS electrodes integrated on the right side and a pair of Ti electrodes on the left side of the toilet seat (Figure 4.2). The human subject study was performed across ten healthy subjects under informed consent and protocol approved by the Institutional Review Board at Rochester Institute of Technology. A two-electrode configuration was used, as to measure the skin-electrode contact impedance, for studying the interaction of metal dry electrodes with the skin. Potentiostat (Reference 600, Gamry Instruments Inc., Warminster, PA, USA) was used to generate a voltage signal of 25mV RMS AC in magnitude, and a frequency sweep of 0.1 Hz - 100 kHz was performed. In preliminary experiments, we confirmed the linearity of the phantom over a range of 5-25 mV, shown in the supplementary information (Fig. S1). To ensure electrical safety, both the potentiostat and the laptop were plugged into a medical-grade isolation transformer (ILC-1400MED4, TSI Power Corp., Antigo, WI, USA). In the first recording, the leads of the potentiostat were connected to the right side of electrodes consisting of SS electrodes while the Ti electrodes were covered by a vinyl sheet. The subject was asked to sit on the seat, such that the skin of just one thigh was in contact with one set of electrodes to measure the impedance. The subject was instructed to stand up, the vinyl sheet was removed, the leads of the potentiostat were connected to Ti electrodes and the impedance measurements were acquired. It took approximately five minutes for each measurement. Impedance response corresponding to both the SS and Ti electrodes was analyzed. Each subject’s paired t-test was used to compute if the differences between the impedance responses obtained for SS and Ti were statistically significant ($p \leq 0.05$).

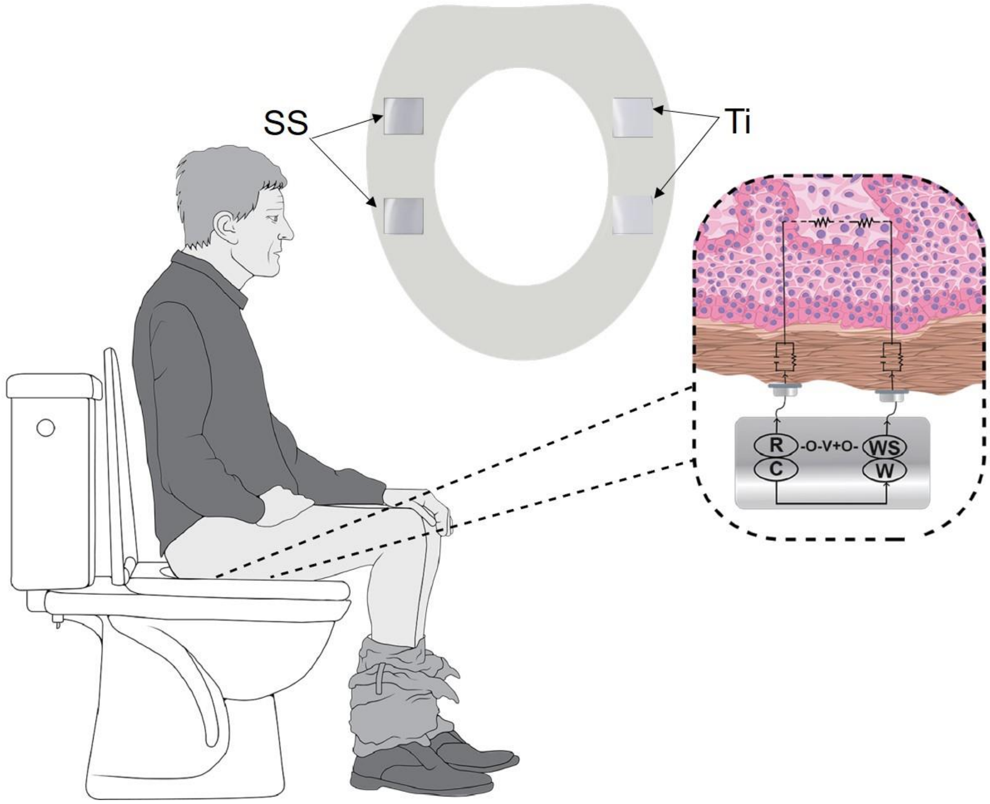

Figure 4.2. Experimental setup for acquiring the skin-electrode contact impedance measurements. Stainless steel (right side) and titanium electrodes (left side), 9 cm^2 each, were integrated into a toilet platform. The zoomed-in view of the skin cross-section coming in contact with the two electrodes along with the electrical equivalent model of the electrode-skin interface is shown.

4.3.3.2 Electrocardiogram Acquisition

Immediately after recording the skin-electrode contact impedance measurements, ECG was captured using two sizes of SS and Ti electrodes fitted within a previously designed fully integrated toilet seat [18]. All the instrumentation/electronics were integrated into the toilet seat, and battery powered [18]. The ECG signal was differentially measured using two electrodes and an instrumentation amplifier with a high common-mode rejection ratio. The captured data was sent to a laptop via an onboard Bluetooth Low Energy radio. Different electrode configurations were integrated into the toilet seat and tested across all the subjects (N=10). Electrode configurations comprised areas of 6 cm^2, and 90 cm^2, for both SS and Ti (Figure 4.3). For comparing signals to a high-quality signal, an alcohol swab was used in place of traditional wet electrodes. Two seat setups were used, one integrated with 90 cm^2 SS and the other with 90 cm^2 Ti electrodes. To achieve a smaller area of electrodes, 90 cm^2 electrodes were covered with a vinyl mask, only exposing the 6 cm^2 area (Figure 4.3). Preliminary experiments showed that electrodes completely covered with the vinyl sheet resulted in no ECG at all, thus indicating that there was no capacitive coupling of ECG signal occurring through the vinyl sheet. The ECG recordings start immediately when the subject sits on the toilet seat. Due to the measurement location, back-to-back ECG measurements across different electrode configurations were performed. For all the subjects, the measurements were performed in the following order: 90 cm^2 Ti; 90 cm^2 SS; 6 cm^2 Ti; 6 cm^2 SS. Lastly, alcohol swabs (AS) were placed on both the smaller area electrodes Ti 6cm^2 followed by SS 6 cm^2. 90-second recordings were made for all the electrode configurations. The total duration for conducting the entire protocol for ECG recordings across each subject was around 20 minutes. All the measurements were conducted in the controlled lab environment and the subjects were asked to sit as still as possible.

Figure 4.3. Fully integrated seat with 90 cm^2 stainless steel (top-left), 90 cm^2 titanium (top-right). Electrodes are covered with a vinyl mask (shown in blue), to achieve a smaller area of 6 cm^2 of stainless steel (bottom-left) and titanium (bottom-right). For gold standard, alcohol swabs were placed on the 6 cm^2 electrodes for both materials.

4.3.3.3 Signal Processing and Analysis

For the preprocessing of the raw ECG signal, five seconds of data were removed from the beginning and the ending of the 90-second acquisition. Signals were band-pass filtered using a second-order Butterworth filter (1 Hz-40 Hz) and a notch filter at 60 Hz [26]. The ECG signal's main power lies in 5 Hz-15Hz [27],[28] thus the signal quality evaluation was performed by calculating the power spectral density of the signal in the 5 Hz-15 Hz to that of the overall signal between 5 Hz-40 Hz [29], [28]. The power spectral density was calculated by Welch's method [30] and the power was computed by approximating the area under the power spectral density curves. Thus, the power spectral density ratio (PSDR) can be defined as the proportion of the QRS power to that of overall signal power [28] as shown in equation (7). Extremely high PSDR indicates the presence of large noisy spikes [28], thus a threshold was empirically chosen, and the signal was considered to be of analyzable quality if the PSDR was less than 0.80 (Figure 4.4). PSDR is a heuristic measure and a threshold of 0.8 was empirically determined to provide rejection of poor-quality signals. The empirically determined threshold value was in agreement with the previously reported threshold value (0.8) by Li et al [28]. The power spectral density curves for the ECG signals depicting PSDR of 0.5 (representing acceptable signal quality) and PSDR of 1 (representing unacceptable signal quality) are shown in the Appendix B.

$$\text{PSDR} = \frac{\int_{5\text{ Hz}}^{15\text{ Hz}} \text{PSD}}{\int_{5\text{ Hz}}^{40\text{ Hz}} \text{PSD}} \tag{7}$$

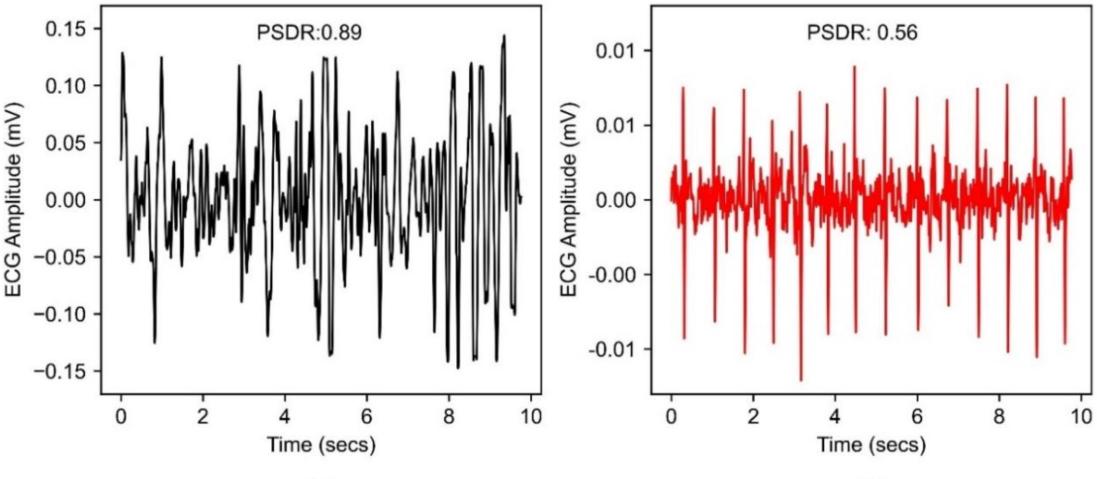

(a)

(b)

Figure 4.4. An example of the power spectral density ratio (PSDR) calculation computed for ECG signal (a) PSDR for a poor-quality signal with large noisy spikes results in a value of 0.89 and is characterized as unanalyzable. (b) Clean ECG signal results in a value of 0.56 and is considered an analyzable signal.

Signal-to-noise ratio (SNR) of the analyzable signals was computed to quantitatively compare the signal quality across all the electrode configurations. The filtered ECG signal was used and the r-peaks were identified based upon the Pan Tompkins algorithm along with ECG signal delineation using Neurokit2, a python package for signal processing [31]. After locating the r-peaks, the S wave was identified as the nearest point to the right of the R wave, where the downward deflection has a minimum. SNR was calculated by using equation (8), similar to [32]. The peak-peak signal (V_{signal}) value was obtained by calculating the difference between the R wave (maximum) and S wave (minimum), and averaging across each ECG cycle. Based on the ECG morphology, peak-peak noise (V_{noise}) was calculated as the difference between the maximum noise and the minimum noise in the segment after the T wave ends and before the P wave of the next ECG signal begins (Figure 4.5). Thus, the noise was calculated as the peak-peak variations in the segment between the two ECG cycles, excluding the P wave, QRS component, and T wave [32]. The mean was computed for the peak-peak noise across ECG cycles present in a 90-second recording. Further, the ratio of peak-peak signal and peak-peak was converted to decibels (dB). For the ECG signals that were identified as unanalyzable as their PSDR was greater than 0.80, they were assigned an SNR value of zero.

$$\mathrm{SNR} = 20 \times \log_{10} \frac{V_{\mathrm{signal}}}{V_{\mathrm{noise}}} \qquad (8)$$

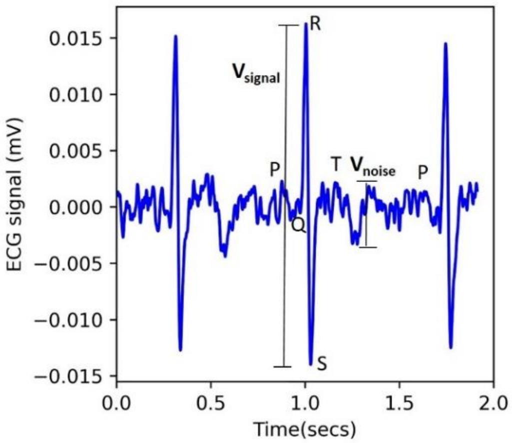

Figure 4.5. An example of signal-to-noise ratio (SNR) calculation, where V_{signal} represents the peak-peak signal (R and S wave), and V_{noise} represents the peak-peak noise in the segment after the T wave ends and before the P wave of the next ECG cycle begins.

Kurtosis has been widely used to determine the ECG signal quality [16], [28], [29]. Kurtosis was used as a metric to further evaluate the quality of the ECG signal across different configurations. Kurtosis is a statistical measure, as defined in equation (9), and provides a measure of the shape of the curve. Higher kurtosis indicates the dominance of the QRS complex and lower indicates the absence of the QRS complex. Before calculating the kurtosis, median filtering was performed on the processed ECG signal, to remove the large spikes, as kurtosis is sensitive to outliers [33]. Kurtosis was calculated across a window of 10 secs and an average was computed.

$$\text{Kurtosis} = \frac{1}{n}\sum_{i=1}^{n}\left[\frac{x_i - \mu}{\sigma}\right]^4 \tag{9}$$

Where μ is the empirical estimate mean of x_i, and σ is the empirical estimate standard deviation of x_i.

4.4 Results

4.4.1 Electrode Material Characterization

The electrical conductivity obtained using four-point probe measurements for Ti and SS resulted in 2.17×10^6 $S.m^{-1}$ and 1.30×10^6 $S.m^{-1}$ respectively. This was in accordance with the literature where the conductivity of Ti is reported as 2.38×10^6 $S.m^{-1}$ and SS as 1.45×10^6 $S.m^{-1}$ [34]. Thus, both the SS and Ti were found to be highly electrically conductive. Surface roughness measured using an optical profilometer resulted in an arithmetic average of roughness profile (R_a) to be 1.3 microns for the Ti and 1.6 microns for the SS. This indicates that the surface of both the materials comprising native oxide are similar in smoothness, and it can be considered that the effective area in contact with the body is approximately the same for both materials. The auger spectrum for SS as a function of kinetic energy shows that only iron oxide was present in the SS native oxide along with carbon and oxygen (Figure 4.6). Thus, the peak at 711 eV indicated the presence of iron oxide (Fe_2O_3) [35]. After depth profiling, it was found that the concentration of carbon and oxygen decreased, chromium and nickel became visible, and iron increased. For titanium, the AES spectrum revealed the presence of titanium along with carbon and oxygen and the concentration of titanium increased after depth profiling. The peak at 420 eV indicated that the oxide composition comprises TiO_2 [36].

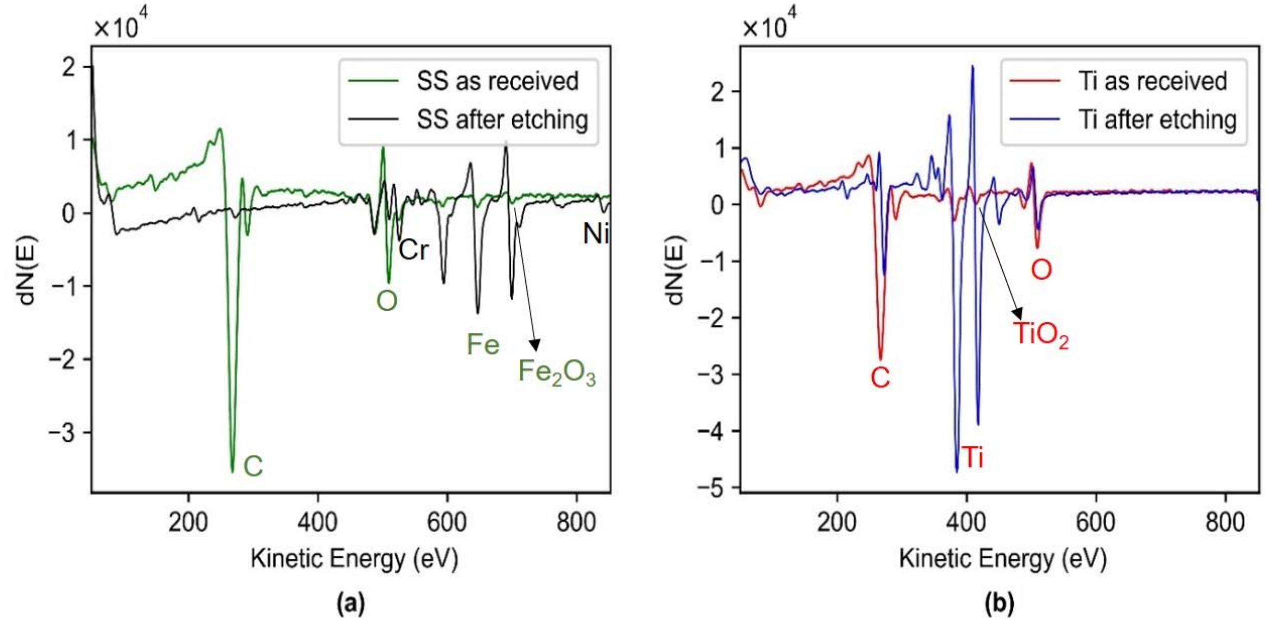

Figure 4.6. (a) AES profile for SS as received, which shows the presence of iron oxide (Fe_2O_3) along with carbon and oxygen. AES profile for SS after etching shows chromium and nickel become visible, and iron concentration increases. (b) AES profile for Ti as received, which shows the presence of titanium along with carbon and oxygen and the peak at 420 eV indicates the presence of TiO_2. AES profile of Ti after etching shows the concentration of titanium increases and oxygen decreases.

4.4.2 Skin-Electrode Contact Impedance Model Parameters

The Bode plot showing the impedance response with respect to frequency resulted in a lower impedance for the 9 cm^2 electrode as compared to the 4 cm^2 electrode (Figure 4.7a). This indicates that the higher-area electrode leads to a lower impedance and matches with the previously reported work [12], [13], [37]. The equivalent impedance model was found to have a good fit to the experimental data, shown as a solid line in Figure 4.7a) for both 4 cm^2 and 9 cm^2 area electrodes tested on a dry skin phantom. The modulus of impedance for both of them was observed to have a similar slope and the impedance of the 4 cm^2 electrode was 2 times higher as compared to that of a 9 cm^2 electrode. This is in complete agreement, as the area of the electrode (9 cm^2) is approximately twice the area of the other electrode (4 cm^2). Thus, the developed phantom was found to scale the effect of impedance to that of the electrode area. The phase response for both 4 cm^2 and 9 cm^2 depicted a resistive behavior and higher frequencies and a capacitive behavior at lower frequencies (Figure 4.7b). The fit model was within 5 degrees for both 4 cm^2 and 9 cm^2 electrodes in the low-frequency range of 1 Hz – 1000 Hz. Further, the computed parameters obtained after fitting the model (**Table 4.1**) indicated that the R_{sc} reduced by two times and both C_{sc} and C_c increased by 2.5 times. This is consistent with the mathematical relationship, as resistance is inversely proportional to area and capacitance is directly proportional to the area, thus clearly depicting the effect of area on the skin-electrode contact impedance (**Table 4.1**). R_d was close for both 9 cm^2 and 4 cm^2 electrodes, indicating the phantom properties were stable during the course of experiments.

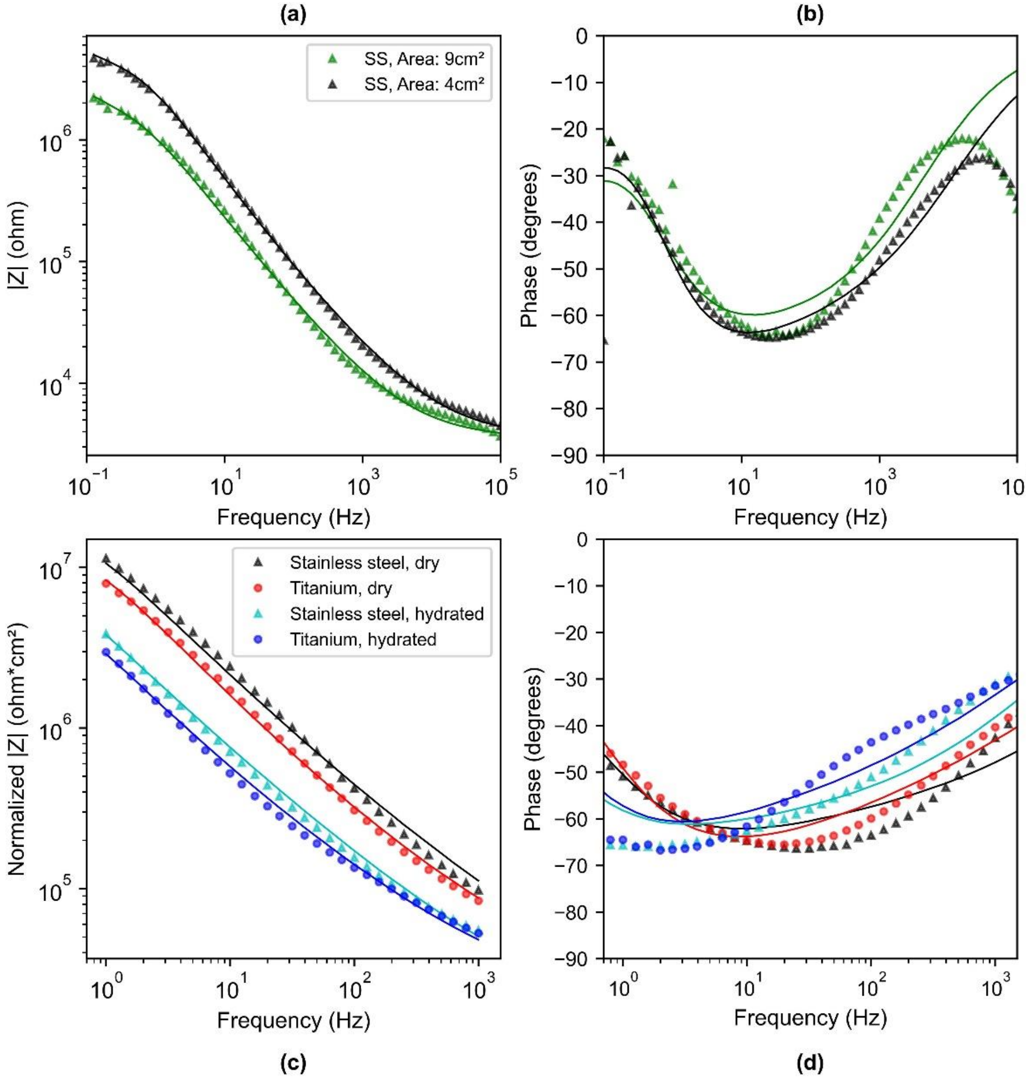

Figure 4.7. (a) Bode plot depicting the impedance magnitude (b) and phase response for SS electrode of area 9 cm^2 and 4 cm^2 on a dry phantom. (c) Bode plot depicting the normalized impedance magnitude and (d) phase response for SS (9 cm^2) and, Ti (9 cm^2) on a dry and hydrated phantom. Normalized impedance response is shown across the low-frequency range 1 Hz - 1000 Hz (crucial for biopotential signals) to clearly show the differences between material and hydration in the lower frequency regime. Points represent the measured data and the solid lines represent the fitted curve obtained via the model.

Table 4.1. Equivalent impedance fitting parameters obtained for impedance response across SS electrodes of 4 cm^2 and 9 cm^2 area electrodes on a dry phantom. R_d and R_{sc} represent the resistance of deeper tissue layer and stratum corneum respectively; C_{sc} and C_c represent the real capacitances of stratum corneum and contact, obtained from the fitted constant phase elements.

Electrode Area	R_d (kΩ)	R_{sc} (MΩ)	C_{sc} (nF)	C_c (μF)	Goodness of fit
4 cm^2	1.77	1.62	151	0.68	0.017
9 cm^2	1.75	0.70	391	1.34	0.044

The bode plots in Figure 4.7c show the normalized impedance with respect to area and depict the impedance response corresponding to different electrode materials, on a dry and hydrated phantom. The impedance response for the Ti electrode was lower than that of the SS electrode (Figure 4.7c). The area-normalized electrode-skin impedance at 10 Hz for SS and Ti was 2.40 and 1.70 MΩ cm^2 on a dry phantom. The fitted phase response of Ti and SS on both dry and hydrated phantom was within 10 degrees of that of experimental data. The model fitting parameters R_d, R_{sc}, and CPE_{sc} were fixed during the fitting of the impedance curve for SS and Ti for a dry phantom, and CPE_c indicated the effect of electrode material on the skin-electrode interface. C_c for Ti (267 nF cm^{-2}) was 2.3 times higher than that of SS (114 nF cm^{-2}), indicating better capacitive coupling for Ti than SS (**Table 4.2**).

Table 4.2. Equivalent impedance fitting parameters obtained for impedance response across SS and Ti on a dry and hydrated phantom. Impedance normalized to the area is shown. R_d and R_{sc} represent the resistance of deeper tissue layer and stratum corneum respectively; C_{sc} and C_c represent the real capacitances of stratum corneum and contact, obtained from the fitted constant phase elements.

Electrode Material (Phantom hydration status)	R_d (kΩ cm^2)	R_{sc} (MΩ cm^2)	C_{sc} (nF cm^{-2})	C_c (nF cm^{-2})	Goodness of fit
Ti (dry)	9.3	6.4	41	267	0.007
SS (dry)	9.3	6.4	41	114	0.031
Ti (hydrated)	9.3	3.0	190	420	0.042
SS (hydrated)	9.3	3.0	190	224	0.035

With the change in the hydration status of the phantom, an impedance of an order of magnitude lower was found for the hydrated phantom as compared to the dry phantom (**Table 4.2**; Hydrated phantom, R_{sc} (3.0 MΩ cm^2) was lower, and C_{sc} (190 nF cm^{-2}) was 4.6 times higher than the dry phantom (6.4 MΩ cm^2; 41 nF cm^{-2})). The combination of R_{sc} and C_{sc} lowered the total impedance by an order of magnitude, which indicates that the stratum corneum properties have a significant contribution to the total skin impedance. R_d was fixed for the dry and hydrated phantom, as the novel porosity-based approach allows changes to the properties of the stratum corneum in a controlled way. The contact capacitance (C_c) for titanium on a hydrated phantom (420 nF cm^{-2}) was approximately 2 times higher than that on a dry phantom (267 nF cm^{-2}). This indicates that the hydrated skin phantom not only provided a lower stratum corneum impedance but also improved the contact impedance by two times as compared to the dry phantom. Further, it is worthwhile to mention that all the impedance graphs, irrespective of the dry electrode configurations being tested, have a consistent slope, indicating a similar transduction mechanism at the interface.

The fitted values of CPE_{sc}, CPE_c, α and β are provided in supplementary information in Tables S1 and S2. The value of α was 0.9, similar to the prior research works [49], [52], and indicated roughness of skin and non-linear distribution of time constants. The value of β in the range of 0.5-0.6 can be attributed to dissipative effect at the electrode-skin interface [17]. For ease of understanding, the values were converted and presented in terms of real capacitance in **Table 4.1** and **Table 4.2**. The error associated with every calculated fitted parameters was substantially smaller than the calculated value of components (Tables S1 and S2). Across the range of frequency, the model agrees with the acquired data within 10%

of the value. Both **Table 4.1** and **Table 4.2** indicate the chi-squared value ranging from 0.7 × 10^{-2} and 4.4 × 10^{-2} for the fitting of the parameters to the circuit model. The obtained goodness of fit values is of the same order of magnitude as that of previous research works that depicted a good agreement between the fitting and experimental data [6], [38].

4.4.3 Healthy Subject Testing

4.4.3.1 *In Vivo* Skin-Electrode Contact Impedance

In vivo impedance measurements captured across the thigh resulted in higher skin-electrode contact impedance for SS as compared to Ti (Figure 4.8). The impedance spectrum was obtained from 0.1 Hz – 100 kHz, but for comparison normalized impedance at 10 Hz is shown in Figure 4.8. FDA guidelines suggest 10 Hz as the reference frequency to validate the performance of recording electrodes [38], [39]. The mean area-normalized electrode-skin impedance at 10 Hz for SS and Ti was 2.68 and 2.06 MΩ cm^2 respectively. SS resulted in a high variance in skin-electrode contact impedance, compared to Ti, although a paired t-test ($p=0.032$) indicated that the contact impedance for Ti is significantly lower than that of SS. Further, each of the five individuals above the median (blue line in Figure 4.8), were observed to have significantly lower impedance for Ti as compared to SS, whereas the impedance for the other five individuals below the median was found not to be significantly different.

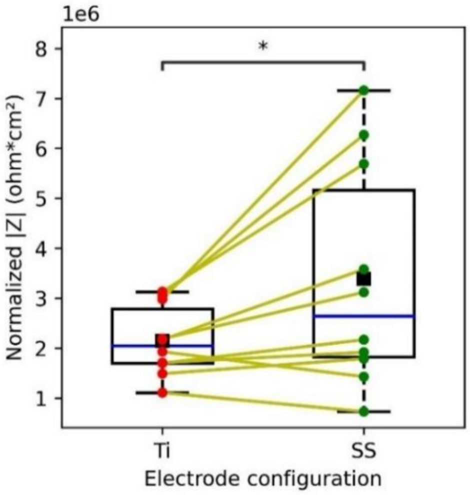

Figure 4.8. Box plot depicting the normalized skin-electrode contact impedance with respect to area, obtained with Ti and SS electrodes across ten human subjects. Data points corresponding to each subject across Ti (red dots) and SS (green dots) are connected with lines (yellow). Blue line shows the median and black square depicts the mean. The normalized skin-electrode contact impedance shown here is experimentally obtained from the impedance spectrum at 10 Hz, which depicts the combination of R_{sc}, C_{sc}, and C_c.

4.4.3.2 ECG Demonstration

Figure 4.9 shows an example of ECG segments captured across one subject with different electrode configurations and their corresponding SNR. Both Ti 6 cm^2 alcohol swabs (AS), shown in black, and SS 6 cm^2 alcohol swabs (AS), shown in red, depicted high SNR of 15 dB and 13 dB respectively. Ti 90 cm^2, shown in blue, resulted in higher SNR as compared to SS-90 cm^2, shown in green. Both Ti-6 cm^2, shown in yellow, and SS-6 cm^2, shown in cyan, exhibited lower SNR in comparison to larger area electrodes. Noise was significantly visible in the smaller area electrode configurations.

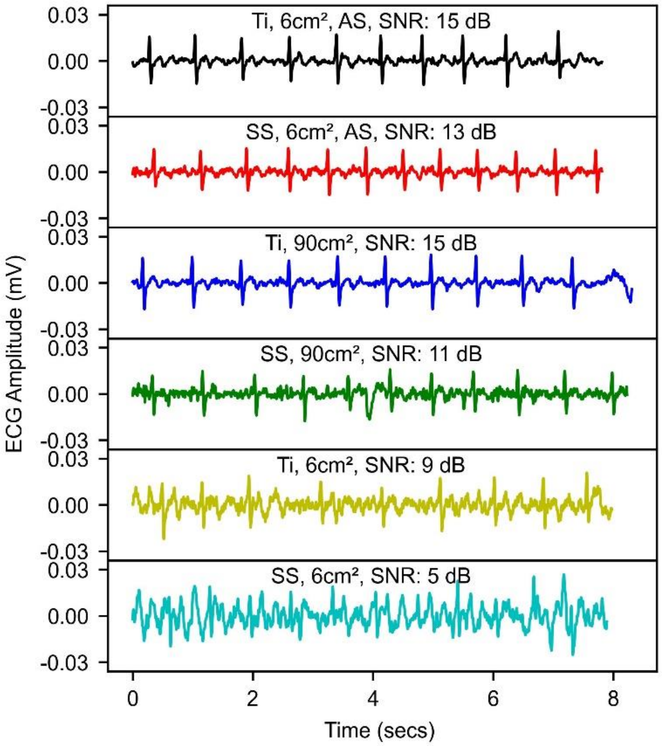

Figure 4.9. Example of the different ECG waveforms across one subject (only 8 secs shown, 90-sec recordings were made) using different electrode configurations, along with their computed SNR.

SNR computed for different electrode configurations across 10 subjects was significantly different for SS 90 cm^2 and Ti 90 cm^2 electrodes with a value of 0.011 ($p<0.05$, Figure 4.10a). Higher SNR obtained for Ti 90 cm^2 to that of SS 90 cm^2 indicates better performance of Ti for the ECG acquisition. Data points corresponding to each subject are represented by a different shape and color and the box plot shows the entire distribution with a blue line indicating the median and whiskers describing entire the range of values. For alcohol swabs placed on SS and Ti, SNR was observed not to be significantly different, indicating the contribution of alcohol swabs towards capacitive coupling more than that of electrode material. For both SS and Ti 6 cm^2 electrodes, analyzable ECG could not be obtained for 7 subjects, hence SNR was assigned zero as depicted in Figure 4.10a. This indicates the smaller area electrodes were not sufficient for capturing ECG signals across seven out of ten subjects. For the three subjects, a similar trend from a material perspective was observed, where Ti resulted in higher SNR as compared to SS electrodes.

Kurtosis resulted in higher values for Ti 90 cm^2 as compared to SS 90 cm^2, thus indicating the dominance of QRS peaks in Ti as compared to SS (Figure 4.10b). Kurtosis for alcohol swabs on SS and Ti was not significantly different. Kurtosis for Ti 6 cm^2 and SS 6 cm^2 was lower than that of other electrode configurations. Moreover, the data points corresponding to the subjects whose PSDR was higher than 0.8 and assigned an SNR of zero, resulted in extremely low and negative kurtosis, which indicated the lack of QRS complex. Further, the evaluation of the contribution of signal and noise components to SNR revealed that the noise obtained with SS (90 cm^2) and Ti (90 cm^2) electrodes was significantly different, however, the signal was not significantly different (Figure 4.11). This indicates that the contribution of the area was large enough to lower the skin-electrode impedance, and capture the ECG signal for both SS and Ti. However, low-frequency noise integrated into the 1 Hz - 40 Hz frequency band was higher for SS as compared to Ti. This is because contact impedance was higher for SS, thus increasing the noise level. This is in agreement with the findings of Kappenman et al., that high-electrode impedance may not contribute to the attenuation of the signal, but may increase the noise level [40].

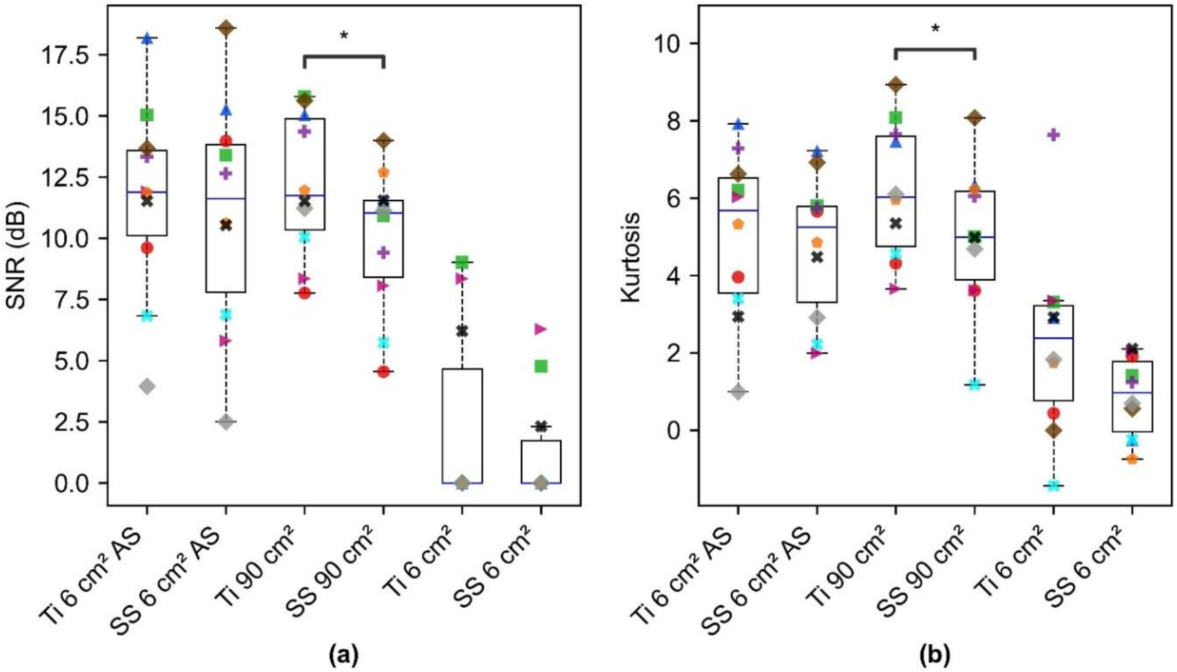

Figure 4.10. Computed ECG signal quality metric depicting the (a) SNR and (b) Kurtosis across different electrode configurations (material and area). Ti 6 cm^2 AS and SS 6 cm^2 AS denote the gold standard measurements, obtained with alcohol swabs placed directly on the electrodes to come into contact with the skin. Box plots show the entire distribution, data points corresponding to each subject are represented by a different shape and color. (*) denotes the statistical significance of $p < 0.05$, obtained with paired t-test and was significant for Ti 90 cm^2 and SS 90 cm^2. Paired t-test conducted for (Ti 6 cm^2 AS, SS 6 cm^2 AS); (Ti 6 cm^2, SS 6 cm^2); (Ti 6 cm^2 AS, Ti 90cm^2); (SS 6 cm^2 AS, SS 90 cm^2) was not significant.

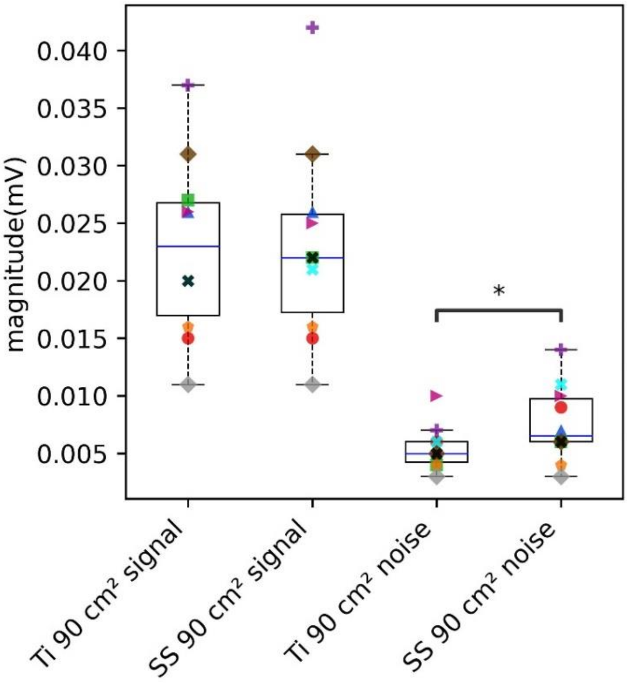

Figure 4.11. Evaluation of the contribution of signal and noise components across large areas of SS and Ti electrode configurations. Box plots show the entire distribution; the datapoint corresponding to each subject is represented by a different shape and color. (*) denotes the statistical significance of $p < 0.05$, obtained with paired t-test.

4.5 Discussion

In this work, a simple mechanistic circuit model has been proposed to isolate and understand the role of the electrode area, material of a dry electrode on dry and hydrated skin, while isolating the influence of each variable independently. Similar to prior work [41], an analogous RC circuit model was used to simulate the electrical model of the skin. Our method of using empirical data to determine parameter values showed the effect of area, which resulted in a lower skin-electrode contact impedance with an increase in the area, which corresponds to prior work [12], [37]and theoretical predictions, giving us confidence in the method. Thus, this method was used to investigate the interface properties using the controlled skin properties via a phantom. **Table 4.2** provides the individual contribution of contact impedance and stratum corneum in the capacitive coupling mechanism. Because contact impedance comprises native oxide, the electrical and dielectric properties of the native oxides were investigated. The Auger peaks (Figure 4.6a) obtained for SS at 711 eV showed that (Fe_2O_3) dominated the composition of SS as the native oxide. The peak at 420 eV (Figure 4.6b) revealed that the oxide composition for Ti was comprised mainly of titanium oxide (TiO_2). Therefore, the thickness, conductivity, and relative permittivity of the native oxide layers were investigated. The native oxide thickness of titanium and stainless steel was found to be a few nanometers thick, 3 nm for that of Ti [42] and 5 nm for SS [43]. Boxley et al. showed the conductivity of TiO_2 to vary between 10^{-3} to 10 Sm^{-1} [42]. This is similar in order of magnitude to that of conductivity of Fe_2O_3 to ~1.3×10^{-3} Sm^{-1} [44]. The relative permittivity of titanium native oxide was found to be 4 times higher for Ti native oxide (TiO_2, $\varepsilon_r = 60$) [45], than that of SS native oxide ($\varepsilon_r = 15.6$) [46]. The fitted curve and the computed contact capacitance (C_c), reveal that the Ti shows enhanced capacitive behavior (× 2.3 times) as compared to SS (**Table 4.2**), therefore lower contact impedance (equation 2). Thus, this can be attributed to the higher relative permittivity of Ti native oxide to that of SS native oxide coming in contact with the skin. Moreover, there have been attempts made by researchers to use aluminum as a metal-based dry electrode for recording biopotential signals, and poor performance has been reported for aluminum [47], [48]. On looking into the relative permittivity of the native oxide for aluminum (ε_r ~9) [46], it suggests a poor performance compared to that of SS and Ti. This further validates the mechanism of capacitive coupling for metal-based dry electrodes.

Stratum corneum properties play a significant role in the capacitive coupling transfer mechanism [49], [50]. The fitted parameters for stratum corneum (R_{sc}, C_{sc}) on a dry phantom (**Table 4.2**), were found to be of the same order of magnitude similar to that of literature, where resistance per unit area is of the order of 10^5 **Ω** cm^2 (ranging between 0.1-5000 kΩ cm^2) and capacitance per unit area is of the order of 30 nF cm^{-2} [51]. Interestingly, we observed that for the hydrated phantom, C_{sc} increased by 4.5 times, as compared to a dry phantom (**Table 4.2**). This can be attributed to the fact that the dielectric properties of the stratum corneum are significantly affected by hydration. S. Björklund et al. showed that the relative permittivity of dry stratum corneum is 10 and that of hydrated SC is 49 [52]. **Table 4.2** indicates that C_c was approximately 2 times more for the hydrated phantom than for a dry phantom. This can be attributed to the improved contact, as in a hydrated state due to higher porosity, saline solution is filling the air gap and acting as the junction liquid (ε_r = 80), thus the effective contact capacitance is improved between the electrode and stratum corneum. Thus, for the hydrated state, the changes in skin-electrode contact impedance due to hydration were significant as compared to the electrode material.

Since hydration is the most significant factor in contributing toward a lower skin-electrode impedance, nowadays, progress is made in the field of semi-dry electrodes [53]. The presence of a low amount of electrolyte as a liquid rather than conductive gel overcomes the limitations of the wet electrodes such as the need for skin preparation/abrasion of the skin and drying out of the gel [54]. The discharge of a small amount of electrolyte can achieve a local skin hydration effect, which results in a lower skin-electrode impedance [55]. Such type of semi-dry technology has great potential especially in recording high-density electroencephalography (EEG) signals. For recording EEG signals with the typically used semi-dry electrodes, electrode material might not play a substantial role as hydration is the most significant factor in achieving a low skin-electrode impedance. However, for recording ECG signals, in some applications such as smart watches (Apple watch), hand-held monitors (AliveCor Kardia Mobile), and toilet seat-based cardiovascular monitoring system (Casana), the electrodes used are completely dry because adding the electrolyte prior to each measurement is not practical. Thus, investigation in this work was carried out to study the role of electrode material in lowering the electrode-skin impedance in the absence of added electrolyte.

Our results depicted higher SNR with Ti as compared to SS (Figure 4.10A), which is in agreement with the findings of Meziane et al. [14]. However, Meziane et al. demonstrated the better performance of Ti as compared to SS only through the empirical biopotential signal acquisition across human subjects. In our work, we further investigated the skin-electrode contact impedance both on a phantom and human skin along with ECG acquisition. For both the phantom and human skin, contact impedance was found to be lower for titanium than SS (Figure 4.7c and Figure 4.8). This is in agreement with Searle et al. where lower contact impedance against time was observed for Ti as compared to SS, however was not significant when compared across 5 subjects [56]. In our work, we noticed that the skin-electrode contact impedance was not very different for subjects below the median line (Figure 4.8). Based on this, the data was divided into two subpopulations (dry and hydrated) and the correlation with SNR corresponding to the ECG signal was investigated. Both skin-electrode contact impedance (Figure 4.12a) and SNR (Figure 4.12b) obtained with different materials were significantly different for dry skin and not for hydrated skin individuals. This indicates that the material plays a significant role for the dry skin individuals, rather than people with hydrated skin. Also, dry skin people with higher skin impedance are more sensitive to noise pickup. Thus, the higher relative permittivity of TiO_2 indicates a lower capacitive impedance in comparison to SS native oxide. These results suggest that the relative permittivity at the interface of skin and the metal plays a significant role in the enhancement of the capacitive coupling phenomenon. Moreover, it was evident that for individuals characterized as having hydrated skin, an analyzable ECG signal was even detected with the small area (6 cm^2) electrodes (Figure 4.10a), thus further indicating the presence of a lower skin-electrode contact impedance.

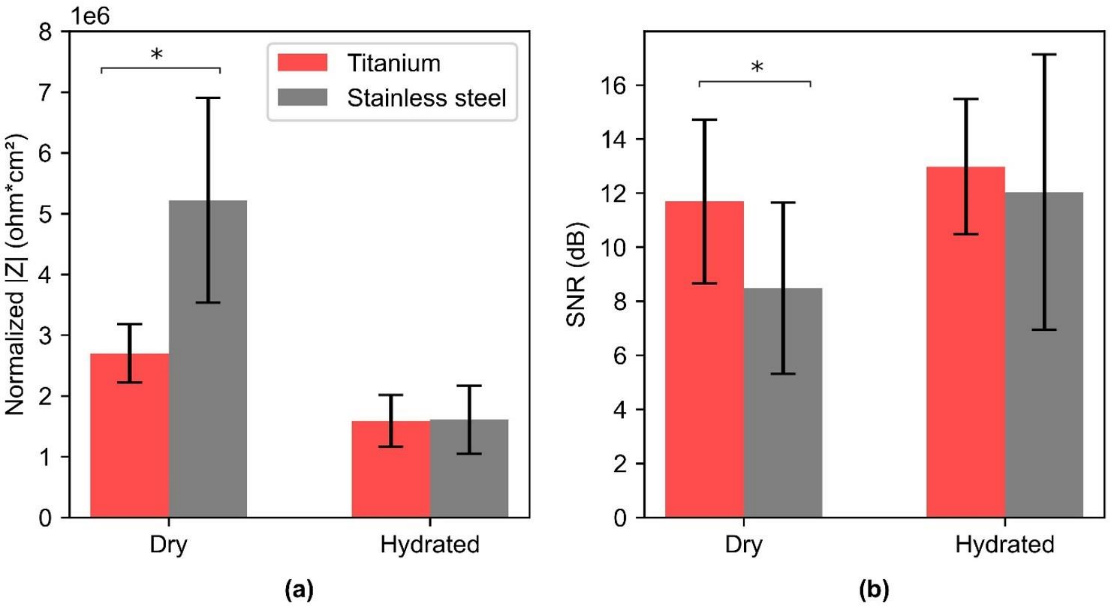

Figure 4.12. (a) Normalized Skin-Electrode contact impedance to the area at 10 Hz for dry (N=5) and hydrated skin (N=5) individuals with SS and Ti. (b) Obtained SNR for ECG across the dry and hydrated skin individuals with SS and Ti. (*) denotes the statistical significance of $p < 0.05$, obtained with paired t-test. Rectangular bars show the mean for the individuals that fall under dry and hydrated skin type, N= 5 for each category, and the height of the error bars denote the standard deviation.

One of the limitations of this study includes that unlike simultaneous ECG measurements performed in earlier work [14] to compare the wet and dry electrode performance, we compared the back-to-back ECG measurements, due to the measurement location. Secondly, an alcohol swab was placed on the electrode for capturing a high quality to compare signals and considered a gold standard. Excellent signal quality was observed with alcohol swabs, however, the mechanistic principle involved in the working of the alcohol swabs is very different from wet electrodes. We believe the mechanistic principle for the functioning of the alcohol swab is based upon improved capacitive coupling due to the increase in the effective area and the presence of higher relative permittivity between the skin and the metal electrode. Due to the skin's rough surface and the stiffness of the metal, the electrodes are not in complete contact with the skin; hence, by placing the alcohol swab between the skin and electrode, the air gaps are replaced by fluid, which leads to an increase in capacitive coupling (ε_r for air is 1 and that of alcohol swab made from 70% IPA is 35) [57]. Moreover, along with increased effective contact area and higher relative permittivity, it also moistens the skin, thus lowering the stratum corneum impedance. The proposed rationale is in complete agreement with previously reported results where the dry electrode was wetted with polyethylene glycol (ε_r ~10) and water (ε_r ~80) [58].

The findings of this work suggest that investigating dielectric properties, such as thickness, and relative permittivity of the native oxide, can be one of the approaches when selecting material for biopotential electrodes. Higher relative permittivity of the electrode material native oxide can lead to an enhancement in the capacitive coupling phenomenon and thus a lower skin-electrode impedance. An increase in electrode area can reduce skin-electrode impedance (Figure 4.7a), but for applications where the area is a limiting factor, such as watches, electrode material selection might help in achieving a lower electrode-skin impedance (Figure 4.7c). For applications such as a toilet seat cardiovascular monitoring system, an optimal combination of both area and material can help in achieving lower skin-electrode impedance and thus higher signal quality (Figure 4.10). Titanium has a potential to be used as an electrode material for achieving higher signal quality, which can be accounted to the higher relative permittivity of Ti native oxide. This work indicates that the approach of prioritizing the relative permittivity of the oxide layer in material selection has the potential to be used as a guide to material selection. Moreover, for dry skin individuals, Ti depicted a lower variance than SS (Figure 4.8), which indicates higher repeatability with Ti than with SS. This can be leveraged, as the properties of humans are variable, which leads to skin impedance changes over time. Thus, titanium-based metal electrodes as compared to SS can improve the reliability of in-home monitoring systems.

4.6 Conclusions

This work explores the role of electrode material and skin hydration in a controlled way on a phantom using a skin-electrode interface model. The model demonstrates the significance of electrode material in the mechanistic principle involved in the working of the dry electrode for biopotential signal acquisition. The developed model studies the contribution of each variable individually and can be used to provide insight into the development of future electrodes. The results of the model suggest the relative permittivity of the native oxide for the electrode material can provide an insight into the electrode performance for biopotential measurements. The ECG acquisition conducted across human subjects indicates titanium as a superior material for the acquisition of biopotential signals with less noise as compared to stainless steel, especially for dry skin individuals. Thus, titanium compared to stainless steel has the potential to improve dry electrode performance. This work provides insight into the transduction mechanism of the metal-based dry electrodes, and the significance of native oxide and skin dielectric properties in the electrode performance, which can help in the evaluation of other electrode materials.

References

[1] S. R. Steinhubl *et al.*, "Effect of a home-based wearable continuous ECG monitoring patch on detection of undiagnosed atrial fibrillation the mSToPS randomized clinical trial," *JAMA - J. Am. Med. Assoc.*, vol. 320, no. 2, pp. 146–155, 2018, doi: 10.1001/jama.2018.8102.

[2] M. A. Serhani, H. T. El Kassabi, H. Ismail, and A. N. Navaz, "ECG monitoring systems: Review, architecture, processes, and key challenges," *Sensors*, vol. 20, no. 6, 2020, doi: 10.3390/s20061796.

[3] L. A. Geddes, "Historical evolution of circuit models for the electrode-electrolyte interface," *Ann. Biomed. Eng.*, vol. 25, no. 1, pp. 1–14, 1997, doi: 10.1007/BF02738534.

[4] Y. H. Chen *et al.*, "Soft, comfortable polymer dry electrodes for high quality ECG and EEG recording," *Sensors (Switzerland)*, vol. 14, no. 12, pp. 23758–23780, 2014, doi: 10.3390/s141223758.

[5] E. Huigen, A. Peper, and C. A. Grimbergen, "Investigation into the origin of the noise of surface electrodes," *Med. Biol. Eng. Comput.*, vol. 40, no. 3, pp. 332–338, 2002, doi: 10.1007/BF02344216.

[6] B. B. Murphy, B. H. Scheid, Q. Hendricks, N. V. Apollo, B. Litt, and F. Vitale, "Time evolution of the skin–electrode interface impedance under different skin treatments," *Sensors*, vol. 21, no. 15, pp. 1–14, 2021, doi: 10.3390/s21155210.

[7] S. M. Lobodzinski, "ECG Instrumentation: Application and Design," in *Macfarlane, P.W., van Oosterom, A., Pahlm, O., Kligfield, P., Janse, M., Camm, J. (eds) Comprehensive Electrocardiology*, Springer, London, 2010, pp. 427–480. doi: 10.1007/978-1-84882-046-3_12.

[8] L. A. Geddes and L. E. Baker, *Principles of Applied Biomedical Instrumentation*. 3rd ed. New York, John Wiley & Sons, 1989. doi: 10.1213/00000539-199005000-00027.

[9] U. Birgersson, E. Birgersson, P. Åberg, I. Nicander, and S. Ollmar, “Non-invasive bioimpedance of intact skin: Mathematical modeling and experiments,” *Physiol. Meas.*, vol. 32, no. 1, pp. 1–18, 2011, doi: 10.1088/0967-3334/32/1/001.

[10] R. N. Schmidt, F. J. Lisy, G. G. Skebe, and T. S. Prince, “Dry Physiological Recording Electrode,” U.S. Patent 6,785,569, 2004.

[11] A. Albulbul, “Evaluating major electrode types for idle biological signal measurements for modern medical technology,” *Bioengineering*, vol. 3, no. 3, 2016, doi: 10.3390/bioengineering3030020.

[12] A. A. Chlaihawi, B. B. Narakathu, S. Emamian, B. J. Bazuin, and M. Z. Atashbar, “Development of printed and flexible dry ECG electrodes,” *Sens. Bio-Sensing Res.*, vol. 20, pp. 9–15, 2018, doi: 10.1016/j.sbsr.2018.05.001.

[13] X. An, O. Tangsirinaruenart, and G. K. Stylios, “Investigating the performance of dry textile electrodes for wearable end-uses,” *J. Text. Inst.*, vol. 110, no. 1, pp. 151–158, 2019, doi: 10.1080/00405000.2018.1508799.

[14] N. Meziane, S. Yang, M. Shokoueinejad, J. G. Webster, M. Attari, and H. Eren, “Simultaneous comparison of 1 gel with 4 dry electrode types for electrocardiography,” *Physiol. Meas.*, vol. 36, no. 3, pp. 513–529, 2015, doi: 10.1088/0967-3334/36/3/513.

[15] A. S. Anusha, S. P. Preejith, T. J. Akl, J. Joseph, and M. Sivaprakasam, “Dry Electrode Optimization for Wrist-based Electrodermal Activity Monitoring,” *MeMeA 2018 - 2018 IEEE Int. Symp. Med. Meas. Appl. Proc.*, pp. 1–6, 2018, doi: 10.1109/MeMeA.2018.8438595.

[16] S. Peng, K. Xu, and W. Chen, “Comparison of active electrode materials for non-contact ECG measurement,” *Sensors*, vol. 19, no. 16, pp. 1–18, 2019, doi: 10.3390/s19163585.

[17] G. Li, S. Wang, and Y. Y. Duan, “Towards conductive-gel-free electrodes: Understanding the wet electrode, semi-dry electrode and dry electrode-skin interface impedance using electrochemical impedance spectroscopy fitting,” *Sensors Actuators B: Chem.*, vol. 277, pp. 250–260, 2018, doi: 10.1016/j.snb.2018.08.155.

[18] N. J. Conn, K. Q. Schwarz, and D. A. Borkholder, “Nontraditional electrocardiogram and algorithms for inconspicuous in-home monitoring: Comparative study,” *JMIR mHealth uHealth*, vol. 6, no. 5, 2018, doi: 10.2196/mhealth.9604.

[19] K. Goyal, D. A. Borkholder, and S. W. Day, “A biomimetic skin phantom for characterizing wearable electrodes in the low-frequency regime,” *Sensors Actuators A: Phys.*, vol. 340, p. 113513, 2022, doi: 10.1016/j.sna.2022.113513.

[20] R. I. Revilla, B. Wouters, F. Andreatta, A. Lanzutti, L. Fedrizzi, and I. De Graeve, “EIS comparative study and critical Equivalent Electrical Circuit (EEC) analysis of the native oxide layer of additive manufactured and wrought 316L stainless steel,”

Corros. Sci., vol. 167, p. 108480, 2020, doi: 10.1016/j.corsci.2020.108480.

[21] H. E. Bishop, J. C. Rivière, and J. P. Coad, "Auger spectroscopy of titanium," *Surf. Sci.*, vol. 24, no. 1, pp. 1–17, 1971, doi: 10.1016/0039-6028(71)90217-2.

[22] B. Taji, A. D. C. Chan, and S. Shirmohammadi, "Effect of Pressure on Skin-Electrode Impedance in Wearable Biomedical Measurement Devices," *IEEE Trans. Instrum. Meas.*, vol. 67, no. 8, pp. 1900–1912, 2018, doi: 10.1109/TIM.2018.2806950.

[23] C. H. Hsu and F. Mansfeld, "Concerning the conversion of the constant phase element parameter Y0 into a capacitance," *Corrosion*, vol. 57, no. 9, pp. 747–748, 2001, doi: 10.5006/1.3280607.

[24] W. G. Cochran, "The X2 Test of Goodness of Fit," *Ann. Math. Stat.*, vol. 23, no. 3, pp. 315–345, 1952, doi: 10.1214/aoms/1177729380.

[25] "Equivalent Circuit Modeling Using the Gamry Electrochemical Impedance Spectroscopy Software." https://www.gamry.com/application-notes/EIS/equivalent-circuit-modeling-using-the-gamry-eis300-electrochemical-impedance-spectroscopy-software/ (accessed Sep. 06, 2022).

[26] D. Ricciardi *et al.*, "Impact of the high-frequency cutoff of bandpass filtering on ECG quality and clinical interpretation: A comparison between 40 Hz and 150 Hz cutoff in a surgical preoperative adult outpatient population," *J. Electrocardiol.*, vol. 49, no. 5, pp. 691–695, 2016, doi: 10.1016/j.jelectrocard.2016.07.002.

[27] N. V. Thakor, J. G. Webster, and W. J. Tompkins, "Optimal QRS detector," *Med. Biol. Eng. Comput.*, vol. 21, no. 3, pp. 343–350, 1983, doi: 10.1007/BF02478504.

[28] Q. Li, R. G. Mark, and G. D. Clifford, "Robust heart rate estimation from multiple asynchronous noisy sources using signal quality indices and a Kalman filter," *Physiol. Meas.*, vol. 29, no. 1, pp. 15–32, 2008, doi: 10.1088/0967-3334/29/1/002.

[29] I. D. Castro, C. Varon, T. Torfs, S. van Huffel, R. Puers, and C. van Hoof, "Evaluation of a multichannel non-contact ECG system and signal quality algorithms for sleep apnea detection and monitoring," *Sensors*, vol. 18, no. 2, pp. 1–20, 2018, doi: 10.3390/s18020577.

[30] P. D. Welch, "The Use of Fast Fourier Transform for the Estimation of Power Spectra: A Method Based on Time Averaging Over Short, Modified Periodograms," *IEEE Trans. Audio Electroacoust.*, vol. 15, no. 2, pp. 70–73, 1967, doi: 10.1109/TAU.1967.1161901.

[31] D. Makowski *et al.*, "NeuroKit2: A Python toolbox for neurophysiological signal processing," *Behav. Res. Methods*, vol. 53, no. 4, pp. 1689–1696, 2021, doi: 10.3758/s13428-020-01516-y.

[32] W. Pei *et al.*, "Skin-Potential Variation Insensitive Dry Electrodes for ECG Recording," *IEEE Trans. Biomed. Eng.*, vol. 64, no. 2, pp. 463–470, 2017, doi: 10.1109/TBME.2016.2562702.

[33] T. He, G. Clifford, and L. Tarassenko, "Application of independent component analysis in removing artefacts from the electrocardiogram," *Neural Comput. Appl.*, vol. 15, no. 2, pp. 105–116, 2006, doi: 10.1007/s00521-005-0013-y.

[34] M. Helmenstine, "Table of Electrical Resistivity and Conductivity," 2019. https://www.thoughtco.com/table-of-electrical-resistivity-conductivity-608499 (accessed Sep. 06, 2022).

[35] J. C. Langevoort, I. Sutherland, L. J. Hanekamp, and P. J. Gellings, "On the oxide formation on stainless steels AISI 304 and incoloy 800H investigated with XPS," *Appl. Surf. Sci.*, vol. 28, no. 2, pp. 167–179, 1987, doi: 10.1016/0169-4332(87)90062-6.

[36] J. Lausmaa, "Surface spectroscopic characterization of titanium implant materials," *J. Electron Spectros. Relat. Phenomena*, vol. 81, no. 3, pp. 343–361, 1996, doi: 10.1016/0368-2048(95)02530-8.

[37] G. Li, S. Wang, and Y. Y. Duan, "Towards gel-free electrodes: A systematic study of electrode-skin impedance," *Sensors Actuators B: Chem.*, vol. 241, pp. 1244–1255, 2017, doi: 10.1016/j.snb.2016.10.005.

[38] B. B. Murphy *et al.*, "A Gel-Free Ti3C2Tx-Based Electrode Array for High-Density, High-Resolution Surface Electromyography," *Adv. Mater. Technol.*, vol. 5, no. 8, pp. 1–10, 2020, doi: 10.1002/admt.202000325.

[39] FDA-2019-D-1649, "Purposes – Performance Criteria for Cutaneous Electrodes for Recording Safety and Performance Based Pathway," 2019.

[40] E. S. Kappenman and S. J. Luck, "The effects of electrode impedance on data quality and statistical significance in ERP recordings," *Psychophysiology*, vol. 47, no. 5, pp. 888–904, 2010, doi: 10.1111/j.1469-8986.2010.01009.x.

[41] Y. M. Chi, T. P. Jung, and G. Cauwenberghs, "Dry-contact and noncontact biopotential electrodes: Methodological review," *IEEE Rev. Biomed. Eng.*, vol. 3, pp. 106–119, 2010, doi: 10.1109/RBME.2010.2084078.

[42] C. J. Boxley, H. S. White, C. E. Gardner, and J. V. Macpherson, "Nanoscale Imaging of the Electronic Conductivity of the Native Oxide Film on Titanium Using Conducting Atomic Force Microscopy," *J. Phys. Chem. B*, vol. 107, no. 36, pp. 9677–9680, 2003, doi: 10.1021/jp034874u.

[43] A. Rosenkranz *et al.*, "Oxide Formation, Morphology, and Nanohardness of Laser-Patterned Steel Surfaces," *Adv. Eng. Mater.*, vol. 17, no. 8, pp. 1234–1242, 2015, doi: 10.1002/adem.201400487.

[44] C. A. Balanis, *Advanced Engineerig Electromagnetics*. John Wiley & Sons, 2012.

[45] J. Löberg, J. Perez Holmberg, I. Mattisson, A. Arvidsson, and E. Ahlberg, "Electronic properties of TiO2 nanoparticles films and the effect on apatite-forming ability," *Int. J. Dent.*, vol. 2013, 2013, doi: 10.1155/2013/139615.

[46] Y. Qiu, S. Thomas, R. K. Gupta, T. Gengenbach, R. Jones, and N. Birbilis, “A surface study of the native oxide upon a compositionally complex alloy,” *Corrosion*, vol. 74, no. 12, pp. 1312–1317, 2018, doi: 10.5006/2967.

[47] G. E. Bergey, R. D. Squires, and W. C. Sipple, “Electrocardiogram Recording with Pasteless Electrodes,” *IEEE Trans. Biomed. Eng.*, vol. BME-18, no. 3, pp. 206–211, 1971, doi: 10.1109/TBME.1971.4502833.

[48] C. Lopes *et al.*, “Me-doped Ti–me intermetallic thin films used for dry biopotential electrodes: A comparative case study,” *Sensors*, vol. 21, no. 23, 2021, doi: 10.3390/s21238143.

[49] L. M. Ferrari, U. Ismailov, F. Greco, and E. Ismailova, “Capacitive Coupling of Conducting Polymer Tattoo Electrodes with the Skin,” *Adv. Mater. Interfaces*, vol. 8, no. 15, pp. 1–8, 2021, doi: 10.1002/admi.202100352.

[50] L. M. Ferrari, U. Ismailov, J. M. Badier, F. Greco, and E. Ismailova, “Conducting polymer tattoo electrodes in clinical electro- and magneto-encephalography,” *npj Flex. Electron.*, vol. 4, no. 1, pp. 1–9, 2020, doi: 10.1038/s41528-020-0067-z.

[51] J. Heikenfeld *et al.*, “Wearable sensors: Modalities, challenges, and prospects,” *Lab on a Chip*, vol. 18, no. 2, pp. 217–248, 2018, doi: 10.1039/c7lc00914c.

[52] S. Björklund *et al.*, “Skin membrane electrical impedance properties under the influence of a varying water gradient,” *Biophys. J.*, vol. 104, no. 12, pp. 2639–2650, 2013, doi: 10.1016/j.bpj.2013.05.008.

[53] G. L. Li, J. T. Wu, Y. H. Xia, Q. G. He, and H. G. Jin, “Review of semi-dry electrodes for EEG recording,” *J. Neural Eng.*, vol. 17, no. 5, 2020, doi: 10.1088/1741-2552/abbd50.

[54] J. Liu *et al.*, “Ten-Hour Stable Noninvasive Brain-Computer Interface Realized by Semidry Hydrogel-Based Electrodes,” *Research*, vol. 2022, pp. 1–12, 2022, doi: 10.34133/2022/9830457.

[55] G. Li, S. Wang, M. Li, and Y. Y. Duan, “Towards real-life EEG applications: Novel superporous hydrogel-based semi-dry EEG electrodes enabling automatically ‘charge-discharge’ electrolyte,” *J. Neural Eng.*, vol. 18, no. 4, 2021, doi: 10.1088/1741-2552/abeeab.

[56] A. Searle and L. Kirkup, “A direct comparison of wet, dry and insulating bioelectric recording electrodes,” *Physiol. Meas.*, vol. 21, no. 2, pp. 271–283, 2000, doi: 10.1088/0967-3334/21/2/307.

[57] J.-G. Park, S.-H. Lee, J.-S. Ryu, Y.-K. Hong, T.-G. Kim, and A. A. Busnaina, “Interfacial and Electrokinetic Characterization of IPA Solutions Related to Semiconductor Wafer Drying and Cleaning,” *J. Electrochem. Soc.*, vol. 153, no. 9, p. G811, 2006, doi: 10.1149/1.2214532.

[58] Y. Yamamoto and T. Yamamoto, “Characteristics of skin admittance for dry

electrodes and the measurement of skin moisturisation," *Med. Biol. Eng. Comput.*, vol. 24, no. 1, pp. 71–77, 1986, doi: 10.1007/BF02441608.

Appendix B

Table B1. Impedance model fitting parameters obtained for impedance response across SS electrodes of 4 cm2 and 9 cm2 area electrodes on a dry phantom. Rd and Rsc represent the resistance of the deeper tissue layer and stratum corneum respectively. Constant phase element CPEsc and exponent α represent stratum corneum capacitance and CPEc and exponent β represent contact capacitance. Values in the Table are shown as computed ± error.

Electrode Area (SS and dry)	R_d (kΩ)	R_{sc} (MΩ)	CPE_{sc} (nSs^{α})	α	CPE_c (μSs^{β})	β
4 cm^2	1.77 ± 0.00	1.62 ± 0.00	182 ± 3.77	0.9 ± 0.005	1.02 ± 0.03	0.56 ± 0.003
9 cm2	1.75 ± 0.03	0.70 ± 0.04	500 ± 10.8	0.8 ± 0.011	2.02 ± 0.42	0.56 ± 0.010

Table B2. Impedance model fitting parameters obtained for impedance response across SS and Ti on a dry and hydrated phantom. Impedance normalized to the area is shown. Rd and Rsc represent the resistance of the deeper tissue layer and stratum corneum respectively. Constant phase element CPEsc and exponent α represent stratum corneum capacitance and CPEc and exponent β represent contact capacitance. Values in the Table are shown as computed ± error.

Electrode Material (Phantom Hydration status)	R_d ($k\Omega cm^2$)	R_{sc} ($M\Omega cm^2$)	CPE_{sc} ($nSs^{\alpha}cm^{-2}$)	α	CPE_c ($nSs^{\beta}cm^{-2}$)	β
Ti (dry)	9.3 ± 0.20	6.4 ± 0.36	47.7 ± 1.08	0.9 ± 0.01	424 ± 45.6	0.50 ± 0.012
SS (dry)	9.3 ± 0.00	6.4 ± 0.00	47.7 ± 0.00	0.9 ± 0.00	170 ± 2.75	0.56 ± 0.002
Ti (hydrated)	9.3 ± 0.00	3.0 ± 0.00	200 ± 0.00	0.9 ± 0.00	652 ± 11.1	0.52 ± 0.002
SS(hydrated)	9.3 ± 0.00	3.0 ± 0.00	200 ± 0.00	0.9 ± 0.00	327± 4.65	0.59 ± 0.002

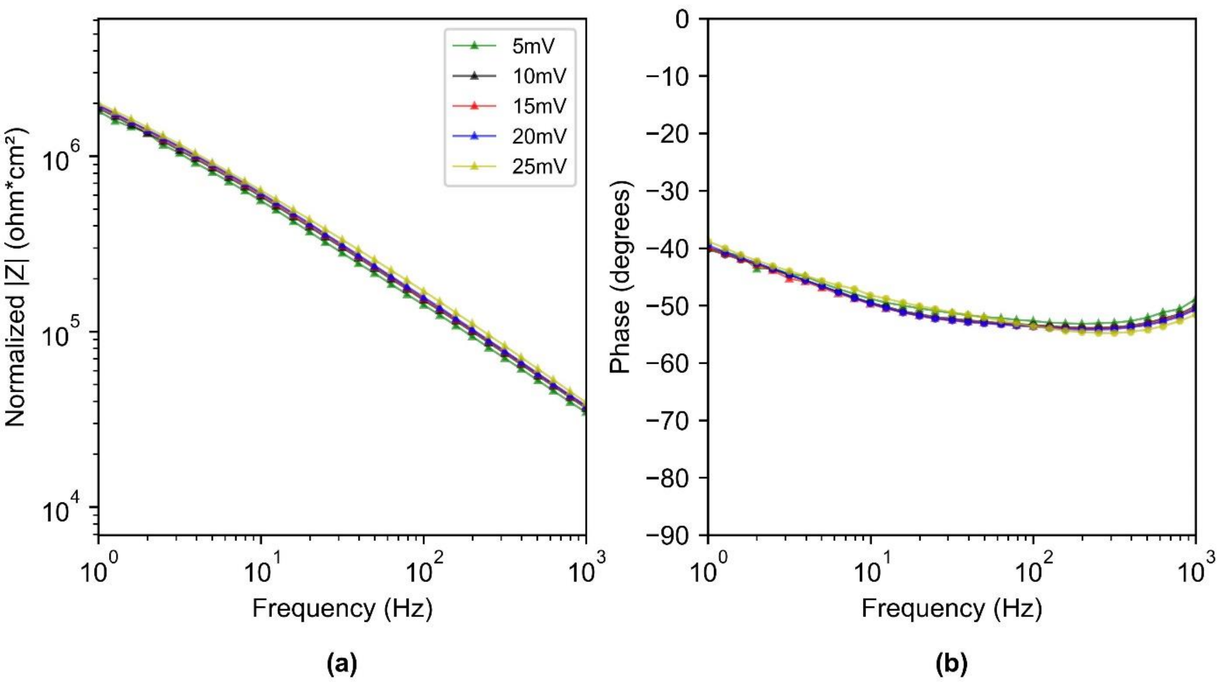

Figure B1. Bode plot depicting the a) normalized impedance magnitude with respect to area and b) phase for SS (9 cm2) on a hydrated phantom obtained with the excitation voltage of 5 mV, 10 mV, 15 mV, 20 mV and 25 mV.

B.1 Power Spectral Density Ratio

The ECG signal quality was evaluated using a metric power spectral density ratio (PSDR) defined in section 4.3.3.3. PSDR represents the relative power of the ECG signal in the QRS complex (5 Hz – 15 Hz), and was calculated as the ratio of power of the ECG signal between 5 Hz and 15 Hz to the power between 5 Hz and 40 Hz. PSDR resulted in values ranging from 0.4 to 1 for the ECG data captured in this work. A threshold of 0.8 was empirically determined to provide rejection of poor-quality signals. The empirically determined threshold value was consistent with the previously reported threshold value (0.8) by Li et al [28]. The ECG waveform and corresponding power spectral density curves for the ECG signals depicting PSDR of 0.55 (representing acceptable signal quality) and PSDR of 1 (representing unacceptable signal quality) are shown in Figure B2 and Figure B3 respectively.

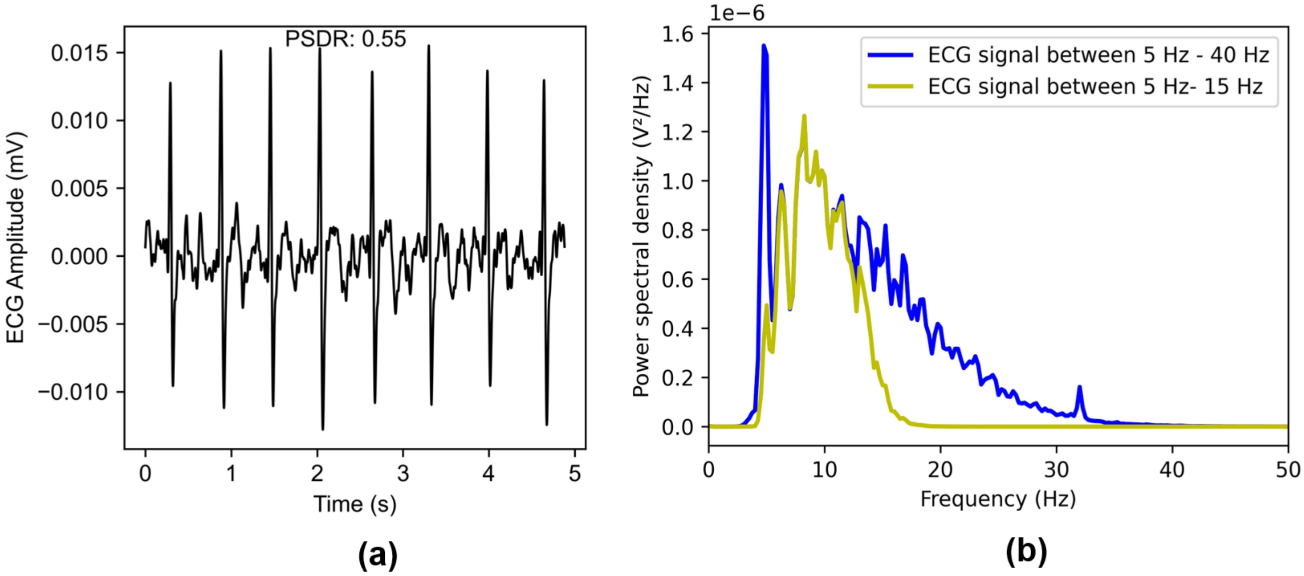

Figure B2. a) ECG signal, 5 secs is shown from 90 secs recording to clearly show the presence of QRS peaks b) Computed power spectral density curves based on the FFT of the ECG signal between 5 Hz - 15 Hz (shown in yellow) and ECG signal between 5 Hz – 40 Hz (shown in blue).

Upon visualization, QRS peaks were clearly visible in the ECG signal (Figure B2 a), and the ratio of the area under the QRS complex (shown in yellow) to that of the area under the ECG signal (shown in blue) resulted in a PSDR of 0.55, which was below the threshold value of 0.8 and thus considered as an analyzable signal.

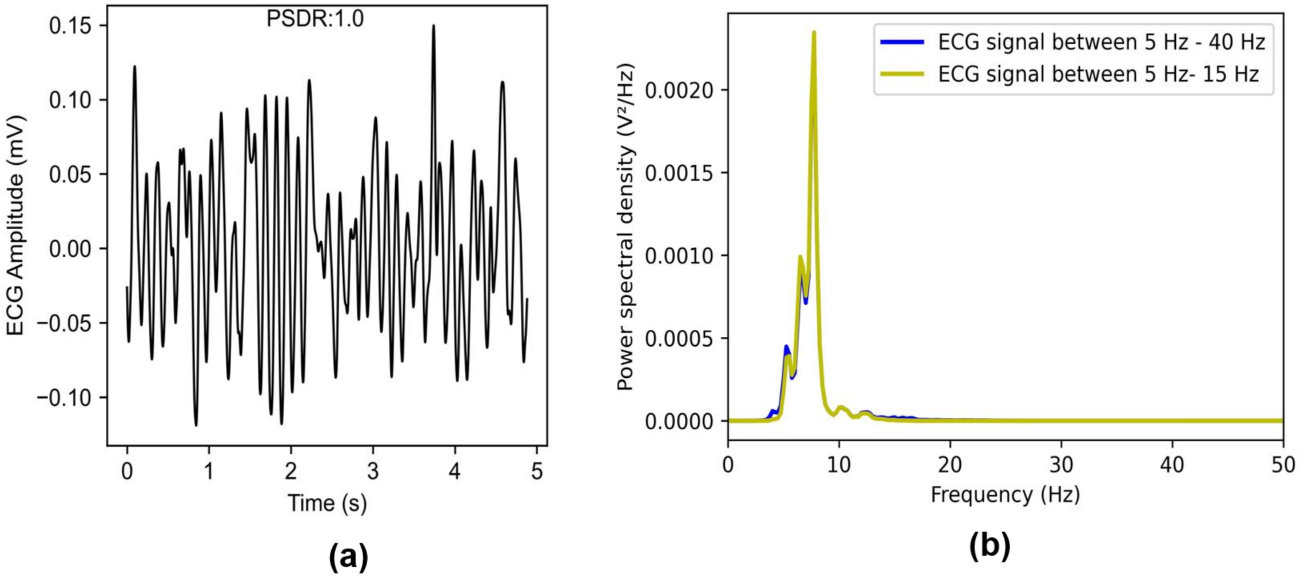

Figure B3. a) ECG signal, 5 secs is shown from 90 secs recording to clearly show the presence of large noisy spikes b) Computed power spectral density curves based on the FFT of the ECG signal between 5 Hz - 15 Hz (shown in yellow) and ECG signal between 5 Hz – 40 Hz (shown in blue). Both the power spectral density curves overlap and resulted in a PSDR of 1.

No QRS complexes were observed in the ECG signal (Figure B3 a). The power spectral density curve depicts the presence of large noisy spikes in the region 5 Hz – 15 Hz, therefore indicating QRS-like artifacts. Moreover, the power spectral density curves between 5 Hz- 15 Hz and 5 Hz – 40 Hz were found to overlap and area under the curves resulted in PSDR close to 1 (Figure B3 b). Based upon empirical observations and power spectral density curve, ECG signal resulting in a PSDR > 0.8 were considered as poor quality unanalyzable signals. PSDR of higher than 0.8 indicated noise in a frequency range similar to that of the QRS complex.

Chapter 5: In-Home Respiration Monitoring Using Thigh-Thigh Bioimpedance Measurements

Part of this chapter published as **K. Goyal**, D. A. Borkholder, and S. W. Day, “Unobtrusive In-Home Respiration Monitoring Using a Toilet Seat,” IEEE-EMBS International Conference on Biomedical and Health Informatics (BHI), pp. 01–05, 2022, doi: 10.1109/bhi56158.2022.9926931. None of the published chapter was modified and I have added the following sections to this chapter: 5.3.4, 5.3.6, 5.4.4, 5.4.6, last three paragraphs of 5.5.

5.1 Abstract

Non-invasive monitoring of pulmonary health could revolutionize the care of health conditions ranging from COVID-19 to asthma to heart failure, but current technologies face challenges that limit their feasibility and adoption. Here, we introduce a novel approach to monitor respiration by measuring changes in impedance from the back of the thigh. The integration of electrodes into a toilet seat ensures patient compliance with unobtrusive daily respiration monitoring benefitting from repeatable electrode placement on the skin. In this work, the feasibility of the thigh and the sensitivity of impedance to respiration have been investigated empirically by comparing thorax and thigh-thigh bioimpedance measurements to spirometer measurements, and computationally, using finite element modeling. Empirical results show a measurable peak-peak impedance (0.022 ohm to 0.290 ohm for normal breathing across 8 subjects) with respiration across thigh-thigh and a high correlation (0.85) between lung tidal volume and impedance change due to respiration. Thigh-thigh bioimpedance measurements were found to be able to distinguish between shallow, normal, and deep breathing. Further, day-to-day variability in the relationship between impedance and tidal volume was investigated. The results suggest that the novel approach can be used to detect respiration rate and tidal volume and could provide valuable insight into disease state for conditions ranging from COVID-19 to heart failure.

Keywords—Bioimpedance, Respiration monitoring, Dry electrodes, Toilet seat, Unobtrusive

5.2 Introduction

Remote respiratory monitoring facilitates the monitoring of pulmonary health of patients from their homes. Daily respiration monitoring may be useful for several conditions including COVID-19 recovery, and progression of edema during heart failure management. Some existing systems use impedance-based techniques to measure pulmonary health markers such as tidal volume, respiratory rate, and pulmonary congestion [1]. These devices non-invasively measure impedance of the thorax using wet electrodes attached to the chest (Figure 5.1a) based on the concept that the impedance across the chest changes as a function of both the volume (inflation) and material properties, such that it causes a decrease in conductance [2]. These methods show great promise and report a good correlation of breathing to impedance, higher than 0.9, but can be limited by poor repeatability of electrode placement, high and variable skin-electrode contact impedance. Moreover, discomfort caused by continuous wearing of electrodes under clothing limit the accuracy and practicality of tracking daily changes with these methods. To overcome the limitations of user inconvenience and poor repeatability of the conventional 4-electrode arrangement, recent efforts made by researchers for continuous respiration monitoring include devices such as a wearable patch [3], and a wearable vest [4], based upon the impedance technique. Other efforts include a non-contact optical approach to monitor respiration, using a volumetric surrogate corresponding to the chest wall movement captured by a smartphone camera [5]. However, all of the aforementioned devices are obtrusive.

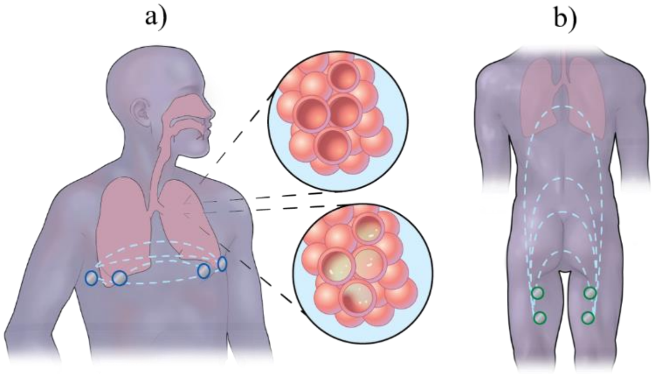

Figure 5.1. High-level overview: a) Bioimpedance measurements are conventionally performed across the thorax to determine pulmonary functioning and extract respiratory parameters of healthy and unhealthy lungs. b) A novel approach of respiration detection from a non-standard location, the back of the thigh, is presented, which can aid in-home physiological monitoring.

Here, we present the ability to measure respiration from back of the thigh (Figure 5.1b), by integrating dry electrodes into a toilet seat, as previously presented for heart function [6]. This implementation decreases electrode slippage, with natural and consistent applied pressure on the electrodes, repeatable electrode placement against the skin, and provides other benefits such as a large area of skin contact and compliance with patient routine. This provides a novel way for unobtrusive in-home respiration monitoring. The method lends itself to routine daily measurement, which is ideal for tracking conditions such as pulmonary edema and respiratory function due to viral infections [1].

Although the relationship of respiration to torso impedance is clear, the relationship between thigh-thigh impedance and respiration has not been investigated. To explore this, we employed a computational model using the finite element method. Finite element modeling (FEM) for bioimpedance simulations provides an efficient way to understand the sensitivity/specificity of impedance, and electrode positioning, in determining an optimal distance between the electrodes [7], [8]. Prior related work with numerical models involves human thorax organs simulated using simple geometric shapes, such as cylinders and spheres, to reduce the computational time [9], [10]. However, the conclusions can only be relied upon if the geometric configuration is anatomically correct. Some of the earlier attempts involved building a numerical model using the torso of the anatomically correct visible human project to study the conventional thoracic bioimpedance measurements [11]. Thus, there is a possibility to understand the system, with an anatomically correct CAD human model. In this work, to understand the sensitivity of impedance from the back of the thigh, FEM modeling has been carried out using COMSOL Multiphysics to perform bioimpedance simulations on a realistic CAD human model (Visible Human Project–Female from the National Library of Medicine).

The broad objective of this work is to evaluate the feasibility and understand the sensitivity of respiratory monitoring from the back of the thigh. In this work, the feasibility of this approach has been investigated empirically, by comparing thorax and thigh-thigh bioimpedance measurements to spirometer measurements, and computationally, using finite element modeling. We demonstrate the ability to measure changes in impedance associated with unhealthy conditions by measuring changes in impedance due to shallow breathing. Further, using the thigh-thigh impedance as a volume surrogate, the tidal volume has been computed. Lastly, we examine the day-to-day variability in the relationship between impedance and tidal volume.

5.3 Methods

5.3.1 Empirical Bioimpedance Measurements

Bioimpedance measurements were performed with a MAX30001 Analog Front-End (Maxim Integrated, USA) at a frequency of 80 kHz and 48µA, in a 4-electrode configuration from thigh-thigh using dry Titanium electrodes integrated into a toilet seat (Figure 5.2). The laptop used to connect the MAX30001 evaluation system was battery powered. The volumetric flow was measured simultaneous to a spirometer (MTL1000L, AD Instruments, USA). For comparison, bioimpedance measurements across the thorax were performed using wet electrodes, and again synchronized with the spirometer (Figure 5.2) and respiratory belts (Pneumotrace II) were placed at the thorax and abdomen to capture thoracic and abdomen movement. The experiments shown here were conducted on 8 subjects (28.0 ± 4.0 years; BMI: 24.3 ± 4.6) in a protocol approved by the Rochester Institute of Technology Institutional Review Board for Protection of Human Subjects.

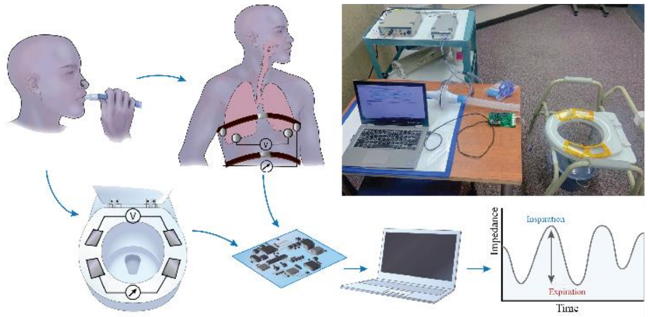

Figure 5.2. Experimental Setup: Simultaneous spirometer measurements for measuring tidal volume along with bioimpedance measurements. Bioimpedance measurements are performed across the thorax and thigh-thigh using a toilet seat platform. Impedance data is captured using MAX30001 Analog Front End.

Anatomical information, such as waist and thigh circumference, thigh length, and length from buttocks to sternal notch, were measured. Each subject was given a single-use disposable respiratory kit consisting of a respiratory filter, mouthpiece, and a nose clip. Subjects were asked to perform three different sequences of respiratory tasks: A (normal breathing for 2 mins); B (normal breathing for 30 secs / followed by 4 cycles of maximal inhale – maximal exhale / followed by 30 secs of normal breathing); C (normal breathing for 30 secs / followed by 4 cycles of maximal inhale – breath-hold – maximal exhale – breath-hold / followed by 30 secs of normal breathing).

The spirometer flow signal was integrated to obtain lung volume. The spirometer volume signal was acquired at a sampling rate of 1000 Hz and the raw impedance signal was acquired at 64 Hz. Both the volume and impedance signals were resampled to 100 Hz using polyphase filtering to obtain uniformity. Three seconds of data were removed from the beginning and the end for both as the impedance recording takes a few secs to settle and scale and polynomial detrending of both signals was performed to remove the baseline drift. The smoothing of the impedance signals was performed using a Savitzky-Golay filter with a window length of 2000 msec and third-order fitting. The processed impedance and spirometer volume signal were aligned using cross-correlation. We used NeuroKit2 [12], a Python-based physiological processing kit, to identify peaks (corresponding to maximum lung volume at the onset of exhalation) and troughs (minimum lung volume at the onset of inhalation) and measure peak-peak amplitude. For sequence A, which comprised normal breathing, peak-peak impedances corresponding to each respiratory cycle in a 2 min recording were averaged for each subject. Inter-subject means and variability are expressed as (Mean ± SD) throughout.

5.3.2 Calibration and Tidal Volume Estimation

For the study conducted across 8 subjects, a subject-specific calibration was performed, using sequence B for calibration as it incorporated a large range of tidal volumes. The spirometer was calibrated with a 3L syringe (Hans Rudolph, Inc., USA) for each subject. The peak-peak value computed from the spirometer volume signal serves as ground-truth tidal volume and the peak-peak amplitudes were mapped for both the spirometer volume signal and impedance signal. Using least squares linear regression with y-intercept forced to zero, a subject-specific calibration curve was computed. The calibration curve was used to estimate the tidal volume for sequence A and the estimated tidal volume was compared with the corresponding ground-truth tidal volume measured using a spirometer as a validation. The measure of the quality of the estimated tidal volume was evaluated using metrics such as root-mean-square-error (RMSE) and the normalized RMSE (NRMSE), similar to the method described in [5]. $\mathrm{TV}_{\mathrm{spirometer}}$ represents ground-truth spirometer and $\mathrm{TV}_{\mathrm{estimated}}$

represents the estimated tidal volume obtained by mapping impedance measurements across thigh-thigh and thorax to the corresponding spirometer volume signal, and N is the number of respiratory cycles obtained for the signal sequence being analyzed.

$$\mathrm{RMSE} = \sqrt{\frac{\sum_{m=1}^{N} \left(\mathrm{TV}_{\mathrm{spirometer}\ (m)} - \mathrm{TV}_{\mathrm{estimated}\ (m)}\right)^{2}}{N}} \qquad (1)$$

$$\mathrm{NRMSE} = \frac{\mathrm{RMSE}}{\mathrm{mean}(\mathrm{TV}_{\mathrm{spirometer}})}\ 100\% \qquad (2)$$

5.3.3 Day-Day Variability in Bioimpedance

An additional protocol was conducted on one subject, where in addition to the sequences A & B, another sequence D (shallow – normal – deep – maximal inhale-exhale) was performed. The tidal volume was displayed in real time and the subject was asked to adjust their tidal volume to different target levels for shallow, normal, deep, and maximal breathing. The visual feedback ensured there is a significant difference between each respiratory maneuver. This was repeated for three consecutive days. The calibration curve (tidal volume vs. impedance) was computed for each day. Additionally, equations (1) and (2) were used with the calibration from Day 1 for each subsequent day as a means to quantify the error introduced by day-to-day variations.

5.3.4 Within-Session Variability in Bioimpedance

The reproducibility of the thigh-thigh impedance measurements within-session for detecting change in respiratory volume was investigated by conducting back-to-back impedance measurements across a healthy subject. The subject was asked to perform a 2 min sequence of respiratory tasks: shallow – normal – deep – maximal inhale-exhale.

Following that, gel (Spectra 360, Parker Laboratories) was applied to the dry electrodes and the experiments were repeated. For comparison, bioimpedance measurements were performed using wet electrodes across the thorax, again synchronized with the spirometer. Five measurements with each of the dry (thigh), dry + gel (thigh), and wet (thorax) electrodes were obtained on the same day within- the-same session. The subject was asked to stand-sit between the thigh-thigh impedance measurements and the placement of the wet electrodes across the chest was not altered between the measurements. Further, to understand the variability in bioimpedance measurements between different days with wet electrodes across the thorax and thigh-thigh (with gel applied to the dry seat electrodes), experiments using the dry (thigh), dry + gel (thigh), and wet (thorax) electrodes were repeated for five consecutive days. The calibration curve (tidal volume vs. impedance) was computed for each measurement. Mean and standard deviation (SD) were calculated across all the slopes obtained from the calibration curves (impedance vs tidal volume).

5.3.5 Development of Numerical Model for Bioimpedance

To understand the mechanism and sensitivity of thigh-thigh impedance, bioimpedance simulations were performed using FEM modeling in COMSOL Multiphysics with the AC/DC module on a realistic CAD human model (Visible Human Project–Female from the National Library of Medicine). The human model consists of 26 tissues, and 184 individual tissue parts [13]. Dielectric properties were assigned using the IT'IS database [14]. To evaluate the impedance change due to respiration, geometrical changes to the human model were performed using the deformed geometry interface in COMSOL Multiphysics. The frequency-domain study was conducted at 80 kHz and 48 μA.

During inhalation, the diaphragm actively contracts, expanding the lungs, but also pushes the contents of the abdomen in an inferior direction (towards the feet), which forces the abdominal wall out. At the same time, the external intercostal muscles expand and raise the rib cage. Therefore, inhalation was simulated by expanding the lungs and contracting the abdomen. Thus, the volume of the lungs was increased to simulate a fairly typical tidal volume of 0.5 L, while the abdomen was compressed vertically, but expanded forward, preserving the volume of the abdomen. In addition, to understand the contribution of just the lung expansion in the thigh-thigh impedance changes, simulations were performed by increasing the lung volume alone, corresponding to a tidal volume of 0.5 L, with no geometrical changes to the abdomen.

5.3.6 Sensitivity of Pulmonary Edema Detection

The FEM model simulating respiration was used to evaluate the impedance change due to the accumulation of fluid in the lung. The lung was partitioned in two halves and the dielectric properties (conductivity and relative permittivity) in the lower portion of the air-filled lung (0.106 S/m, 3020) were replaced with that of body fluid (1.5 S/m, 98) [7]. Bioimpedance simulations were performed using COMSOL Multiphysics across both the thorax and the back of the thigh.

5.4 Results

5.4.1 Feasibility and Sensitivity of Empirical Bioimpedance Measurements

For an individual, measured impedance is highly correlated with tidal volume, and shows little variation from breath to breath. An example waveform of the measured impedance signal for thigh-thigh and thorax and the corresponding volume signal measured by a spirometer is shown in Figure 5.3. Impedance from both locations are highly correlated (0.85 thigh, 0.93 thorax) to spirometer tidal volume. During normal breathing (Sequence A), thigh impedance varied in a nearly sinusoidal waveform with a measurable peak-peak impedance ranging from 0.022 Ω to 0.290 Ω for different subjects (0.10 Ω ± 0.09 Ω, Mean ± SD), as compared to peak-peak impedance ranging from 0.14 Ω to 2.26 Ω (0.8 Ω ± 0.7 Ω) for the thorax. This showed an impedance change of an order of magnitude lower for thigh-thigh as compared to the thorax. A high correlation of (0.76 thigh, 0.93 thorax) between impedance changes to changes in lung volume measured by a spirometer was observed for sequence B.

For sequence D, which comprised shallow breathing, small breathing cycles corresponding to a spirometer tidal volume of 0.13 L were detected. The thigh location was observed to have high sensitivity to distinguish between shallow, normal, deep, and maximal breathing maneuvers, similar to the thorax. This is demonstrated by the measured changes in impedance, as the peak-peak amplitudes ranged from 0.01 Ω to 0.06 Ω (thigh-thigh) and 0.13 Ω to 2.54 Ω (thorax) corresponding to a tidal volume of 0.13 L to 1.74 L.

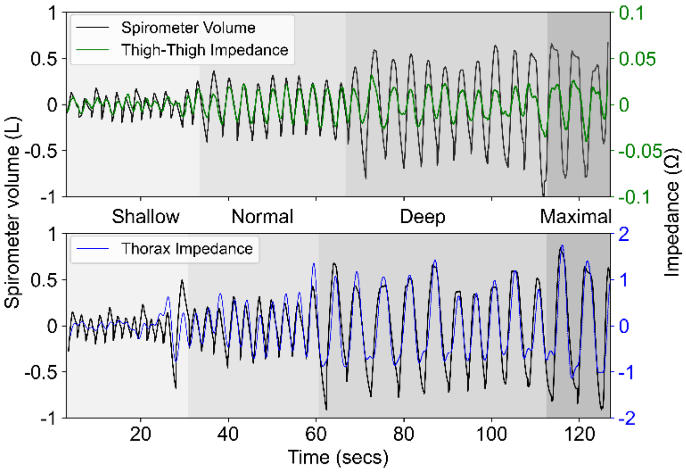

Figure 5.3. Simultaneously captured spirometer volume (black) and impedance signal across thigh-thigh (green) and thorax (blue) for sequence D. Shallow, normal, deep, and maximal breathing maneuvers are shown in lighter to darker gray scales respectively

5.4.2 Estimated Tidal volume

Across the subjects, a tidal volume range of 0.5 L up to 3.8 L was observed for sequence B. The calibration was found to be significantly different across subjects, and varied between 8.5 to 36.9 (18.5 ± 11.0) and 0.5 to 4.6 (2.1 ± 1.6) for thigh-thigh and thorax respectively. The coefficient of determination (R^2) varied from 0.42 to 0.90 (0.65 ± 0.16) for thigh-thigh, and 0.58 to 0.93 (0.74 ± 0.13) for thorax. RMSE computed using equation (1) varied in the range 0.15 L to 0.60 L (0.32 L ± 0.13 L) for thigh-thigh and 0.12 L to 0.40 L (0.25 L ± 0.12 L) for thorax. NRMSE calculated using equation (2) was found to lie between 9.8% and 47% (28.5 % ± 11.8%) for thigh-thigh and varied from 12% to 39% (22.1% ± 10.4%) for thorax.

5.4.3 Day-Day Variability in Bioimpedance

The calibration was observed to be similar for Day 1 (23.26) and Day 2 (24.40), however, it was significantly different for Day 3 (14.31) as shown in Figure 5.4. On Day 3, another measurement captured after repositioning resulted in calibration (11.43) to be within 20% of that of the prior measurement conducted on Day 3. Using the calibration obtained on Day 1, RMSE of 0.14 L and 0.6 L were obtained for Day 2 and Day 3 respectively. NRMSE was found to be 22.2% (Day 2) and 84.6% (Day 3).

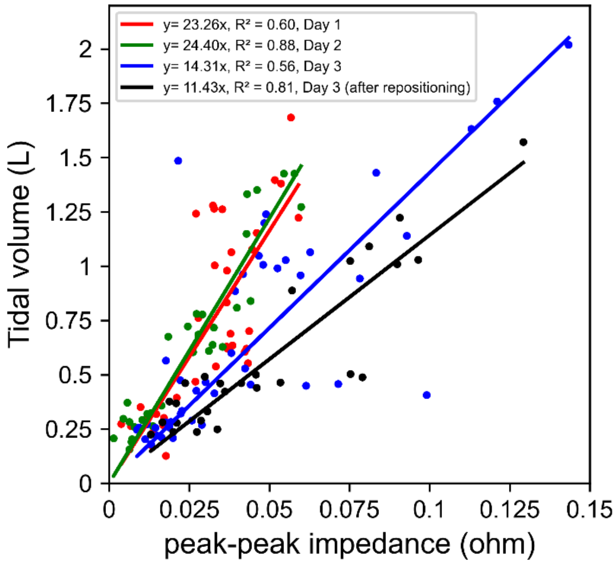

Figure 5.4. Least squares linear regression between the peak-peak impedance across thigh-thigh and the ground-truth tidal volume measured using a spirometer for Day 1 (red), Day 2 (green), Day 3 (blue), and Day 3 after 5 mins (black).

5.4.4 Within-Session Variability in Bioimpedance

The peak-peak bioimpedance measurements were found to be highly correlated to the peak-peak spirometer tidal volume (0.87 dry electrodes across thigh; 0.89 dry + gel electrodes across thigh; 0.90 wet electrodes across thorax, Figure 5.5 and Figure 5.6). For the within-session measurements, the SD was 12.3%, 11.0%, and 10.4% of the mean in the correlation slope for dry (thigh), dry + gel (thigh), and wet (thorax) electrodes respectively (Figure 5.5). The results indicate that the gel on electrodes helped to reduce the thigh-thigh impedance variability but is not a significant factor affecting the reproducibility of the bioimpedance measurements as a function of respiratory volume. For the measurements across five days, the slopes of the linear regression depicted a SD of 14.9%, 8.0%, and 41.5% of mean for dry-thigh (5.6a), dry + gel-thigh (5.6b), and wet (thorax) electrodes respectively (Figure 5.6).

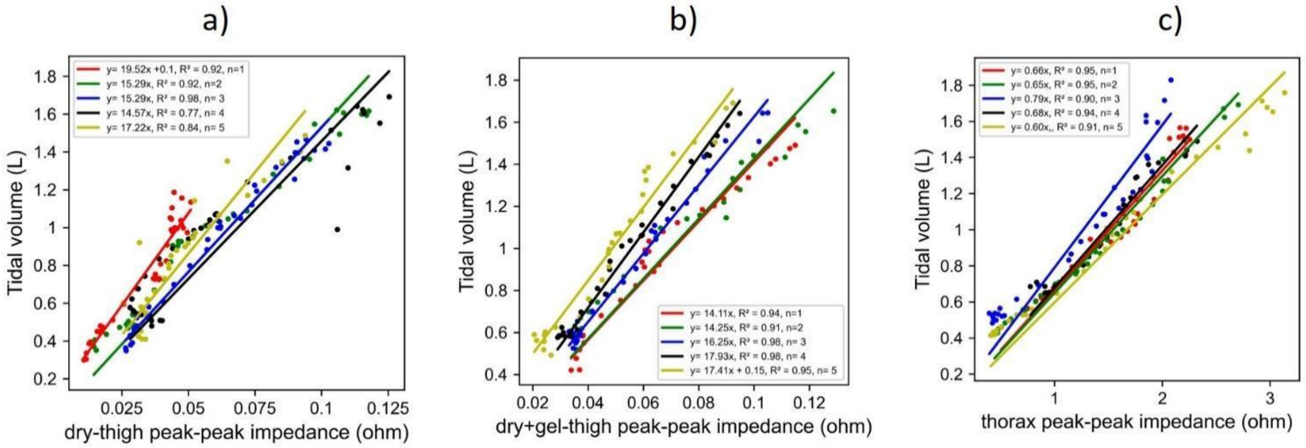

Figure 5.5. Least squares linear regression between the peak-peak impedance across thigh-thigh and the ground-truth tidal volume measured using a spirometer for a) dry electrodes across thigh-thigh b) dry + gel electrodes across thigh-thigh c) wet electrode across the thorax. Raw data and regression line obtained within-session for five back-to-back measurements are shown: n= 1 (red), n= 2 (green), n= 3 (blue), n= 4 (black), n=5 (yellow).

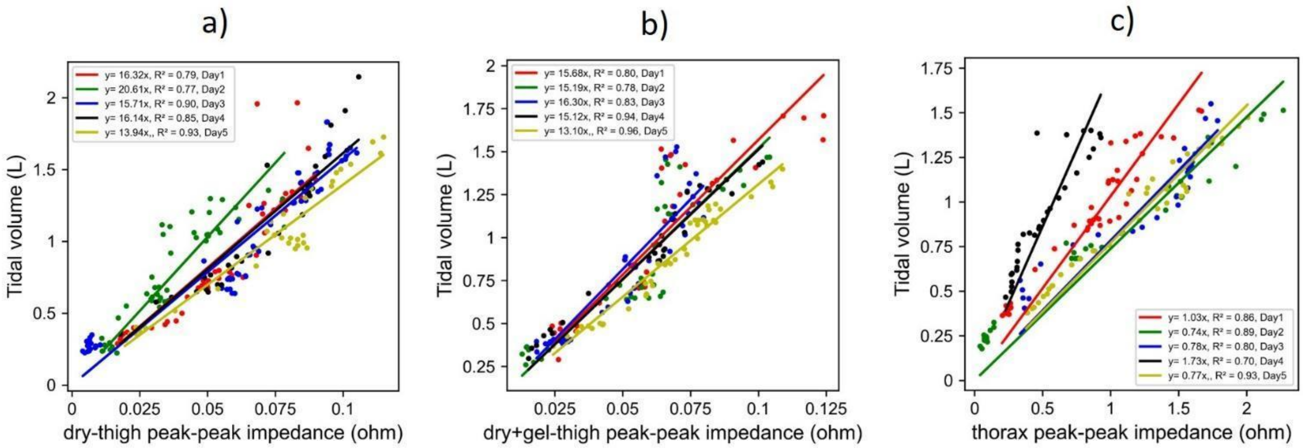

Figure 5.6. Least squares linear regression between the peak-peak impedance across thigh-thigh and the ground-truth tidal volume measured using a spirometer for a) dry electrodes across thigh-thigh b) dry + gel electrodes across thigh-thigh c) wet electrode across the thorax. Slopes obtained for five days are shown: Day 1 (red), Day 2 (green), Day 3 (blue), Day 4 (black), and Day 5 (yellow).

5.4.5 Finite Element Modeling Simulations

In response to the geometrical changes to replicate breathing, our current FEM simulations depict a 16% change in impedance across the thorax and a 1.0% change in impedance across thigh-thigh (Figure 5.7) for a fairly typical tidal volume of 0.5 L. For the simulations across the thorax, it was found there was an increase in impedance during the inhalation process, which is in complete agreement with the previously reported results [2], whereas, thigh-thigh bioimpedance simulations depicted a decrease in impedance with the inhalation. Alone with the changes in lung volume, there were not any significant changes in the thigh-thigh impedance. Thus, the FEM model indicates that the impedance change across thigh-thigh is affected by both lung volume and abdominal compression.

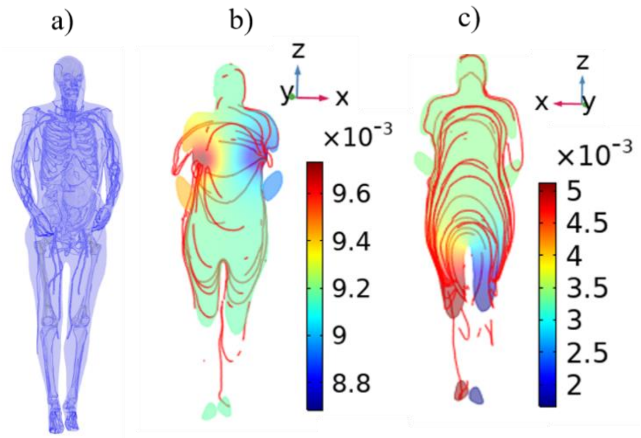

Figure 5.7 a) Computationally efficient VHP model containing organs encapsulated by a layer of muscle, followed by a layer of fat, further covered by a 1 mm thick skin layer. b) transthoracic and c) thigh-thigh bioimpedance simulations performed in COMSOL Multiphysics with respect to geometrical changes to replicate breathing. Generated slice plot of potential and streamlines representing current density.

5.4.6 Sensitivity of Edema Detection

In response to the change in material properties of the air filled lungs with that of fluid, FEM simulations predict a 5.2% decrease (from 49.55 Ω to 46.96 Ω) in impedance and there was no change in impedance across thigh-thigh impedance. This is consistent with the previously reported results [15], [16], as the fluid accumulates in the chest, the impedance decreases, since the conductivity of fluid is more than air. The low sensitivity of thigh-thigh to edema can be explained by FEM solutions (Figure 5.7c) that show that the thigh-thigh current path would predominantly pass through the pelvis and thigh area, and not effectively reach the lung. Thus, the FEM model depicts that the absolute value of thigh-thigh bioimpedance measurements might not be sensitive to pulmonary edema detection.

5.5 Discussion

Transthoracic impedance monitoring provides a surrogate for measuring respiratory parameters and estimating tidal volume because of the linear relationship between lung volume and impedance changes [2], [3]. In this work, we leveraged the bioimpedance technique to detect respiration from the back of the thigh. Figure 5.3 shows that the thigh-thigh impedance correlated well to the changes in lung volume measured by a spirometer. There have been efforts made by other researchers to use the back of the thigh for conducting bioimpedance analysis, however, they targeted different applications such as body hydration [17] and abdominal fat [18]. In fact, Hong et al. performed bioelectrical impedance analysis using toilet seat electrodes and showed the effectiveness of the thigh-thigh current path to measure abdominal fat [18] as compared to conventional foot-foot and hand-foot measurements. That study focused on the absolute values of impedance, whereas we are interested in detection of the change in impedance due to respiration. Nonetheless, our absolute thigh-thigh impedance varied from 20.4 Ω to 29.5 Ω at 80 kHz (N=8) and is consistent to that of Hong et al. (21.65 Ω to 35.62 Ω at 50 kHz).

In this work, due to the novel measurement location for respiration monitoring, the mechanistic principle that leads to the detection of respiration was evaluated. Figure 5.7c shows the available current paths for thigh-thigh bioimpedance measurements. On visualizing the contour lines, they were observed to go all the way up to the thorax, however, that does not mean there is a substantial amount of current that passes through the lungs. Moreover, the vector magnitude of the current density demonstrates that the thigh-thigh current path would predominantly pass through the pelvis and thigh area, and not effectively reach the lung. Further, we observed that the geometrical changes related to abdominal compression varied thigh-thigh impedance magnitude and direction more significantly than the changes in lung volume. As a result, thigh-thigh bioimpedance decreases with inhalation, the inverse of thorax measurements. This inverse relationship was in complete agreement with our empirical results, as a negative correlation of thigh-thigh impedance to respiration was observed across all the 8 subjects for typical breathing.

Interestingly, for one subject we noticed impedance to be directly related (no inversion) with the spirometer volume signal while performing the maximal inhale and exhale maneuver. We believe that this individual switched to a different style of breathing, aka "diaphragmatic" or "belly" breathing (belly moves forward) vs. thoracic breathing (belly moves inward on inhalation and the ribs move up or out) [20] during maximal inhale-exhale maneuvers. The empirical investigation carried out using respiratory belts to capture geometrical changes with respect to thorax and abdomen motion was found to be in agreement with our hypothesis (data not shown). It is worthwhile to mention that sequence C, which was comprised of a holding breath period further validated the out of phase relationship of thigh-thigh impedance (inhalation) with the spirometer volume signal.

A wide range of calibrations, obtained across 8 subjects, demonstrated the physiological diversity and the need for subject-specific calibration, consistent with the findings of previous work [21]. Calibration performed with sequence D was observed to have better regression co-efficient as compared to sequence B, as it comprises a wider range of shallow-maximal breathing maneuvers. Thus, future studies will be conducted using sequence D as calibration, and the effect of other variables such as posture that might affect the calibration will be investigated to address the variability in day-day calibration/repositioning. Figure 5.4 indicates that the calibration of Day 1 used for Day 3 underestimated the tidal volume by 50%. Repositioning alone led to a 20% change in the calibration, suggesting a need to understand the effect of other variables to attain a robust subject-specific calibration for estimating tidal volume. The anatomical information can further provide an insight into the subject-specific calibration. In addition, the FEM model could be used to investigate the effect of other factors, such as excitation frequency, the amplitude of current, and the area of electrodes on the sensitivity of bioimpedance measurements across the back of the thigh.

The FEM model explains that the thigh-thigh current path does not go through the lungs (Figure 5.7c), thus the change in material properties (air replaced with body fluid) did not vary the absolute value of thigh-thigh impedance, and might not be sensitive to pulmonary edema detection. Moreover, the relative change in thigh-thigh impedance corresponding to tidal volume might not be sufficient to be used as an indirect measure of edema detection as tidal volume is not related to edema [19].

This work showed a high correlation of thigh-thigh impedance to the respiration rate and volume signal, similar to that of thorax impedance. The reproducibility experiments depicted that the day-to-day variation is significantly higher for thorax impedance measurements as compared to the thigh-thigh impedance measurements, due to the challenges with consistent placement of the thorax electrodes. The high day-to-day variability in the thorax measurements obtained in this work is consistent with that of Grenvik et al. [22], where a change of 53% and 64% was observed in the slopes of the relationships between chest impedance to that of changes in the lung volume of two subjects on two different days.

For the wet electrodes across the thorax, the variability in measurements conducted within-the-session (10.4%) reduced as compared to that of the inter-day (41.5%), as the electrodes were not moved between measurement sessions. Thus, it is worth mentioning here, that the variability in the thigh-thigh impedance measurements was consistent within a percent or two (12.3% thigh, 10.4% thorax) as the thorax in repeat measurements on the same day, and better between days (14.5% thigh, 41.5% thorax). Although this is preliminary data with a single subject, it indicates that the day-to-day variability of the relationship between impedance and volume will limit the accuracy and sensitivity of respiratory tidal volume. Therefore, there is a need to understand the factors that lead to the variations, especially within-session measurements and future work will help determine these limits.

5.6 Conclusion

This work demonstrates the feasibility and sensitivity of respiration monitoring from the back of the thigh, using electrodes integrated into a toilet seat. Empirical results showed a measurable impedance change with respect to shallow, normal, deep, and maximal breathing maneuvers, which shows the ability to effectively measure the respiration rate. The linear relationship between thigh-thigh impedance and lung volume provides an approach that can be used to estimate tidal volume that could provide valuable insight into disease states for conditions ranging from COVID-19 to heart failure. This novel study takes into account practical implementation and patient compliance. It could be used to provide respiratory health data unobtrusively and thus has the potential to revolutionize in-home respiratory monitoring.

References

[1] W. Groenendaal, S. Lee, and C. van Hoof, “Wearable Bioimpedance Monitoring: Viewpoint for Application in Chronic Conditions,” *JMIR Biomed. Eng.*, vol. 6, no. 2, p. e22911, 2021, doi: 10.2196/22911.

[2] M. Młyńczak and G. Cybulski, “Impedance pneumography: Is it possible?,” *Photonics Appl. Astron. Commun. Ind. High-Energy Phys. Exp. 2012*, vol. 8454, p. 84541T, 2012, doi: 10.1117/12.2000223.

[3] J. A. Berkebile, S. Mabrouk, V. Ganti, A. Srivatsa, J. Sanchez-Perez, and O. T. Inan, “Towards Estimation of Tidal Volume and Respiratory Timings via Wearable-Patch-Based Impedance Pneumography in Ambulatory Settings,” *IEEE Trans. Biomed. Eng.*, vol. 9294, no. c, 2021, doi: 10.1109/TBME.2021.3130540.

[4] I. C. Gyllensten *et al.*, “Early indication of decompensated heart failure in patients on home-telemonitoring: A comparison of prediction algorithms based on daily weight and noninvasive transthoracic bioimpedance,” *JMIR Med. Informatics*, vol. 4, no. 1, pp. 1–13, 2016, doi: 10.2196/medinform.4842.

[5] B. A. Reyes, N. Reljin, Y. Kong, Y. Nam, and K. H. Chon, “Tidal Volume and Instantaneous Respiration Rate Estimation using a Volumetric Surrogate Signal Acquired via a Smartphone Camera,” *IEEE J. Biomed. Heal. Informatics*, vol. 21, no. 3, pp. 764–777, 2017, doi: 10.1109/JBHI.2016.2532876.

[6] N. J. Conn, K. Q. Schwarz, and D. A. Borkholder, “Nontraditional electrocardiogram and algorithms for inconspicuous in-home monitoring: Comparative study,” *JMIR mHealth uHealth*, vol. 6, no. 5, 2018, doi: 10.2196/mhealth.9604.

[7] L. Beckmann, D. Van Riesen, and S. Leonhardt, “Optimal electrode placement and frequency range selection for the detection of lung water using Bioimpedance Spectroscopy,” *Annu. Int. Conf. IEEE Eng. Med. Biol. - Proc.*, pp. 2685–2688, 2007, doi: 10.1109/IEMBS.2007.4352882.

[8] S. Rossi, C. Mancarella, C. Mocenni, and L. Della Torre, “Bioimpedance sensing in wearable systems: From hardware integration to model development,” *RTSI 2017 - IEEE 3rd Int. Forum Res. Technol. Soc. Ind. Conf. Proc.*, 2017, doi: 10.1109/RTSI.2017.8065956.

[9] O. I. Shuvo and M. N. Islam, “Sensitivity Analysis of the Tetrapolar Electrical Impedance Measurement Systems Using COMSOL Multiphysics for the non-uniform and Inhomogeneous Medium,” *Dhaka Univ. J. Sci.*, vol. 64, no. 1, pp. 7–13, 2016, doi: 10.3329/dujs.v64i1.28517.

[10] A. Ikarashi, M. Nogawa, S. Tanaka, and K. I. Yamakoshi, “Experimental and numerical study on optimal spot-electrodes arrays in transthoracic electrical impedance cardiography,” *Annu. Int. Conf. IEEE Eng. Med. Biol. - Proc.*, pp. 4580–4583, 2007, doi: 10.1109/IEMBS.2007.4353359.

[11] A. A. Danilov, D. V. Nikolaev, S. G. Rudnev, V. Y. Salamatova, and Y. V. Vassilevski, “Modelling of bioimpedance measurements: Unstructured mesh application to real human anatomy,” *Russ. J. Numer. Anal. Math. Model.*, vol. 27, no. 5, pp. 431–440, 2012, doi: 10.1515/rnam-2012-0024.

[12] D. Makowski *et al.*, “NeuroKit2: A Python toolbox for neurophysiological signal processing,” *Behav. Res. Methods*, vol. 53, no. 4, pp. 1689–1696, 2021, doi: 10.3758/s13428-020-01516-y.

[13] “VHP-FEMALE CAD HUMAN MODEL _ neva.” https://www.nevaelectromagnetics.com/vhp-female-3-1 (accessed Feb. 08, 2021).

[14] M. C. Kuster Niels, “Dielectric Properties » IT’IS Foundation,” 2020. https://itis.swiss/virtual-population/tissue-properties/database/dielectric-properties/

[15] L. M. Yamokoski, G. J. Haas, B. Gans, and W. T. Abraham, “OptiVol® fluid status monitoring with an implantable cardiac device: A heart failure management system,” *Expert Rev. Med. Devices*, vol. 4, no. 6, pp. 775–780, 2007, doi: 10.1586/17434440.4.6.775.

[16] A. Fein, R. F. Grossman, J. G. Jones, P. C. Goodman, and J. F. Murray, “Evaluation of transthoracic electrical impedance in the diagnosis of pulmonary edema,” *Circulation*, vol. 60, no. 5, pp. 1156–1160, 1979, doi: 10.1161/01.CIR.60.5.1156.

[17] T. Schlebusch, W. Fichtner, M. Mertig, and S. Leonhardt, “Unobtrusive and comprehensive health screening using an intelligent toilet system,” *Biomed. Tech.*, vol. 60, no. 1, pp. 17–29, 2015, doi: 10.1515/bmt-2013-0140.

[18] H. H. Ki, G. L. Yong, and S. P. Kwang, “Effectiveness of thigh-to-thigh current path for the measurement of abdominal fat in bioelectrical impedance analysis,” *Med. Biol. Eng. Comput.*, vol. 47, no. 12, pp. 1265–1271, 2009, doi: 10.1007/s11517-009-0551-z.

[19] J. Sharp T, G. Geraint T, I. L. Bunnell, and D. G. Greene, “Ventilatory Mechanics in Pulmonary Edema,” *J Clin Invest*, vol. 37, no. 1, pp. 111–117, 1958, doi: 10.1172/JCI103577.

[20] A. Tsoli, N. Mahmood, and M. J. Black, “Breathing life into shape:capturing, modeling and animating 3D human breathing,” *ACM Trans. Graph.*, vol. 33, no. 4,

2014, doi: 10.1145/2601097.2601225.

[21] M. Młyńczak, W. Niewiadomski, M. Zyliński, and G. Cybulski, “Assessment of calibration methods on impedance pneumography accuracy,” *Biomed. Tech.*, vol. 2015, no. 6, pp. 587–593, 2015, doi: 10.1515/bmt-2015-0125.

[22] A. Grenvik, S. Ballou, E. McGinley, J. E. Millen, W. L. Cooley, and P. Safar, “Impedance pneumography. Comparison between chest impedance changes and respiratory volumines in 11 healthy volunteers.,” *Chest*, vol. 62, no. 4, pp. 439–443, 1972, doi: 10.1378/chest.62.4.439.

Chapter 6: Future Work and Final Remarks

6.1 Future studies with skin phantom

The present work details the fabrication of a skin mimicking phantom that replicates the electrical properties of the skin interacting with dry electrodes. Using a novel porosity-based approach, it can be used to vary hydration in a controlled predictive manner and used as a platform for carrying out benchtop experiments. This control is not achievable on *in vivo* human skin due to inter and intra-subject variability. The phantom can be used to facilitate electrode development, greatly reducing cost and complexity and increasing reproducibility by working with phantoms instead of human subjects.

The developed phantom was used for characterizing the dry electrodes in the low-frequency regime (1 Hz- 1000 Hz), crucial for acquiring biopotential signals such as ECG, EMG, and EEG. Further, the developed phantom was used to investigate the dependence of the skin-electrode contact impedance on the electrode material, electrode area, and skin hydration. This was accomplished by developing a novel equivalent circuit model for the skin-electrode interface impedance model.

The developed model provides insight into the transduction mechanism for dry electrodes in recording biopotential measurements. The model explains the contribution of electrode area, material, and skin hydration and it could be used for design of future wearable electrodes. Further, the present work evaluates the feasibility of using large metal dry electrodes in two different applications. First, it demonstrates the ability to capture clinically relevant Electrocardiogram signals using large dry titanium electrodes using a toilet seat cardiovascular monitoring system. Secondly, this application was extended to a respiration monitoring system, by proposing a novel approach for monitoring respiration by measuring changes in impedance from the back of the thigh, both empirically and computationally using finite element modeling. The underlying principles, experimental protocols, and computational techniques presented in this work are transferable to other electrophysiological signals and lay a foundation for developing non-invasive continuous or wearable in-home monitoring physiological systems. This chapter provides concluding remarks and details of future studies, which are natural extensions of this work and can be built upon the present work.

To summarize, this work fills in the following gaps in the current state of the art:

1. Provides a biomimetic skin phantom capable of simulating the electrical properties of skin along with controlled hydration status in the low-frequency regime that can be used as a platform for benchtop testing of new electrode designs.
2. Elucidates the mechanistic principle of biopotential electrodes and the crucial factors such as material and skin hydration that affect electrode performance, thus facilitating wearable electrode development.
3. Provides a novel approach for unobtrusive in-home respiration monitoring that can be used to detect respiration rate and tidal volume and could provide valuable insight into disease state for conditions ranging from COVID-19 to heart failure.

6.1.1 Characterization of wearable hydration sensors

The current skin phantom was intended to characterize the performance of biopotential signal monitoring electrodes in the low-frequency regime. The developed phantom is also capable of modeling different hydration states of the skin. Future studies utilizing the skin phantom can be structured to investigate the performance of wearable hydration sensors. For the skin hydration measurement, the water content of the stratum corneum (outer layer of the skin), plays a crucial role and affects the electrical properties of the skin [1]. The development of wearable sensors is directly performed by conducting experiments on *in vivo* human skin, which lacks explicit control. In this work, the proposed porosity approach was able to model various stratum corneum hydration states ranging from very dry skin (0.16% porosity) to sufficiently hydrated skin (0.28%). Thus, the novel porosity-based hydration approach has the potential to facilitate the characterization of wearable hydration sensors.

In the current work, the porosity-based hydration status was evaluated by carrying out impedance measurements using a 2-electrode setup (shown in Figure 3.2) and validated with the human skin data across healthye subjects. However, it will be beneficial to validate the phantom with the more direct and standard method and against a gold standard such as a corneometer [2](Figure 6.1).

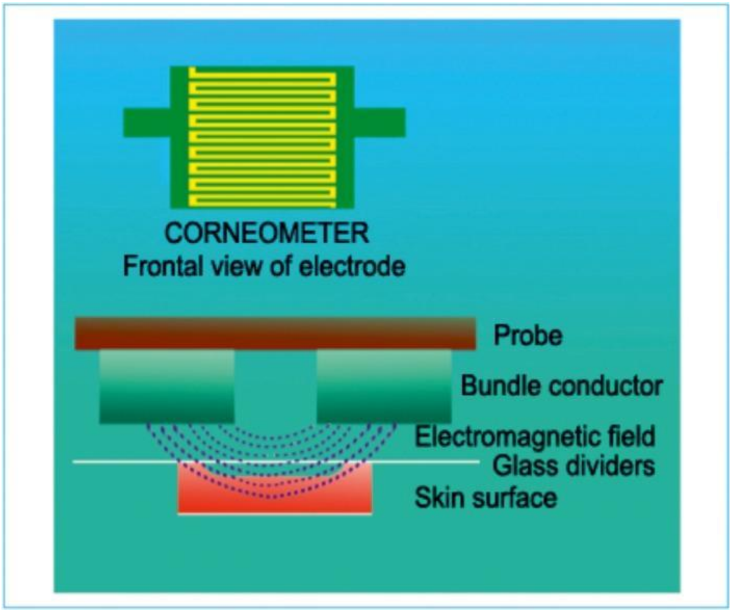

Figure 6.1. Corneometer® CM 825 head probe is composed of two conductor tracks (gold electrodes) with different electrical charges and a separating glass lamina that prevents current conduction in the skin. A scattered electromagnetic field is generated between the metallic tracks and penetrates the very first layer of the skin during the measurement, determining the dielectric constant of the stratum corneum [3].

6.1.2 Lower pore spacing for testing smaller electrodes

The current phantom was tested with metal-based dry electrodes of areas 4 cm^2 and 9 cm^2. Most of the wearable electrodes are being designed for watches, or patches, that are smaller in area (1 cm^2 or smaller). In this work, the spacing between two pores centers was 2 mm and the pore size was 0.3 mm in diameter. Spacing between the pores and the pore size can be reduced to extend this work for the testing of smaller size electrodes, so that a very small electrode may touch sufficient number of pores. Thus, the modified design of the upper layer of the phantom will enable the testing of the smaller-size electrodes with an application intended for wearable devices. Moreover, the design modifications can also be used to explore the performance of different electrode designs such as interdigitated electrode design, commonly used in hydration sensors [1], [4], [5], [6].

6.2 Novel biopotential electrode material

One of the key challenges in the signal quality with the dry wearable electrodes is due to the high skin-electrode impedance. The findings of the current work [7], showed that the high relative permittivity of the electrode material native oxide leads to an enhancement in the capacitive coupling and thus a lower skin-electrode impedance. This finding can be used and novel electrode materials with high relative permittivity can be developed.

The current work was focused on understanding the transduction mechanism of the metal-based dry electrodes using a skin-electrode interface model. Future studies can be conducted on characterizing the performance of flexible soft electrodes [8]. This can be done similar to the present work, by carrying out experiments in a controlled way on a phantom, and then developing a skin-electrode interface model.

6.3 Bioimpedance future studies

6.3.1 Effectiveness of monitoring respiration rate

This work shows that thigh-thigh bioimpedance depicts a high correlation to the respiration rate and thus can be effectively used to measure respiratory rate. Recent evidence suggests that an adult with a respiratory rate of over 20 breaths/minute and over 24 breaths/minute indicates an unwell and critically ill condition respectively [9]. For COVID-19 disease, a respiratory rate higher than 30/min can be an indicator of the presence of severe disease [10]. In addition to the respiratory rate measurement, combined measurements of heart rate and oxygen saturation can serve as the method for early recognition of high-risk and critically ill patients [10]. Therefore, the novel approach of measuring respiration from the back of the thigh can be integrated into the toilet seat cardiovascular monitoring system, capable of measuring heart rate and oxygen saturation, and can be used to indicate health conditions.

In the current work, the data collection was conducted in a controlled environment and across healthy subjects. However, the FIT seat will be not in a controlled environment. Future studies can be carried out by integrating motion artifacts and developing robust algorithms to reject the introduced motion artifacts.

6.3.2 Accuracy and sensitivity of respiratory tidal volume

The present work demonstrates a linear relationship between thigh-thigh bioimpedance and lung volume and an ability to capture different breathing patterns. This relationship could be leveraged and may be useful for tracking COVID-19 recovery. The COVID-19 surviving patients require long-term pulmonary monitoring after discharge [11], therefore, a spirometer is recommended for daily use to monitor and evaluate pulmonary functioning for rehabilitation care during COVID-19 recovery [12]. In a recent research study, the findings indicate that the forced vital capacity values (FVC) were smaller than the normality values by 32% in discharged COVID-19 patients. [13]. Therefore, it is important to evaluate the sensitivity of this technique to detect change in tidal volume during COVID-19 recovery.

In this work, preliminary data across a single healthy subject for the inter-day variability of the thigh-thigh bioimpedance measurements resulted in a 14% variation in the calibration slopes (tidal volume vs impedance). Current thorax-based wearable devices for daily monitoring of lung functioning also have the challenges of accurately estimating the tidal volume based on the previous calibration coefficients [15]. Moreover, monitoring of changes in respiratory volume using wearable sensors results in a relative volumetric error of higher than 10% [14]. Thus, the day-day variability of the relationship between impedance and volume, limits the accuracy and reliability of measuring respiratory tidal volume. In this work, the system was able to detect respiration rate, but the accuracy and repeatability of the magnitude may make it impractical for tracking day-to-day volumetric changes in a patient. Thus, the factors that cause the variability should be investigated.

References

[1] S. Yao *et al.*, “A Wearable Hydration Sensor with Conformal Nanowire Electrodes,” *Adv. Healthc. Mater.*, vol. 6, no. 6, pp. 1–8, 2017, doi: 10.1002/adhm.201601159.

[2] U. Heinrich *et al.*, “Multicentre comparison of skin hydration in terms of physical-, physiological- and product-dependent parameters by the capacitive method (Corneometer CM 825),” *Int. J. Cosmet. Sci.*, vol. 25, no. 1–2, pp. 45–53, 2003, doi: 10.1046/j.1467-2494.2003.00172.x.

[3] M.-M. Constantin, E. Poenaru, C. Poenaru, and T. Constantin, “Skin Hydration Assessment through Modern Non-Invasive Bioengineering Technologies.,” *Maedica (Buchar).*, vol. 9, no. 1, pp. 33–8, 2014.

[4] C. Malnati, D. Fehr, F. Spano, and M. Bonmarin, “Modeling stratum corneum swelling for the optimization of electrode-based skin hydration sensors,” *Sensors*, vol. 21, no. 12, 2021, doi: 10.3390/s21123986.

[5] M. A. Yokus and M. A. Daniele, “Skin Hydration Sensor for Customizable Electronic Textiles,” *MRS Adv.*, vol. 1, no. 38, pp. 2671–2676, 2016, doi: 10.1557/adv.2016.540.

[6] R. AlDisi, Q. Bader, and A. Bermak, “Hydration Assessment Using the Bio-Impedance Analysis Method,” *Sensors*, vol. 22, no. 17, pp. 1–16, 2022, doi: 10.3390/s22176350.

[7] K. Goyal, D. A. Borkholder, and S. W. Day, “Dependence of Skin-Electrode Contact Impedance on Material and Skin Hydration,” *Sensors*, vol. 22, no. 8510, 2022, doi:

10.3390/s22218510.

[8] S. Masihi *et al.*, “Development of a Flexible Wireless ECG Monitoring Device with Dry Fabric Electrodes for Wearable Applications,” *IEEE Sens. J.*, vol. 22, no. 12, pp. 11223–11232, 2022, doi: 10.1109/JSEN.2021.3116215.

[9] M. A. Cretikos, R. Bellomo, K. Hillman, J. Chen, S. Finfer, and A. Flabouris, “Respiratory rate: The neglected vital sign,” *Med. J. Aust.*, vol. 188, no. 11, pp. 657–659, 2008, doi: 10.5694/j.1326-5377.2008.tb01825.x.

[10] Q. Sun, H. Qiu, M. Huang, and Y. Yang, “Lower mortality of COVID-19 by early recognition and intervention: experience from Jiangsu Province,” *Ann. Intensive Care*, vol. 10, no. 1, pp. 2–5, 2020, doi: 10.1186/s13613-020-00650-2.

[11] J. You *et al.*, “Anormal pulmonary function and residual CT abnormalities in rehabilitating COVID-19 patients after discharge,” *J. Infect.*, vol. 81, no. 2, pp. e150–e152, 2020, doi: 10.1016/j.jinf.2020.06.003.

[12] Q. Xu *et al.*, “A portable triboelectric spirometer for wireless pulmonary function monitoring,” *Biosens. Bioelectron.*, vol. 187, no. March, p. 113329, 2021, doi: 10.1016/j.bios.2021.113329.

[13] A. Fumagalli *et al.*, “Pulmonary function in patients surviving to COVID-19 pneumonia,” *Infection*, vol. 49, no. 1, pp. 153–157, 2021, doi: 10.1007/s15010-020-01474-9.

[14] V. Monaco and C. Stefanini, “Assessing the tidal volume through wearables: A scoping review,” *Sensors*, vol. 21, no. 12, pp. 1–21, 2021, doi: 10.3390/s21124124.

[15] D. Mannée, F. De Jongh, and H. Van Helvoort, “The accuracy of tidal volume measured with a smart shirt during tasks of daily living in healthy subjects: Cross-sectional study,” *JMIR Form. Res.*, vol. 5, no. 10, pp. 1–10, 2021, doi: 10.2196/30916.